



System development for improvement of quality inspection and control in the food industry

Rodrigo Alves Lopes

Thesis to obtain the Master of Science Degree in

Mechanical Engineering

Supervisors: Prof. Carlos Baptista Cardeira

Prof. Paulo Miguel Nogueira Peças

Examination Committee

Chairperson: Prof. Paulo Jorge Coelho Ramalho Oliveira

Supervisor: Prof. Carlos Baptista Cardeira

Member of the Committee: Prof. João Rogério Caldas Pinto

June 2019

Acknowledgements

First of all, I would like to thank my supervisor, Professor Paulo Peças for providing me the opportunity to develop this thesis in TetraPak, and Professor Carlos Carneira for his availability, support and shared knowledge during this work.

I would also like to thank Engineer Pedro Bicudo for all the guidance and support during this project, and to all TetraPak employees for the help and friendship provided.

I also thank Professor Melão Barros, Professor Manuel Freitas and Pedro Teixeira for access to the laboratories and support in the experiments conducted. A big thank you to Vítor Medeiros as well for the help and material provided.

Last, a thank you to all my family and friends for the encouragement and support.

Resumo

O objetivo desta dissertação é identificar um sistema capaz de realizar a inspeção da qualidade de selagem de filme BOPP no embalamento de palhinhas de plástico, em linha com a produção, levando à detecção e contenção de produtos defeituosos. Neste trabalho são estudados o princípio do processo de selagem e os parâmetros que o governam. Amostras de filme selado, coletadas com diferentes parâmetros de processo em ambiente industrial, são inicialmente classificadas de acordo com a sua força de selagem com um teste de descolamento, exterior à produção. Para inspeção em linha com a produção duas soluções distintas são propostas. Um sistema para a medição da temperatura do filme após selagem usando pirômetros infravermelhos é proposto e a sua correlação com a variação da força de selagem é estudada. Um sistema baseado em visão computacional também é apresentado, em que amostras de imagens são coletadas com um sistema de iluminação infravermelha e um sistema de filtragem polarizadora. Para extração das características da imagem, dois descritores de textura são propostos baseados em local binary pattern e em gray level co-occurrence matrix, e para classificação, uma rede neuronal multi-layer perceptron é usada. As capacidades de ambos os sistemas em identificarem com precisão defeitos de selagem do filme são analisadas.

Palavras-Chave: Selagem, Filme BOPP, Inspeção em linha, Pirômetro, Iluminação infravermelha, Filtro polarizador, Textura

Abstract

The objective of this thesis is to identify a system capable of in-line inspection of BOPP film sealing quality in straw packaging, leading to the detection and containment of defective products. In this work, the sealing process principle and the parameters that govern the process are studied. Sealed film samples, collected with different process parameters in an industrial environment, are initially classified according to their seal strength with an off-line peel test. For in-line inspection, two distinct solutions are proposed. A system for the measurement of film temperature after sealing using infrared pyrometers is studied and its correlation with seal strength variation is analyzed. A system based on machine vision is also studied, where sample images are acquired with an infrared lighting system and a polarized filtering system. For image features extraction, two textural descriptors are proposed based on the local binary pattern and the gray level co-occurrence matrix and for classification, a multi-layer perceptron neural network is used. The capabilities of both systems in accurately identifying film sealing defects are analyzed.

Keywords: Sealing, BOPP film, In-line inspection, Pyrometer, Infrared lighting, Polarized filter, Texture

Contents

Acknowledgements	iii
Resumo	v
Abstract	vii
List of tables	xiii
List of figures	xvi
Nomenclature	xx
Glossary	xiii
1 Introduction	1
1.1 Motivation	1
1.2 State of Art.....	2
1.3 Thesis Objectives and Contributions	3
1.4 Thesis Outline.....	4
2 Sealing Process Model	6
2.1 Factory production	6
2.1.1 Packaging film	7
2.2 Heat sealing process	8
2.2.1 Conductance sealing principle	9
2.2.2 Heat flow resistances	10
2.2.3 Heat roller sealing model.....	10
2.3 Sealing defects	13
3 Seal Quality Analysis	15
3.1 Sample collection.....	15
3.2 Seal strength experimental results	16
3.2.1 Critical area identification	17
3.2.2 Relation between sealing parameters and seal strength	18

4	Film Temperature Analysis	20
4.1	Thermistors in temperature analysis	20
4.2	Radiation pyrometry in temperature analysis	21
4.2.1	Thermal radiation.....	22
4.3	Pyrometry devices	24
4.3.1	Pyrometers	25
4.3.2	Thermographic cameras	25
4.3.3	Selection criteria	26
4.4	Pyrometry applied to sealing inspection	26
4.4.1	Pyrometry applied to BOPP film.....	27
4.5	Pyrometry equipment application	29
4.5.1	Thermographic camera	29
4.5.2	Pyrometer.....	31
5	Pyrometer Model	34
5.1	Theoretical model	34
5.2	Experimental model.....	35
5.3	Production process implementation	36
5.3.1	Film surface temperature variation.....	36
5.4	Pyrometer model response to film temperature variation	39
6	Film Sealing Imaging	42
6.1	Image acquisition.....	42
6.1.1	Infrared imaging.....	43
6.1.2	Polarized filtering imaging	45
6.2	Image preprocessing	47
6.3	Features Extraction	48
6.3.1	Texture Analysis	48
6.3.2	Local binary pattern (LBP) descriptor.....	49
6.3.3	Gray level co-occurrence matrix.....	51
6.4	Image Classification	54
6.4.1	Method performance evaluation.....	55
7	Imaging Experimental Results	57

7.1	Local binary pattern descriptor results.....	58
7.2	Gray level co-occurrence matrix results	59
7.3	Results comparison	62
8	Pyrometer Experimental Results	64
8.1	Installation.....	64
8.2	Experiment in normal production conditions	64
8.2.1	Theoretical model validation.....	66
8.2.2	Peak temperature analysis – Moving average filter	68
8.3	Experiment with abnormal production conditions.....	69
8.3.1	Experiment results with sealing temperature variation.....	69
8.3.2	Experiment results with sealing pressure variation	71
9	Conclusions.....	73
9.1	Achievements	73
9.2	Future Work	74
10	Bibliography	75
	Appendix A – Peel Test Method.....	81
A.1	Sample preparation	81
A.2	Test Procedure	82
A.3	Results Analysis	83
	Appendix B – Pyrometer Installation.....	84
	Appendix C – Imaging Result Values	86
C.1	Local binary pattern results	86
C.1.1	Clear film.....	87
C.1.2	Rugged film.....	91
C.2	Gray level co-occurrence matrix results.....	95
C.2.1	Clear film.....	95
C.2.2	Rugged film.....	98

List of Tables

Table 3.1. Sample collection parameters and qualitative sealing analysis for clear film. The machine's normal working conditions are at 115°C and 0.5 MPa.....	16
Table 3.2. Sample collection parameters and qualitative sealing analysis for rugged film. The machine's normal working conditions are at 130°C and 0.5 MPa.....	16
Table 5.1. Experimental model mean settling time. σ represents the standard deviation.	35
Table 5.2. Straw specifications.....	37
Table 5.3. Parameters related to pyrometer measurement.	37
Table 5.4. Production velocity estimated.....	38
Table 7.1. Table representing the division of images collected for each category.	57
Table 7.2. Best F1 scores for variation of radius and number of pixels.	58
Table 7.3. Performance results for multiple LBP.....	59
Table 7.4. Distance in pixels that results in the best performance.....	60
Table 7.5. Performance results for multiple GLCM.	61
Table 7.6. Comparison between the best F1 score obtained from both texture descriptors.	62
Table 7.7. Computational times for the different algorithms.....	63
Table 8.1. Average values and standard deviation of the peak and valley film temperature.....	66
Table 8.2. Statistical results of the error between the theoretical model and the experimental pyrometer response.....	67
Table 8.3. Comparison of the maximum temperature errors obtained with and without the moving average filter as a comparison with the theoretical model. M corresponds to the number of points averaged.	68
Table 8.4. Pyrometer response at different sealing temperatures for both types of film.	70
Table 8.5. Pyrometer response at different sealing pressure for both types of film.....	72
Table C.1. F_1 score obtained from clear film classification with infrared imaging with variation of the radius together with the number of neighborhood pixels.	87
Table C.2. F_1 score obtained from clear film classification with polarized filtering imaging with variation of the radius together with the number of neighborhood pixels.	88

Table C.3. F_1 score obtained from clear film classification with infrared imaging with multiple LBP, where the LBP 2 parameters result from the variation of the radius together with the number of neighborhood pixels.	89
Table C.4. F_1 score obtained from clear film classification with polarized filtering imaging with multiple LBP, where the LBP 2 parameters result from the variation of the radius together with the number of neighborhood pixels.	90
Table C.5. F_1 score obtained from rugged film classification with infrared imaging with variation of the radius together with the number of neighborhood pixels.	91
Table C.6. F_1 score obtained from rugged film classification with polarized filtering imaging with variation of the radius together with the number of neighborhood pixels.	92
Table C.7. F_1 score obtained from rugged film classification with infrared imaging with multiple LBP, where the LBP 2 parameters result from the variation of the radius together with the number of neighborhood pixels.	93
Table C.8. F_1 score obtained from rugged film classification with polarized filtering imaging with multiple LBP, where the LBP 2 parameters result from the variation of the radius together with the number of neighborhood pixels.	94
Table C.9. F_1 score obtained from clear film classification with variation of the number of gray levels.	95
Table C.10. F_1 score obtained from clear film classification with variation of the angle direction (NL=32).	95
Table C.11. F_1 score obtained from clear film classification with variation of the pixels distance (NL=32; DA=45°).	96
Table C.12. F_1 score obtained from clear film classification with variation of the descriptors used (NL=32; DA=45°; DI=15 and DI=12 for infrared and polarized filtering imaging respectively).	96
Table C.13. F_1 score obtained from clear film classification with multiple angle directions (NL=32; DI=15 and DI=12 for infrared and polarized filtering imaging respectively).	96
Table C.14. F_1 score obtained from clear film classification with variation of the pixels distance of the second angle direction (NL=32, DI ₁ =15, DA ₁ =45°, DA ₂ =0° for infrared imaging; NL=32, DI ₁ =12, DA ₁ =45°, DA ₂ =0° for polarized filtering imaging)	97
Table C.15. F_1 score obtained from clear film classification with variation of the pixels distance of the second angle direction (NL=32, DI ₁ =15, DA ₁ =45°, DI ₂ =6, DA ₂ =0° for infrared imaging; NL=32, DI ₁ =12, DA ₁ =45°, DI ₂ =17; DA ₂ =0° for polarized filtering imaging)	97
Table C.16. F_1 score obtained from rugged film classification with variation of the number of gray levels.	98
Table C.17. F_1 score obtained from rugged film classification with variation of the angle direction (NL=32).	98

Table C.18. F_1 score obtained from rugged film classification with variation of the pixels distance (NL=32; DA=0°).....	98
Table C.19. F_1 score obtained from rugged film classification with variation of the descriptors used (NL=32; DA=0°; DI=14 and DI=8 for infrared and polarized filtering imaging respectively).	99
Table C.20. F_1 score obtained from rugged film classification with multiple angle directions (NL=32; DI=15 and DI=12 for infrared and polarized filtering imaging respectively).....	99
Table C.21. F_1 score obtained from rugged film classification with variation of the pixels distance of the second angle direction (NL=32, DI ₁ =14, DA ₁ =0°, DA ₂ =90° for infrared imaging; NL=32, DI ₁ =8, DA ₁ =0°, DA ₂ =45° for polarized filtering imaging)	99
Table C.22. F_1 score obtained from rugged film classification with variation of the pixels distance of the second angle direction (NL=32, DI ₁ =14, DA ₁ =0°, DI ₂ =17, DA ₂ =90° for infrared imaging; NL=32, DI ₁ =8, DA ₁ =0°, DI ₂ =4; DA ₂ =45° for polarized filtering imaging)	100

List of Figures

Figure 2.1. Different types of straws.....	6
Figure 2.2. Picture of the heat-sealing cylinder, together with the final product leaving the machine. ...	7
Figure 2.3. Packaging film model.....	7
Figure 2.4. On the left: cylinder for clear film; on the right: cylinder for rugged film.....	8
Figure 2.5. On the left: clear film packaging; on the right: rugged film packaging.	8
Figure 2.6. Model representing molecular entanglements in heat sealing processes [1].	9
Figure 2.7. Representation of contact resistance. Due to the irregular surface of the materials, full contact is never achieved [22].....	10
Figure 2.8. Model representing the sealing process. Both films are pressured between the rolls. The heat sealable layers are represented at red and orange.	11
Figure 2.9. Graphic representing the temperature variation between the two rolls. T_{sr} represents the temperature at the surface of the sealing roll, Tt represent the temperatures at the surfaces of the top film, and Tb the temperatures of the bottom film.	11
Figure 3.1. Distribution of the samples collected throughout the film length.....	17
Figure 3.2. Seal strength distribution according to sample area collected.....	17
Figure 3.3. Evolution of seal strength according to the sealing temperature.	18
Figure 3.4. Evolution of seal strength according to the sealing pressure.	19
Figure 4.1: Semitransparent medium model [22].	23
Figure 4.2: Spectral ranges used in radiation pyrometry [20].	26
Figure 4.3. Diagram representing the relation between the wavelength and the polypropylene transmissivity [20].....	28
Figure 4.4. Diagram representing the relation between wavelength and atmospheric gas absorption [20].	28
Figure 4.5: Thermographic Camera Optris® Xi 400.....	29
Figure 4.6: On the left: video frame captured; on the right: color legend related to temperature	30
Figure 4.7. Diagram representing the film leaving the machine. At orange: inspected line by the pyrometers.	31

Figure 4.8. Pyrometer Optris® CTP3.	32
Figure 4.9. On the left: Straw drawing; on the right: relation between the diameter of the measuring spot in dependence on the distance.	32
Figure 5.1. Experiment to estimate pyrometer response time. The film is heated up to 68°C. After stabilizing at that temperature, the door is opened and the sensor response to the temperature variation is collected.	35
Figure 5.2. Comparison between the experimental measurement normalized and the model step response.	36
Figure 5.3. Straw pacing specifications.	37
Figure 5.4. Relation between distance from surface and measured diameter (obtained from Optris® CTP3 datasheet)	37
Figure 5.5. Comparison between the temperature measured and the area inspected. On the bottom, a top view of the straws can be seen as a comparison.	38
Figure 5.6. Circular segment representation. The orange area A_s represents the sealed film area exposed to the pyrometer and the blue area represents the non-sealed area.	38
Figure 5.7. Film surface temperature variation with time, as the different film areas pass through the pyrometer measurement area. At $r = 1$, we have the sealed film temperature and at $r = 0$ we have the non-sealed film temperature.	39
Figure 5.8. Simulation of the system model time response to the surface measured temperature variation.	40
Figure 5.9. Simulation of the system model time response to the surface measured temperature variation for production at half speed.	40
Figure 5.10. Simulation of the system model time response to the surface measured temperature variation for production at normal speed, with pyrometer constant time $T=12.5$ ms.	41
Figure 6.1. Model representing the machine vision steps for image classification.	42
Figure 6.2. On the left: image of clear film sample; on the right: image of rugged film sample.	45
Figure 6.3. On the left: backlight lighting model; on the right: dome light lighting model [53].	46
Figure 6.4. Model representing pixel distribution according to the filter polarization angle [54].	46
Figure 6.5. Examples of images captured with backlight lighting. On the left: clear film; on the right: rugged film.	47
Figure 6.6. Examples of images captured with dome lighting. On the left: clear film; on the right: rugged film.	47
Figure 6.7. Model representing the steps of image preparation.	48

Figure 6.8. Four examples of the LBP described according to $P, RLBP$. The pixel values are interpolated when the sampling point is not in the center of the pixel [64].	50
Figure 6.9. Example of the calculation of LBP [66].	50
Figure 6.10. On the left: example of an image quantified in 3 gray-levels, sampled in 5x5 pixels; on the right: the correspondent GLCM, for a direction of 0° and a distance of 1. For instance, the value of the GLCM $F_{0,1} = 3$ was calculated by scanning the image of gray levels and finding the frequency where, for each pixel with a value of 0, its left or right neighbor pixel value was 1.	52
Figure 6.11. MLP diagram [78].	54
Figure 6.12. Model of a confusion matrix, where the classified images are divided into four groups: TP, FP, FN, TN.	55
Figure 7.1. Average F1 score for different levels of pixel radius.	58
Figure 7.2. Average F1 score for different number of neighborhood pixels.	58
Figure 7.3. LBP performance variation related with the number of artificial neurons.	59
Figure 7.4. On the left: variation of the number of gray-levels; on the right: variation of the direction angle.	60
Figure 7.5. Performance variation related with descriptors variation.	61
Figure 7.6. GLCM performance variation related with the number of artificial neurons.	62
Figure 8.1. Sample of 5 minutes of experimental pyrometer response in normal production conditions, with a zoom of 10 seconds.	65
Figure 8.2. Representation of the peak and valley temperature values in each iteration.	66
Figure 8.3. Sample of 2 minutes of experimental pyrometer response, in normal production conditions, in comparison to the model response, with a zoom of 10 seconds.	67
Figure 8.4. Comparison between the controller temperature and pyrometer temperature variation, for rugged film.	69
Figure 8.5. Comparison between the controller pressure and pyrometer temperature variation, for rugged film.	71
Figure A.1. On the left: diagram representing the sample dimensions; on the right: sample of film collected.	82
Figure A.2. On the left: a diagram representing the unsupported hold; on the right: a picture showing the specimen hold.	82
Figure A.3. Example of 3 different seal strength profiles.	83
Figure A.4. On the left: seal break; on the middle: seal tear; on the right: seal peel.	83
Figure B.1. Pyrometer support 3D model.	84

Figure B.2. Picture of pyrometer support. 84

Figure B.3. Pyrometer installation in the machine..... 85

Nomenclature

Greek Symbols

σ	Standard deviation
μ	Mean deviation
Φ	Energy flux
ρ	Reflectivity
α	Absorptivity
τ	Transmissivity
σ_{SB}	Stefan-Boltzmann constant
ε	Emissivity
θ_{dir}	Directional angle
λ	Wavelength

Roman Symbols

F_{max}	Maximum force
w	Seal sample width
q	Local heat flux density
k	Thermal conductivity
T_l	Local temperature
Q	Heat flow rate
A	Cross-sectional surface area
t	Time
h_c	Thermal contact conductance coefficient
x	Distance
T_{sr}, T_t, T_b, T_{sp}	Temperature at the different contact surfaces
T_{sf}	Surface temperature
T_∞	Room temperature
\bar{h}	Convection coefficient
q_{conv}	Convection heat transfer rate
E	Emissive power

J	Radiosity
G_{ref}	Reflective power
G_{tr}	Transmitted power
E_b	Emissive power of a blackbody
T_{abs}	Absolute temperature
G	First-order system model
G_{tc}	Pyrometer system theoretical continuous model
G_{td}	Pyrometer system theoretical discrete model
G_{ec}	Pyrometer system experimental continuous model
G_{ed}	Pyrometer system experimental discrete model
d_t	Distance between straws
d_e	Distance between consecutive straws
h_p	Pyrometer distance to film
d_p	Pyrometer measurement diameter
A_p	Pyrometer measurement area
v_p	Production velocity
A_s	Circular segment area
R	Pyrometer measurement radius
h	Distance to sealed area
r	Ratio between sealed and non-sealed areas
T_p	Peak temperature
T_v	Valley temperature
M	Number of points averaged in moving average filter
x_{MA}	Moving average filter input signal
y_{MA}	Moving average filter output signal
T_{LBP}	Local binary pattern texture descriptor
t_{LBP}	Local neighborhood texture
g	Gray level
s	Gray level difference
P	Number of equally spaced pixels
R_{LBP}	Local binary pattern radius
F	Normalized gray level co-occurrence matrix value
v_l	Speed of light
f	Wave frequency
T	Time constant

T_s Settling time
 NL Number of gray levels

Subscripts

0 Initial value
 c Central value
 p Pixel index
 i, j Matrix rows and columns indexes

Glossary

ACC	Accuracy
BOPP	Bi-oriented polypropylene
CON	Contrast
COR	Correlation
ENE	Energy
ENT	Entropy
FN	False negatives
FP	False positives
GLCM	Gray level co-occurrence matrix
HOM	Homogeneity
LBP	Local Binary Pattern
LED	Light-emitting diode
MA	Moving average filter
MLP	Multi-layer perceptron
PE	Polyethylene
PP	Polypropylene
PS	Polystyrene
SCG	Scaled conjugate gradient
SS	Seal strength
TN	True negatives
TP	True positives
USB	Universal Serial Bus

Chapter 1

Introduction

1.1 Motivation

The primary function of a package is to protect the product, through transportation, until its use. To better achieve this, packaging materials and processes have evolved through the years, to meet the changing needs of the industries and the consumers. From the use of rigid packaging, made from weaving, clay and metal, or the use of paper, it wasn't until the 20th century that plastic substrates appeared as a solution. The introduction of cellophane, invented in 1908 by Jacques E. Brandenberger, marks the beginning of the modern era of flexible packaging. Crystal clear film, appearing in 1927, transformed the market, allowing the consumer to see what was inside the package. From that point on, multiple types of films were discovered and developed according to the application needs [1], [2].

Biaxially Oriented Polypropylene, known as BOPP, was first developed by Imperial Chemical Industries in 1961. Polypropylene is a thermoplastic characterized by low density and good resistance to chemicals and to mechanical fatigue, being also an excellent moisture barrier. This material is commonly oriented to improve optical, mechanical, and barrier properties, becoming transparent, which makes it very useful for packaging [3].

The function of packaging, from an engineering perspective, is to protect the product from the environment until its use. This means the creation of a barrier that stops the environment conditions from interfering with the product quality, while also providing abusive resistance through the different steps of the supply chain. This barrier may involve the creation of hermetic seals, blocking light, or providing low permeation to gases such as moisture and oxygen. For the food industry, which englobes not only food products, but products that come into contact with them, packaging gains an even higher importance, being responsible for blocking any type of product contamination and avoiding harmful microbe growth, preventing spoilage and extending the shelf life [4].

In order to prevent the product from being contaminated, a good package seal is required. When it comes to plastic films, heat sealing is used, which involves the fusing of films together under heat and pressure. There are many different methods of heat sealing, which depend on the type and form of the structures being sealed, as well as the type of package and product. In the case studied in this thesis, conductance or thermal sealing is used, more specifically heat roller sealing, in which rollers apply heat,

through conduction, and pressure to the thermoplastic sealing layers. Proper seal formation requires the correct combination of these parameters [5], [6]. Too little of any of these will prevent an adequate seal from forming. The seal must be able to withstand the extreme environments it may be subjected to during shipping and handling. High altitudes may put pressure on the seal as the package expands due to the thinning of the air surrounding it, while extreme temperature variations may affect seal durability [3].

Over the years, the consumer importance given to the product quality has been increasing. This, together with the more restrict quality norms and regulations imposed to the industries, has seen companies investing in product quality assurance. This trend also applies to packaging, specially sealing quality. Companies have been motivated to look for and develop new and improved systems for sealing quality inspection. From the companies' point of view, sample testing is not enough anymore, and 100% quality inspection needs to be guaranteed. This is the base motivation for this thesis, which tries to propose different methods for in-line inspection of the film seal quality of straws packaging.

1.2 State of Art

As previously mentioned, with the increasing concern for sealing quality, over the years several approaches for film sealing quality inspection have been developed.

The most common forms of seal inspection still focus on destructive test methods applied to package samples. One of these methods is burst testing, where air is continuously added to a pouch sample containing the product until a specified pressure value is achieved. If the package bursts before this value is reached, the package fails, and subsequent tests are performed to determine where the problem arose. The burst test is a good overall test for seal strength because it stresses a package uniformly in all directions and identifies the location of the weakest point and the pressure at which it fails. An international standard for the application of this method is described in [9].

Another destructive inspection method widely used is tensile testing. In this method, each end of a seal is mechanically pulled until separation occurs, and the force that is required to accomplish this separation is recorded. If the force value is lower than the designated range, the package is considered to lack adequate seal strength. The tensile test is greatly used for the surveillance of material sealability and to spot-check equipment operations and sealing conditions [10]. The international standard for the application of this method can be found in [11].

Non-destructive methods, such as the mechanical squeeze test [12], the vacuum decay method [13] or the use of tracer gasses [14], can also be used for seal quality inspection. These methods, however, can only be applied to a small number of samples, making the detection of sporadic defects difficult, not guarantying 100% inspection, while also requiring manual labor from specialized workers. Because of this, companies have looked over the years for the search and development of in-line seal inspection systems, which should be non-destructive, fast and contactless.

Multiple methods of sealing inspection, based on different quality requisites, have been proposed throughout the years. Pascall et al.(2002) presented a study where the effectiveness of ultrasonic imaging for non-destructive assessment of seal strength in polymeric trays was investigated [15]. In this method, beams of ultrasound waves were sent into the seal area, and the reflections, or echoes, of these beams were received and processed by the system, creating an image for analysis. Ostyn et al. (2007) were able to detect wrinkles and solid contaminants in seals based on the analysis of the vibration pattern of sealing bars applied to statistical process control [16]. Morita et al. (2007) explored the potential of terahertz radiation in seal inspection. A focused beam was scanned along the sealed area and the transmitted signal was collected. Differences between the absorption coefficients of plastic and water and refraction index difference between plastic and air allowed the detection of fault seals. Song et al. (2014) evaluated the capabilities of high voltage in leak detection of flexible pouches, by measuring the discharge voltage when high voltages were applied to the sample packages [17].

From all the methods proposed, machine vision has been one of the most analyzed solutions. These systems have evolved significantly with the technology advances to tackle the challenges from modern manufacturing industry. Shuangyang (2010) studied the inspection of seal quality using machine vision [18]. Examples of acceptable and non-acceptable food packing seals images were analyzed, their uniformity was examined and associated with numerical quality measures and template matching was used for classification. Barnes et al. (2012) presented two imaging systems for detecting faults in heat seals of polymer trays, one using polarized light stress analysis and the other based on laser scatter imaging [19]. From the images obtained, the seal area was segmented and a very large set of candidate features, based on statistical information related to color and texture, was extracted. An adaptive boosting algorithm was then used to automatically select the best features and a classifier was trained to detect faults in different regions of the seal.

Thermal imaging is a specific method that can also have an application in sealing inspection. The first infrared-detecting cameras were developed around the year 1950, initially as a quite big apparatus for military purposes. It wasn't until the 1970s that smaller portable systems started to become available, enabling the use of infrared imaging for commercial and industrial applications. The enormous progress due to micro system technologies toward the end of the twentieth century resulted in reliable quantitatively measuring infrared camera systems. Infrared thermal imaging has now become affordable to a wider public for an ever-growing range of applications [20]. D'huys et al. (2016) studied the use of an active thermography method for seal contamination detection, where six different thermal image processing methods are compared [21].

1.3 Thesis Objectives and Contributions

The primary objective of this work is to identify a system capable of in-line inspection of BOPP film sealing quality in straw packaging, resulting in an inspection of all the products produced and a containment of any defect detected. This system also needs to be viable to be implemented in an industrial environment, fulfilling the requisites of the food industry regulations and safety norms.

This work was done in partnership with a plastic straw production factory, with the focus on its sealing system. In this factory, two different types of film, one clear and one rugged, are used and will be taken into account throughout this thesis. The straws packaging process will be studied and the sealing parameters that have an influence identified. The seal strength of sealed film samples, collected from the industrial environment, will be measured and will allow the definition of a production tolerance interval and the quantification of the different seal classifications.

To achieve the primary objective, two distinct solutions will be proposed. The first one includes a system for the measurement of film temperature after sealing using infrared pyrometers. The selection criteria of pyrometers and their influence in the final measurement will be presented. The system will aim to prove the relation between seal strength and film temperature after sealing, while also presenting a clear distinction in temperature measurements related to the different sealing conditions, allowing for seal quality classification.

The second solution proposed will be based on machine vision, where images collected from sealed film at different conditions will be analyzed. Two different imaging systems, one based on infrared lighting and the other on polarized filtering, will be tested. Two textural descriptors will also be proposed for image features extraction, based on the local binary pattern and the gray level co-occurrence matrix and for classification, a multi-layer perceptron neural network will be used. This work aims to analyze the capability of texture descriptors in describing the image features for classification, to compare the performances obtained with the different machine vision systems and the different descriptors, and to present a system with a good performance, allowing for seal quality classification.

1.4 Thesis Outline

Following this introductory chapter, Chapter 2 introduces the sealing process for straw packaging in analysis, together with a description of both films used. A study of the heat-sealing principle is presented together with the parameters that govern the process. The sealing defects and their causes are also explained.

In Chapter 3, a seal quality analysis is presented. The sealed film samples collected are identified and subject to a peel test according to the ASTM F88 procedure. From the results, the critical area of the film is identified, and the samples are classified according to their seal strength.

Chapter 4 presents a film temperature analysis. An initial experiment with thermistors is conducted and the results briefly explained. Following this, the important principles that govern thermal radiation are presented, together with the introduction of the pyrometry devices and their selection criteria. A brief application of a thermographic camera in sealing inspection is described, together with the application of a pyrometer.

In chapter 5, the pyrometer theoretical and experimental models are introduced, the latter being extracted from an experiment also described. The production and pyrometer installation parameters are

defined and a model of the film temperature variation, together with the pyrometer response to it are presented.

Chapter 6 introduces the machine vision solution step by step. Initially, the two types of image acquisition systems are described together with an explanation of the image preprocessing conducted. For feature extraction, texture analysis is introduced, and two descriptors based on the local binary pattern and the gray level co-occurrence matrix are presented. The methods used for image classification and performance evaluation are also presented.

Chapter 7 presents the results obtained with the two different textural descriptors applied to the two different image acquisition systems for the two different types of films, together with a comparison of their performances.

In Chapter 8, the installation of the pyrometer and experiments conducted are described. The results from normal production conditions are initially compared to the theoretical model deduced in Chapter 5, and a moving average filter for data processing is introduced. Finally, the results for temperature measure in relation to the production parameters are presented.

Chapter 9 presents the conclusions of this thesis and some suggestions for future work.

Chapter 2

Sealing Process Model

2.1 Factory production

The product in analysis in this thesis is plastic straws wrapped in film. The plastic straws pass through multiples steps of production, from extrusion to cutting and being corrugated, before being wrapped in plastic film. Multiple straws with different sizes and colors are produced and packaged right after they are finished.



Figure 2.1. Different types of straws.

The wrapping of the straws will be the focus of this work. In this process, the straws are placed between two layers of film, which are sealed together between two cylinders under pressure, where the sealing cylinder is heated at enough temperature to trigger the sealing process. The sealing of the film around the straw creates a small pocket for each one, creating a barrier between the straw and the environment, blocking any possibility for contamination.



Figure 2.2. Picture of the heat-sealing cylinder, together with the final product leaving the machine.

2.1.1 Packaging film

The focus of this thesis is in the packaging film, more specifically the sealed film area. To create a protective barrier around the straws, keeping them free from contamination, two layers of thin film are sealed together, creating a pouch around them.

The film used is made of coextruded bi-oriented polypropylene (BOPP), with three distinct layers: a core layer in the middle and heat sealable layers in both sides, with one side treated, as seen in figure 2.3.

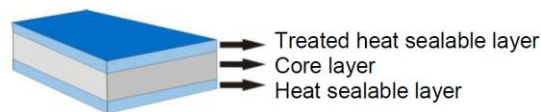


Figure 2.3. Packaging film model.

Polypropylene is a thermoplastic characterized by low density and good resistance to chemicals and to mechanical fatigue, including environmental stress cracking. It is also an excellent moisture barrier and has medium transparency. This type of film can be oriented, being stretched to produce some molecular realignment in the direction of the stretch. When oriented, its optical, mechanical, and barrier properties are improved and it becomes transparent, which makes it very useful for packaging [3].

The most important film characteristic relevant to this work is its thickness. The film's sealing initiation temperature is 105°C, at which the heat sealable layer starts to melt, which means that it is required for the film to reach at least this temperature for sealing to occur. In this thesis two different combinations of film will be analyzed.

2.1.1.1 Clear film

Clear film will be the term used to reference the use of two layers of BOPP film sealed together. These have a thickness of 18 µm and present a clear pattern throughout.

2.1.1.2 Rugged film

When the term rugged film is used in this work, it is in reference to the use of two layers of BOPP film sealed together, each with a thickness of 16 μm . The term rugged is chosen due to the film presenting, after sealing, a striped pattern. This is the result of using a sealing cylinder with the same striped pattern, as seen in figure 2.4.

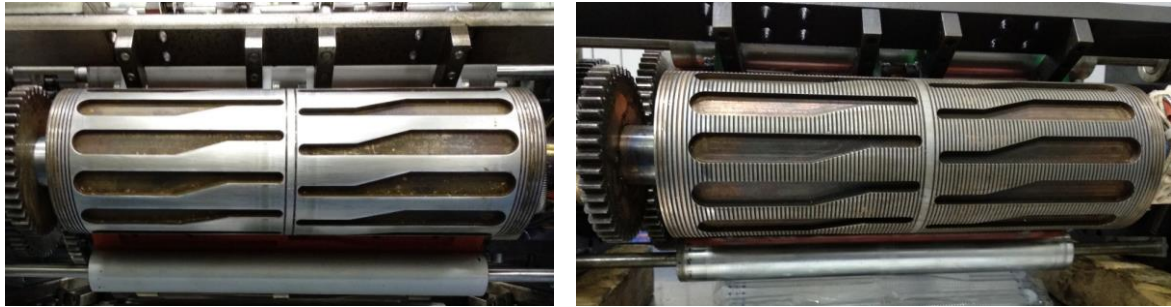


Figure 2.4. On the left: cylinder for clear film; on the right: cylinder for rugged film.



Figure 2.5. On the left: clear film packaging; on the right: rugged film packaging.

2.2 Heat sealing process

Heat sealing involves welding thermoplastic polymer surfaces together in order to produce seals of sufficient strength to withstand stresses in the distribution and consumer environment. There are many different methods of heat sealing, which depend on the type and form of the structures being sealed, as well as the type of package and product. Some types of heat sealing include conductance or thermal, impulse, dielectric, induction or ultrasonic sealing [4].

The principle behind these types of sealing is the same. The sealing layer is exposed to heat and pressure, and begins to melt, leading to a more intimate contact between the two sealing surfaces. Given enough time and pressure, molecular segments diffuse across the interface and reorganize,

forming entanglements within the polymer chains, destroying the interface and producing a homogenous layer that remains homogeneous after cooling, resulting in a chemical bond, as represented in figure 2.6. The higher the bond, the higher the seal strength.

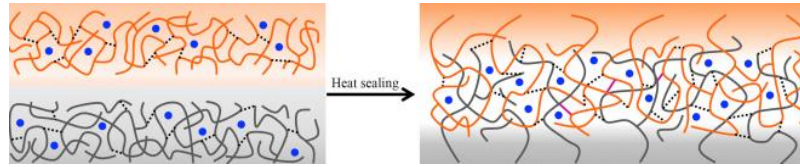


Figure 2.6. Model representing molecular entanglements in heat sealing processes [1].

In this work, the sealing process analyzed is conductance or thermal sealing, more specifically heat roller sealing. In this process, rollers apply heat, through conduction, and pressure to the thermoplastic sealing layers.

Often, after the contact time, the heat seal materials are still molten and the seal does not have its full strength, but the materials must be able to adhere to each other well enough to insure the integrity of the seal. The full strength of the seal develops as it cools to ambient temperatures [8].

2.2.1 Conductance sealing principle

In conductance sealing, the transfer of thermal energy which occurs between the heat-sealing plate and the multiple layers of packaging material is essential towards understanding how the seal process happens and the strength of the seal itself. An equation that can properly represent the rate of heat transfer through a multi-layered body is Fourier's Law of heat conduction.

2.2.1.1 Fourier's Law of heat conduction

Fourier's law provides a mathematical correlation between thermal conductivities of the various materials used in the sealing process, the heat being transferred through the system and the change in temperature that it originates [22]. Equation (2.1) represents Fourier's law in its differential form, with q being the local heat flux density in $W \cdot m^{-2}$, k being the material's thermal conductivity in $W \cdot m^{-1}K^{-1}$ and ∇T the local temperature gradient in $K \cdot m^{-1}$.

$$q = -k \cdot \nabla T_l \quad (2.1)$$

When equation (2.1) is integrated for a homogeneous material of one dimensional geometry between two endpoints at constant temperature, it appears as equation (2.2), with Q as the heat flow rate in W , A as the cross-sectional surface area in m^2 , ΔT as the temperature difference between the ends in K and Δx as the distance between the ends in m .

$$\frac{\Delta Q}{\Delta t} = -kA \frac{\Delta T_l}{\Delta x} \quad (2.2)$$

2.2.2 Heat flow resistances

In equation (2.2) it was assumed a single homogeneous material. However, that is not the case in the sealing process. As described in figure 2.3, the film possesses three distinct layers. This results in different thermal conductivity values. However, for the sake of simplicity, a single thermal conductivity value will be assumed for the entire film.

Another factor that needs to be taken into account is that, in the sealing process, the heat flow passes through different independent objects. When passing between two objects in direct contact with one another, contact resistance surges.

Contact resistance appears because, due to differing surface metrologies, it is highly unlikely that two materials are in full contact. Instead, pockets of vacuum or air can form in-between them, as represented in figure 2.7, resulting in an increase in the thermal resistivity of the overall system. These cavities result in the need to consider new resistance terms besides those of the materials themselves, where there may not only be conduction occurring, but convection and radiation as well.

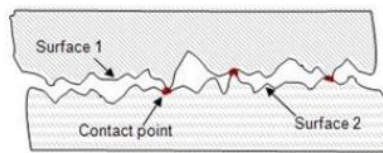


Figure 2.7. Representation of contact resistance. Due to the irregular surface of the materials, full contact is never achieved [22].

This new resistance term can be described as a relation of the thermal contact conductance coefficient h_c , which represents the ability to conduct heat between two bodies in contact.

2.2.3 Heat roller sealing model

In this work, heat roller sealing is studied. In this process, the heat flow originates from a heated roller, usually made of a metal with high thermal conductivity, passing through both films which are pressured against another roller. A model of the process can be seen in figure 2.8.

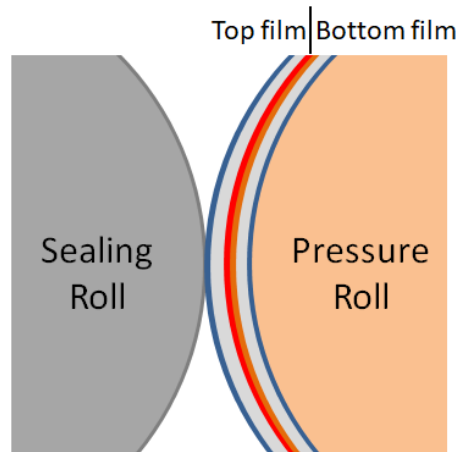


Figure 2.8. Model representing the sealing process. Both films are pressured between the rolls. The heat sealable layers are represented at red and orange.

The temperature distribution throughout the different components is represented in a simplistic way in figure 2.9. Due to contact resistances, temperature drops can be seen at the contact between the rolls and the films and between the two films. The temperature at the film is also always lower than the temperature at the sealing roll's surface.

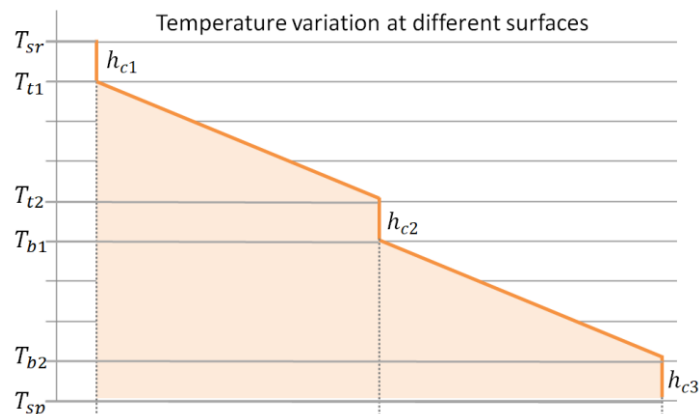


Figure 2.9. Graphic representing the temperature variation between the two rolls. T_{sr} represents the temperature at the surface of the sealing roll, T_t represent the temperatures at the surfaces of the top film, and T_b the temperatures of the bottom film.

The areas of interest in this process are the surfaces of the films' treated heat sealable layers. These will be the regions where the sealing initiation temperature needs to be reached in order for the sealing process to occur.

From Fourier's law and the law of energy conservation, considering the initial point as the heat roll surface temperature T_{sr} and the end point the temperature of the bottom film T_b , the heat flow rate Q can be described in equation (2.3). k is the film's thermal conductivity, h_{c1} and h_{c2} are the thermal contact conductance coefficients between the sealing roll and the top film and between both films respectively, Δx is the thickness of the film and A is the cross-sectional area of the film being sealed.

$$\frac{\Delta Q}{\Delta t} = \frac{T_{sr} - T_b}{\frac{1}{h_{c1} \cdot A} + \frac{\Delta x}{k \cdot A} + \frac{1}{h_{c2} \cdot A} + \frac{\Delta x}{k \cdot A}} \quad (2.3)$$

However, this equation is only a simplistic representation of the heat flow throughout the sealing process. In practice, the heat flow is not uniform. Temperature variations from changes in position and passing time influence this parameter. A transient heat transfer model is described in [23]. Free or natural convection, which represents the cooling of a body due differences in densities between hot and cooler air, can also have an impact in this value.

Despite this, equation (2.3) allows us to evaluate which parameters can have an influence in the heat flow that reaches the sealing layers. Changes in these parameters can be related to changes in the seal strength

2.2.3.1 Film related parameters

Looking at the film characteristics, there are several parameters that can have an influence in the sealing quality. Looking at equation (2.3), variations in the films thickness Δx has an influence in the heat flow. Also, a change of the film's thermal conductivity k can happen due to unwanted production or treatment conditions while an increase in the film's roughness can also impact the thermal contact conductance coefficient h_c .

Despite the influence that the film's characteristics have on the quality of the sealing process, these are inspected and verified by the manufactures and are very unlikely to be the cause of sealing problems. In this work, it will be assumed that the film maintains its characteristics constant.

2.2.3.2 Parameters related to the sealing process

When it comes to sealing quality problems related to the sealing process, they are usually a consequence of an error in the three main defining parameters: temperature, dwell time and pressure.

The temperature parameter corresponds to the temperature of the sealing roll surface when it comes in contact with the film. Dwell time refers to the period of time where the sealing roll is in contact with the film. Both of these parameters are directly related to the amount of heat that is transferred to the sealing interface, as seen in equation (2.3). If either the temperature or the dwell time are not high enough, the sealing layer might not achieve the sealing initiation temperature required for sealing to start.

The third parameter is the pressure at which the equipment brings together and holds the two films to form the seal. If not enough pressure is applied, the real contact area decreases significantly, decreasing the thermal contact conductance coefficient h_c , which has a negative impact in the heat transferred to the film.

Changes in these parameters can produce a significant variability in seal strength. Due to this issue, throughout the years, multiple experimental studies have been conducted with the objective of relating the sealing process parameters with the resulting film's seal strength.

Yuan and Hassan [24] performed an experimental study on the effect of sealing parameters on the heat seal strength of OPP film. In this study they confirmed that, after the seal initiation temperature, the strength of the heat seal increased sharply with platen temperature before reaching the maximum strength value at a certain temperature, termed the plateau initiation temperature. It was also confirmed that the platen temperature and dwell time are interrelated in obtaining the heat seal strength. However, platen temperature plays a more important role as compared to dwell time since the interfacial temperature is primarily controlled by the platen temperature, while dwell time has to be sufficiently long to ensure that enough heat is transferred to the sealing interface in order to melt the sealing layer.

A pressure related study is also described in [24]. It was concluded that for small pressure values no sealing occurred. However, with a slight increase, sealing occurs, not being required a major difference in pressure for the seal strength to reach its highest level. At a higher pressure setting after this point, no significant change of seal strength with pressure is detected. Other researchers have also confirmed these results applied to different types of polymers [25]–[28].

There is, however, a negative effect related to the increase of temperature. If the platen temperature value is too high, fusion of the film's core layer may initiate, which leads to a fragilized film, with a reduction of its flexibility and maximum tensile strength. As such, a platen temperature interval has to be defined and obeyed to guarantee a strong seal.

In this work, due to the nature of the process being studied, dwell time will be assumed as constant, since all the machines during normal production work at their maximum velocity, not being possible to accelerate them, which would be the way for dwell time to impact the sealing quality.

2.3 Sealing defects

Sealing defects occur when the sealing strength is lower than the tolerance defined. This corresponds to the force necessary to separate both films after sealing. When this strength is low, we have what we call weak sealing, where it is easier to open the straw pouch. Any small force, either from product transportation or application in the package, can make the straw pocket open, leaving the straw vulnerable to contamination, creating a health hazard for the consumer.

Defective products due to sealing quality, as previously mentioned, are a consequence of a change in the sealing process parameters. This unexpected parameter variation can be a result of multiple causes.

One of the reasons for sealing defects is component malfunction. Subject to high temperature and pressure, the components tend to either deteriorate over time or fail catastrophically. The variability of the components wear rates and the difficulty to conduct their inspection, due to difficult access, makes

it extremely difficult to predict when a failure might happen. A small component malfunction, due to the dependency they have on each other, has an impact on the entire system, possibly leading to defects.

The unevenness of the temperature distribution across the sealing cylinder surface can also have an impact on the sealing process. This is a consequence of the heating supplied by the resistances inside the sealing cylinder, which emit more heat in the middle when compared to the edges. Measurements of the surface temperature, conducted with an infrared thermometer, detected a temperature variation up to 8°C. This temperature distribution increases the difficulty in controlling the process, requiring more strict parameter tolerances.

Another frequent reason for sealing defects comes from human error, either by interference with the system or failure to follow the procedures, especially the cleaning and inspection of the system. The film, when heated to high temperature, tends to leave some particles that become attached to the sealing cylinder. After many hours of production, these particles accumulate, creating a barrier around the cylinder that decreases the area of contact with the film and the thermal conductivity, consequently decreasing the heat that reaches the sealing layers, impacting the sealing process.

All the reasons for sealing defects described above can be directly related to either a change in temperature or pressure in the sealing process. In this paper, in order to recreate the production of defects, the variation of these two parameters will be taken into account.

Chapter 3

Seal Quality Analysis

In order to differentiate what is defined as good sealing and weak sealing, it is required to analyze the film sealing strength. This is the characteristic that is used to quantify sealing quality and is used in all industries where film sealing is present, such as the food and medical industry. Due to the high norms and restrictions that these industries are subject to, standards for seal strength analysis are set in place worldwide.

For this analysis, it will be taken into account the ISO 11607-1:2019 norm [36], which includes the ASTM F88 procedure [11]. This procedure describes the standard test method for analysis of the seal strength of flexible barrier materials [34], [37]–[39]. Summing up, it states that small rectangular shaped samples of the sealed film should be collected and subject to a peel test, in which each film is slowly striped apart from each other, collecting data related to the maximum force required for the film's separation. A more detailed description of the norm and the procedure followed can be found in appendix A.

3.1 Sample collection

For sealing quality analysis and distinction, multiple sets of samples were collected from two different machines in the production area. One, which will be referred to as machine A, that produces straw with clear film, and another, which will be referred to as machine B, that produces straws with rugged film. In each machine, sets of samples were collected at different working production conditions, varying the sealing temperature and pressure parameters in defined intervals. The parameter values used for sample collection and a qualitative analysis of each of them, performed by the factory's machine operator, can be seen in tables 3.1 and 3.2.

	Controller temperature [°C]	Controller pressure [MPa]	Qualitative classification of sealing
Machine A – Clear film	115	0.50	Good sealing
	115	0.40	Good sealing
	115	0.30	Weak sealing
	115	0.25	Really weak sealing
	115	0.20	Lack of sealing
	110	0.50	Good sealing
	105	0.50	Weak sealing
	100	0.50	Really weak sealing
	95	0.50	Lack of sealing

Table 3.1. Sample collection parameters and qualitative sealing analysis for clear film. The machine's normal working conditions are at 115°C and 0.5 MPa.

	Controller temperature [°C]	Controller pressure [MPa]	Qualitative classification of sealing
Machine B – Rugged film	130	0.50	Good sealing
	130	0.30	Weak sealing
	130	0.25	Really weak sealing
	130	0.20	Lack of sealing
	120	0.50	Weak sealing
	115	0.50	Really weak sealing
	110	0.50	Lack of sealing

Table 3.2. Sample collection parameters and qualitative sealing analysis for rugged film. The machine's normal working conditions are at 130°C and 0.5 MPa.

Analyzing the sealing qualitative classification, it is expressed that: good sealing means that the product is up to the factory standards; weak sealing means that it is possible to observe that the sealing is weaker than the standard defined; really weak sealing means that the product is not up to standards and would result in a customer complaint; lack of sealing means no sealing actually occurred between the films, having the straws left the pockets on their own. To samples classified with lack of sealing it is not possible to apply the seal strength analysis test. For these, the force required to break the seal will be considered approximately zero.

3.2 Seal strength experimental results

Just as described in appendix A, the samples collected were subjected to a peel test. From this test it was possible to obtain data related to the seal profile, which compares the films separation, in millimeters, with the force required to do so, in Newtons. Analyzing this data, it is possible to obtain the

seal strength SS , in N/mm, calculated according to equation (3.1), where F_{max} is the maximum force applied and w is the width of the film samples [37].

$$SS = \frac{F_{max}}{w} \tag{3.1}$$

For each temperature or pressure change, this value was calculated as the average of the values obtained from each test conducted.

3.2.1 Critical area identification

As previously described in chapter 2, the temperature distribution at the sealing cylinder surface is not constant, but higher in the middle and lower in the edges, which can lead to an uneven seal strength distribution throughout the film.

To confirm this assumption, multiple samples from clear film qualified as weak sealing (105°C, 0.5MPa) were tested, according to the following distribution seen in figure 3.1. A distribution of the samples seal strength can be seen in figure 3.2.

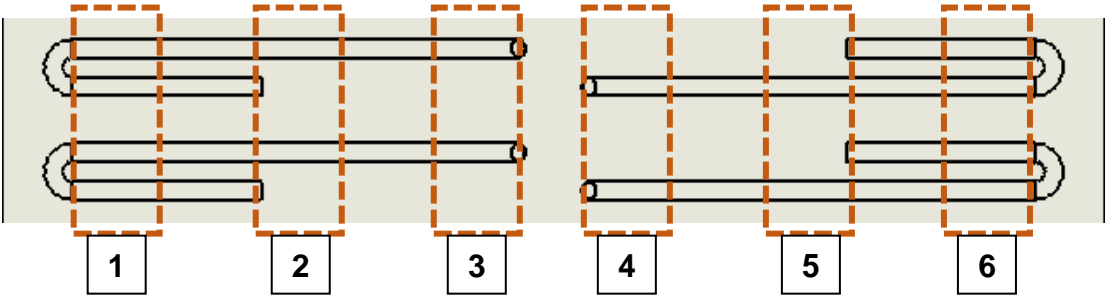


Figure 3.1. Distribution of the samples collected throughout the film length.

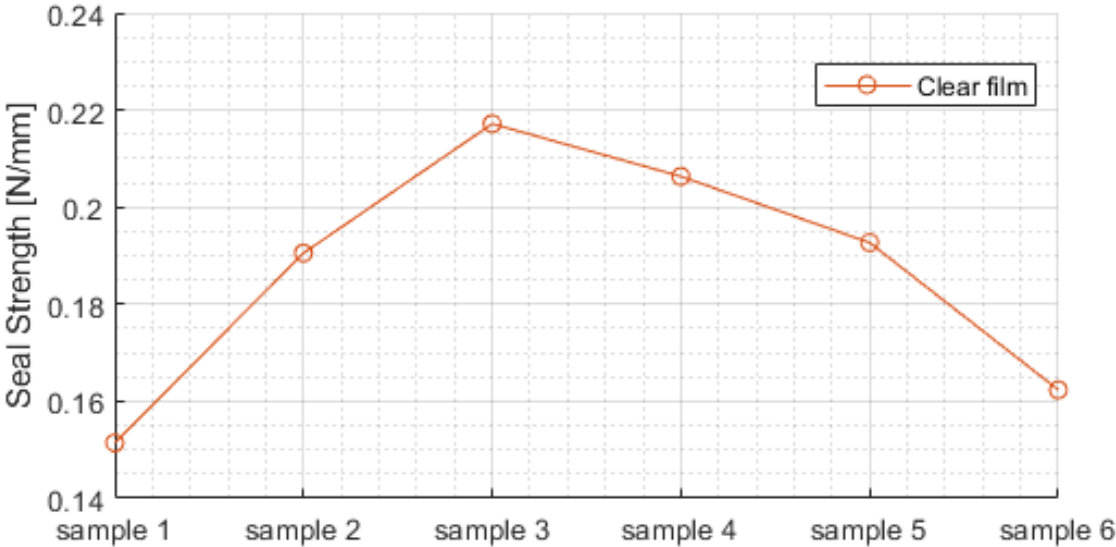


Figure 3.2. Seal strength distribution according to sample area collected.

Analyzing the results, it is possible to confirm that the sealing cylinder surface temperature distribution has a direct correlation to the film seal strength. This confirms that, throughout the film length, the sealing critical area will be at the film edges, next to the straw corrugation. This will be the area of focus for the next chapters.

3.2.2 Relation between sealing parameters and seal strength

To analyze the relation between the temperature and pressure parameters change and the consequent seal strength, strips of film from the critical area, according to sample 1 described in figure 3.1, were collected from each of the samples, obtained with parameters variation, and subjected to a peel test.

An evolution of the films seal strength, as a result of the sealing parameters, can be seen in figures 3.3 and 3.4. For both the clear and rugged films, in their specification sheets, it is present the film minimum sealing strength expected, at standard sealing conditions, with a value of 0.157 N/mm.

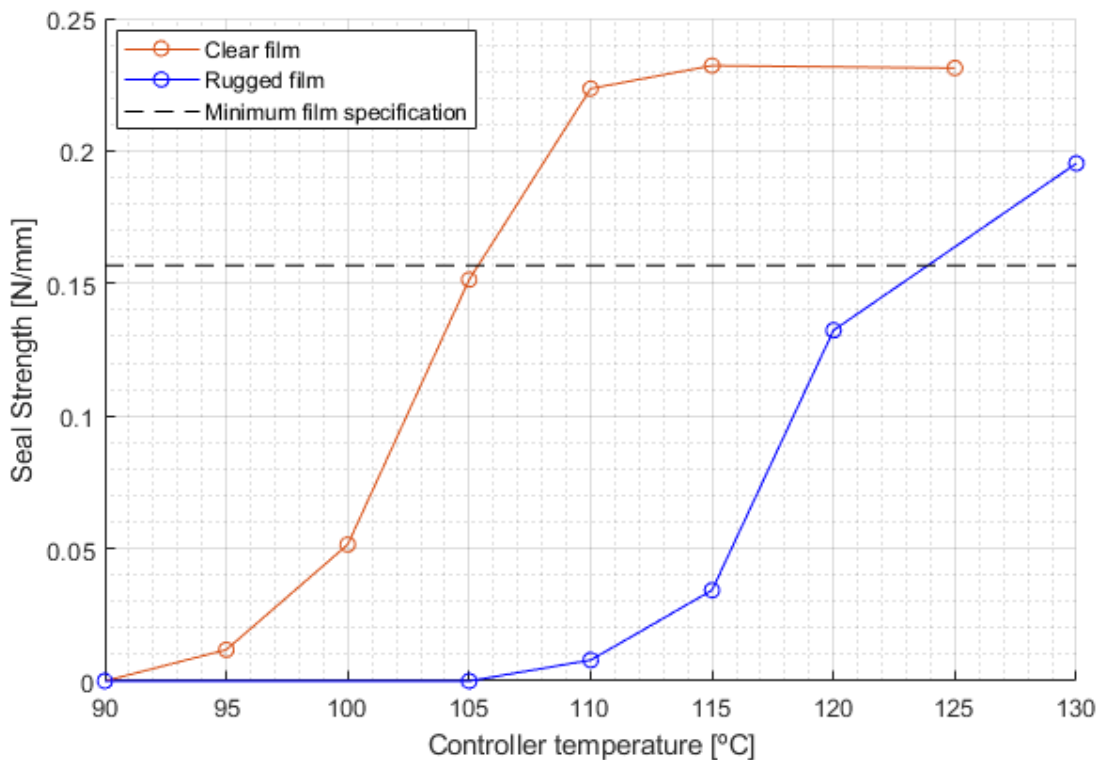


Figure 3.3. Evolution of seal strength according to the sealing temperature.

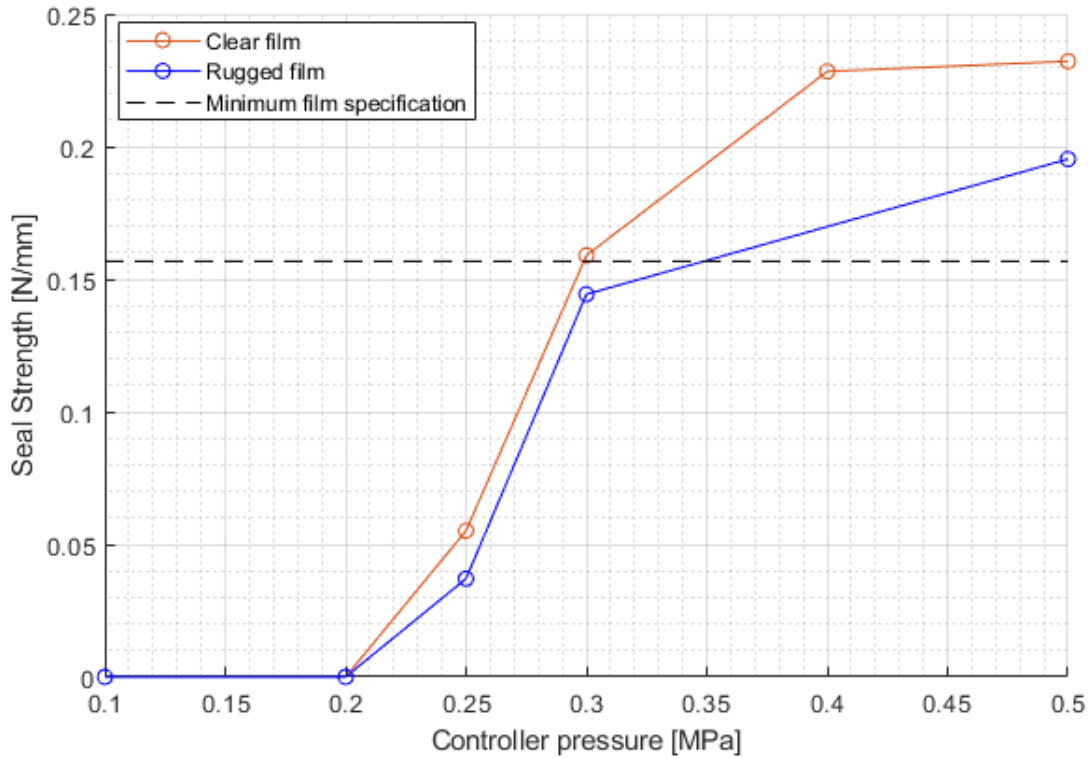


Figure 3.4. Evolution of seal strength according to the sealing pressure.

Analyzing the graphics obtained, it is possible to confirm that the qualitative analysis of the sealed film samples matches the seal strength values obtained. Good sealing is only considered for temperature and pressure conditions where the seal strength reaches a plateau value. This is the value considered by the factory as standard. Any deviation from it, even if still close to the film's minimum specifications, should not be approved and should be identified as not valid. The reason is that, between production and the product reaching the customer, it passes through different stages that can deteriorate its quality, reducing the initial seal strength. Vibration caused by transportation or harsh storage conditions can impact the chemical bond created in the film sealing.

Even though the seal strength evolution shows a high slope between what was qualified as really weak and weak sealing, the difference between weak and good sealing becomes less apparent. In the following chapters, different methods for film sealing in-line inspection will be described and their capacity to make this distinction will be evaluated.

Chapter 4

Film Temperature Analysis

As already described in chapter 2, the sealing process is responsible for transmitting energy to the materials being sealed. In this case, the energy is transmitted as heat to the BOPP films being sealed together. All the parameters responsible for a good seal have an influence on the amount of heat that is transferred to the films.

The heat transferred will have an influence on one parameter that will be discussed in this chapter: the temperature of the film after the sealing process. This condition allows us to relate the quality of seal with the final temperature of the film after sealing. This hypothesis will be the base of the work described in this chapter.

In order to test the hypothesis that the final temperature of the film can be directly correlated with the quality of the seal and used as an inspection method, different ways of measuring film temperature were tested, as described in the next sub-chapters

4.1 Thermistors in temperature analysis

The simpler way to measure the temperature of an object or environment is to use thermometers. These devices when exposed to a different temperature suffer a change in their properties that can be measured, indicating the temperature value. One type of thermometer frequently used is a thermistor. These sensors are semiconductors with an electrical resistance that changes in response to temperature, depending on its material, allowing temperature estimation.

Since these types of devices require contact with the object being measured, it is not possible to measure the temperature of the film during production. However, if the film temperature is different after the sealing process, it can be assumed that the air temperature immediately around the film will also change, due to a variation in the convective heat transfer rate q_{conv} , defined in equation (4.1), as a result of the product between the average convection coefficient for the entire film surface \bar{h} , the surface area A and the variation in temperature between the film surface and the environment [22].

$$q_{conv} = \bar{h} \cdot A \cdot (T_{sf} - T_{\infty}) \quad (4.1)$$

Detecting changes in the temperature of the air immediately around the film with thermistors might correlate to changes in the film temperature. To test this assumption a simple experiment was conducted in industrial environment, as follows.

4.1.1.1 Experiment results

For this experiment, three DS18B20 temperature sensors [41] were placed over the film, at the machine's exit, with another sensor placed far from the machine's exit to control room temperature. To test the assumption that changes in the film temperature can be related to changes in air around it, the temperature and pressure sealing parameters were varied, and their impact measured.

Looking at the results, it was possible to conclude that it is not viable to detect differences between weak and good seals. The results showed little to no differences in temperature values measured with sealing parameters changed, which makes this method invalid for sealing quality classification. Since heat propagation is slow, the sensors also have a response time to variations in temperature of several minutes, making them unreliable for this application.

In conclusion, changes in the film temperature are not high enough to cause a measurable variation in the temperature of the environment around it. As such, it is necessary to measure the temperature of the film directly after the sealing process. This will be the base topic of the next sub-chapter.

4.2 Radiation pyrometry in temperature analysis

Radiation pyrometry, also known as radiation thermometry or infrared thermometry, is a powerful method of temperature measurement based on a simple principle: every body at a temperature superior to the absolute zero (> 0 K) emits electromagnetic radiation. The amount of radiation and its distribution as a function of wavelength depend on temperature and material properties. Analyzing the radiation emitted allows the estimation of the body surface temperature.

This is where pyrometry methods bring a huge advantage in comparison to more conventional ones, since they do not need mechanical contact with the inspected component and provide an almost instant measure of the temperature value. Pyrometry methods are also not sensitive to vibrations, do not perturb the temperature field and are immune to electrical interference, allowing for a remote and nondestructive inspection.

The great advantages of these characteristics made pyrometry a very rapidly evolving field in science as well as industry, owing to the enormous progress made in the last three decades in

microsystem technologies of IR detection. Nowadays, it is applied in research and development as well as in a variety of different fields in industry, such as non-destructive testing [42].

4.2.1 Thermal radiation

As previously said, all matter with a temperature over absolute zero emits thermal radiation, since it is composed of particles with kinetic energy, which interact with each other. These kinetic interactions among matter particles result in the electrodynamic generation of coupled electric and magnetic fields. This leads to the emission of photons, radiating energy away from the body through its surface boundary, defined as thermal radiation. These photons move at the speed of light and behave according to the known optical principles. They can be deflected, focused with a lens, or reflected by reflective surfaces. For temperatures in the range of natural and technological processes, this radiation is included in the thermal infrared spectral region, between 0,8 and 14 μm . For this reason, this radiation cannot normally be seen with the naked eye.

The energy flux Φ , in Watts, radiating from an object surface into the hemisphere around it can be defined as radiant power. Considering the object surface with area A , we can define emissive power, E (W/m^2) as the rate at which radiation is emitted from a surface per unit surface area, over all wavelengths and in all directions.

$$E = \frac{d\Phi}{dA} \quad (4.2)$$

At the same time, radiation from the surroundings, which may consist of multiple surfaces at various temperatures, is also incident upon the object. The rate at which radiation is incident upon the surface per unit surface area, over all wavelengths and from all directions is defined as irradiation G (W/m^2).

When radiation is incident upon a semitransparent object, portions of the irradiation may be reflected, absorbed, and transmitted. Transmission refers to radiation passing through the object. Absorption occurs when radiation interacts with the object, causing an increase in the internal thermal energy of the medium. Reflection is the process of incident radiation being redirected away from the surface, with no effect on the object itself. We define reflectivity ρ as the fraction of the irradiation that is reflected, absorptivity α as the fraction of the irradiation that is absorbed, and transmissivity τ as the fraction of the irradiation that is transmitted. Because all of the irradiation must be reflected, absorbed, or transmitted, it follows the relation in equation (4.3).

$$\rho + \alpha + \tau = 1 \quad (4.3)$$

If we consider all the radiant energy leaving the object surface, we define radiosity J (W/m^2) as the sum of the emissive power with the reflected power and the transmitted power.

$$J = E + G_{ref} + G_{tr} \quad (4.4)$$

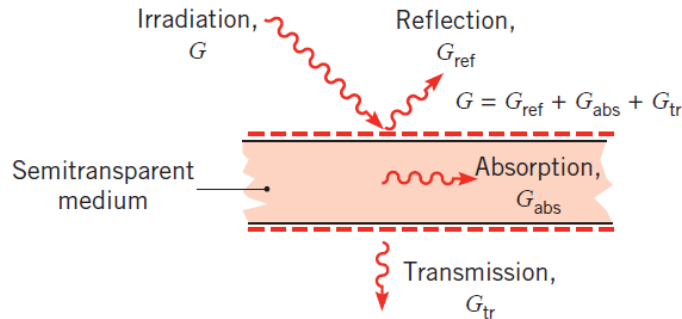


Figure 4.1: Semitransparent medium model [22].

The previous definitions were established in relation to the energy flux across all directions. However, most often surfaces of objects do not emit radiation uniformly in the hemisphere. The previous equations were also established in relation to the energy flux of all wavelengths. Just like the direction, surfaces of objects do not emit radiation uniformly across all wavelengths.

4.2.1.1 Blackbody

A blackbody is idealized as an object which absorbs all incident radiation, regardless of wavelength and direction. For a prescribed temperature and wavelength, no surface can emit more energy and, although the radiation emitted by a blackbody is a function of wavelength and temperature, it is independent of direction. As the perfect absorber and emitter, it serves as a standard against which the radiative properties of actual surfaces may be compared, since no other surface as precisely its properties [20].

Stefan-Boltzmann law defines the total emissive power of a blackbody E_b as directly proportional to the fourth power of the absolute temperature.

$$E_b = \sigma_{SB} T_{abs}^4 \quad (4.5)$$

4.2.1.2 Emissivity

In reality, real objects are rarely a black body, though in certain spectral intervals they may behave closely to it and can only emit a part of the radiation a black body emits at the same temperature and same wavelength. Emissivity is defined as the ratio of the radiation emitted by the surface to the radiation emitted by a blackbody at the same temperature.

$$\varepsilon = \frac{E}{E_b} \quad (4.6)$$

Knowing the emissivity value allows us to rewrite equation (4.5), relating the total emissive power of real bodies with their temperature.

$$E = \varepsilon \sigma_{SB} T_{abs}^4 \quad (4.7)$$

While equation (4.7) is simple in form, its simplicity is deceptive in that the emissivity itself depends on the spectral and directional characteristics of the surface emission. The change in directional characteristics can, however, be neglected for small angles. For nonconductors materials, such as plastic, the emissivity value is almost constant for $\theta_{dir} \leq 70^\circ$ [22].

4.2.1.3 Kirchhoff's law of thermal radiation

While the exact value of emissivity in a given scenario can be very difficult to decipher, good approximations of this value can be obtained with simpler methods. One of these is based on Kirchhoff's law of thermal radiation, that states that for a body in thermodynamic equilibrium, the emissivity is equal to the absorptivity. This is described in equation (4.8).

$$\varepsilon = \alpha \quad (4.8)$$

Replacing equation (4.3) in equation (4.8), we have:

$$\varepsilon = 1 - \rho - \tau \quad (4.9)$$

Being emissivity an important variable in pyrometry applications, measurements have been performed to determine these properties for many different materials and surface coatings and standard values have been approximately defined [43].

4.3 Pyrometry devices

As previously mentioned, in order to estimate the objects surface temperature, the intensity of the radiation emitted by it is analyzed. This is the basic principle behind pyrometry devices.

The core part behind these devices is the detector, which converts the infrared radiation received into electrical signals, and allows temperature estimation. The quality of the detector largely determines the performance of the system.

Infrared detectors fall into two main groups: thermal detectors, which are based on the change in a physical property of a semiconductor material, and quantum detectors, which interact directly with the impacting photons that lead to changes in the concentration of the free charge carriers in the detector. The quantum detectors are wavelength dependent and can detect the temperature of a remote object's surface by measuring the amount of IR incidence of a specific range. Unlike thermal detectors, they offer quicker response time and better detection performance. More information regarding the physical principles of these detectors can be found in [20].

4.3.1 Pyrometers

A pyrometer is a device that, based on the principles described earlier, can measure the temperature of a small surface area. It is constituted by an optical system, which picks up the thermal radiation emitted from a circular surface area and focuses it on a detector. The temperature value measured results in an average of the area inspected.

The optical resolution is defined as the relationship between the distance of the measuring device from the target, and the diameter of the spot. The greater this value, the better the optical resolution of the measuring device, and the smaller the target can be at a given distance. The target must completely fill the inspected area, otherwise other thermal radiation from the background will make the measured value inaccurate.

4.3.2 Thermographic cameras

Thermographic cameras work based on the same principles as pyrometers. However, their main purpose is not to very accurately obtain the average temperature of a small inspection area. Instead, they convert IR radiation of a large surface area into a false color visual image, which represents its two-dimensional temperature distribution.

There are two main types of imaging system available to the IR thermography. Scanning systems consist of either a single-element IR detector or a linear detector array, rastered across the desired field of view to construct a 2-D image. On the other hand, focal plane arrays, depending on their size and resolution, use thousands of individual detectors arranged in a matrix, similar to a typical camera, capturing the 2-D image directly projected by the lens. The focal plane array is superior to scanning array in almost every aspect in terms of performance, since it allows higher frame rates at higher pixel numbers [20].

In comparison with pyrometers, thermographic cameras bring major advantages when it comes to industry use, allowing for a complete inspection of the temperature distribution of the surface, leading to the discovery of small abnormalities, which can be related to defects in the object. However, it also presents a few disadvantages since it requires a computer unit for signal and imaging processing, which

requires a larger installation space, and has a price many times higher. Pyrometers are also more accurate at measuring the temperature of an object.

4.3.3 Selection criteria

When selecting a pyrometric system, a few criteria have to be taken into account, depending on the performance that is required. The most important criteria are the measurement temperature range, resolution, uncertainty and repeatability required, the size of the area being inspected and distance the surface, the response and acquisition time, the operating temperatures and the spectral range.

For IR imaging, only a small range of the IR spectrum is used. Typically, three spectral ranges are defined for thermography: the long-wave (LW) region from around 8 to 14 μm , the mid-wave (MW) region from around 3 to 5 μm , and the short-wave (SW) region from 0.9 to 1.7 μm .

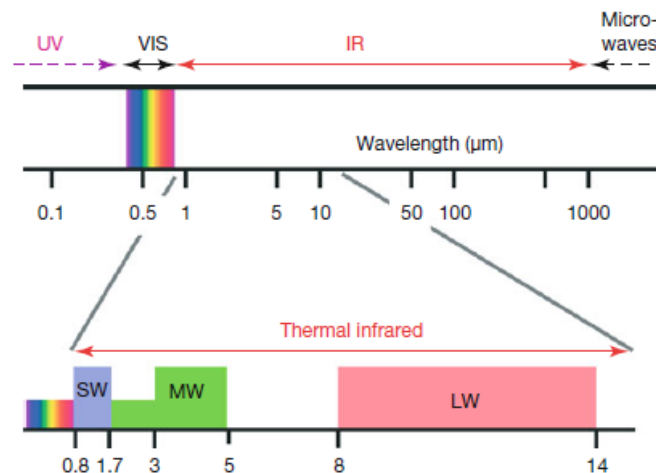


Figure 4.2: Spectral ranges used in radiation pyrometry [20].

All criteria have to be carefully defined and compared with values present in the equipment datasheet, before its selection.

4.4 Pyrometry applied to sealing inspection

A diverse number of industries already resort to pyrometry for sealing quality inspection. With focus in food and pharmaceutical industries, where any type of contamination of the product can have major implications, seal integrity inspection is of most importance.

With the use of thermal imaging, industries can analyze the heating distribution throughout the seal, looking for abnormal patterns that indicate a defective seal. This includes the presence of contaminants, folds or wrinkles in the seal. This combination of precision and non-invasiveness makes

thermal imaging suited for seal verification of any kind of flexible packaging such as sachets, pouches, stick packs or blisters [43].

Pyrometers, even though they are less flexible and offer a smaller inspection area, still bring major advantages in some applications, where only a small inspection line is required to take conclusions regarding the quality of product, due to their lower price and size.

4.4.1 Pyrometry applied to BOPP film

As discussed previously in this chapter, a possible way to reach a conclusion regarding the sealing quality of the film is through the analysis of its temperature. This is possible using pyrometry devices since, like all other materials, the film emits a continuous stream of thermal radiation from its surface, and its intensity can be measured and related to the surface temperature.

However, due to some of the film inherit properties, in order to achieve a valid measurement of the temperature, several conditions have to be met, due to the many variables that can influence this measurement process, such as the spectral emission characteristics of polypropylene, optical performance, interference sources or environmental parameters [44].

One of the most important parameters to be defined revolves around the film emissivity. Accurate temperature measurement requires precise knowledge of this quantity, since it directly correlates to the temperature value displayed by the device. The correct value is necessary for its correct calibration.

A simple way to estimate this parameter is based on Kirchoff's law. As described in equation (4.9), emissivity depends on the values of reflectivity ρ and transmissivity τ . When it comes to plastics, a good approximation for reflectivity is $\rho = 0.04$, independent of wavelength. Reflectivity is also independent of material thickness [42].

Estimating the transmissivity value, however, is a harder task, since it is dependent not only on the wavelength of radiation, but also on the type of material and object thickness. It is most effective to design an installation which results in using the highest emissivity value possible.

When it comes to thin-film plastics, they tend to be transparent at many wavelengths, which relates to high transmissivity values. This allows radiation from objects behind the film to pass through and influence the measured intensity. To contradict this situation, the wavelength measured by the device should be carefully selected, to assure that the transmissivity value is as low as possible.

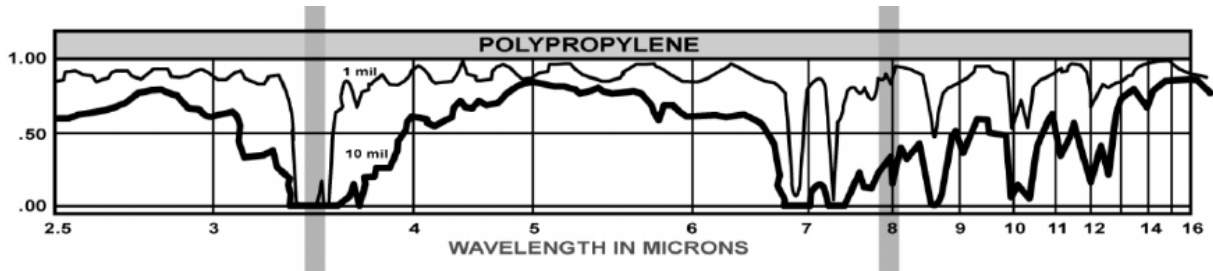


Figure 4.3. Diagram representing the relation between the wavelength and the polypropylene transmissivity [20].

The study relating the wavelength of radiation with the transmissivity of the polypropylene has been developed in controlled conditions. The results are plotted in figure 4.3. Analyzing the graphic, we can conclude that, for really thin polypropylene film, only in a very specific wavelength does the transmissivity reaches values really close to zero. This wavelength is $3.43 \mu m$. Due to the importance of this parameter, special pyrometric infrared sensors have been developed by companies focused in this technology, that are especially designed for the temperature measurement of thin polypropylene film and only measure the radiation intensity in the $3.43 \mu m$ wavelength.

Assuming the transmissivity value as zero in this wavelength, we can estimate the emissivity value in equation (4.10).

$$\varepsilon = 1 - \rho - \tau = 1 - 0.04 - 0 = 0.96 \quad (4.10)$$

When selecting the correct radiation wavelength where intensity is to be measured, another factor needs to be taken into account. For accurate measurement, it is necessary that none of the radiation emitted by the film is absorbed on its path to the pyrometric device. This, however, can happen in the spectral regions of atmospheric absorption bands. Some gases present in great quantities in the atmosphere, such as water vapor (H_2O) and carbon dioxide (CO_2) can absorb radiation in specific wavelength, as described in figure 4.4.

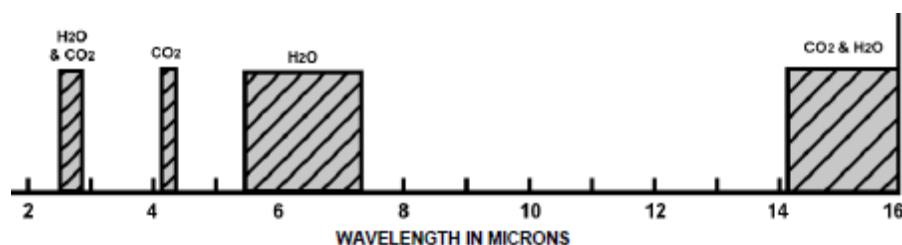


Figure 4.4. Diagram representing the relation between wavelength and atmospheric gas absorption [20].

However, analyzing the figure 4.4, we can conclude that the $3.43 \mu\text{m}$ wavelength, defined previously as the specific wavelength for polypropylene, is not part of the spectral regions of atmospheric absorption bands, having no influence in the measurement system.

In harsh working environments, dust, smoke, and suspended matter in the atmosphere can result in contamination of the optics, blocking parts of the radiation stream and, therefore, leading to false measured values. Planned maintenance and cleaning of the device is necessary to maintain its good function.

4.5 Pyrometry equipment application

4.5.1 Thermographic camera

In order to conduct an initial analysis of the possibilities of this type of technology, a simple test was conducted with a thermographic camera Optris® Xi 400. This small size rugged device is considered an entry-level thermographic camera, capable of temperature measurements between 20°C and 900°C . With a FPA detector and a 390:1 optical resolution, produces a video of 382×288 pixels, with a frame rate of 27Hz. It detects radiation in the 7.5 to $13 \mu\text{m}$ wavelength, obtaining temperature values with an accuracy of $\pm 2\%$ [45].



Figure 4.5: Thermographic Camera Optris® Xi 400

In the experiment, the temperature of the film surface opposite to the one in contact with the sealing cylinder was measured, immediately after the machine's exit. The camera was connected to a laptop through a USB connection and the resulting video was obtained with the use of "Optris® PIX Connect Software". The video shows the continuous flow of straws passing through the camera field of view. The temperature distribution values remain quite constant throughout the test, with a repeatability error of around $\pm 2^{\circ}\text{C}$. As an example, a single frame of video is shown in figure 4.6.

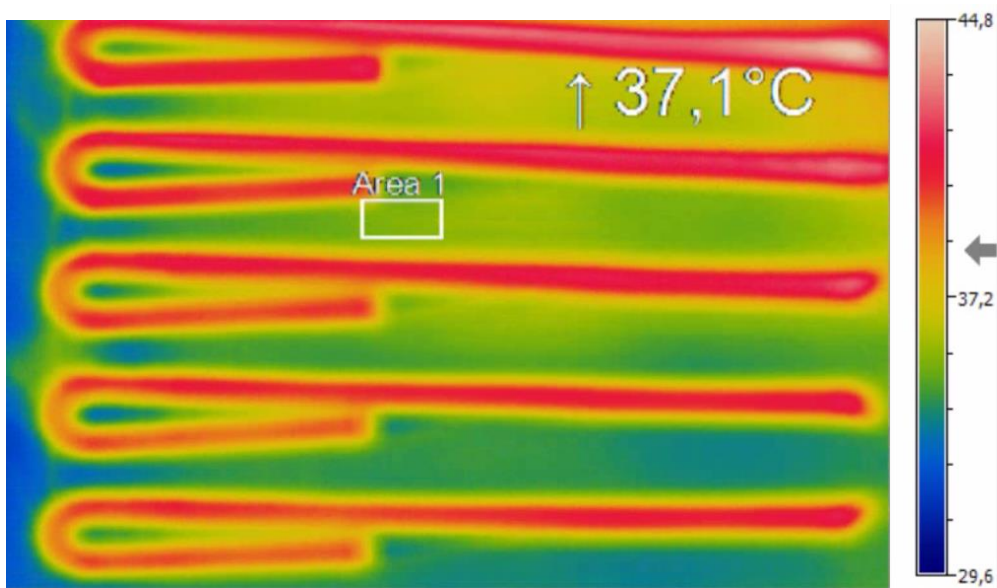


Figure 4.6: On the left: video frame captured; on the right: color legend related to temperature

The main conclusion that can be extracted from this test is that, with radiation detection in the long-wave infrared region, from around 8 to 14 μm , it is not possible to obtain accurate values of the surface temperature of the film. This happens because, as previously explained, for really thin film, as is the case, the transmissivity values in this spectral range are really high, reaching values of 0.9 in some wavelengths, as can be seen in figure 4.6. High transmissivity values imply that most of the radiation that reaches the detectors actually came through the film instead of being from its surface, which induces a major error in the results.

This film transparency due to high transmissivity can easily be seen in figure 4.6, where, despite the straws being covered by BOPP film, their shape can clearly be detected in the image. This implies that the radiation detected by the camera is actually emitted by the straws and completely transmitted through the film.

Another reason that proves this assumption is that the area of film sealed is not the point of highest temperature, showing lower values than the straws. This occurrence proves the inability of the camera to detect the correct temperature of the film, even without any object immediately behind it.

This simple test was especially important in this study, proving that the more general sensors, that measure in the long-wave infrared region and are far less expensive, are not appropriate for this application. It proves the necessity of using a specific sensor for polypropylene film, despite the higher investment.

These specific sensors, as previously mentioned, should detect radiation only in the 3.43 μm wavelength, which becomes quite difficult since thermographic cameras that can do this are not only very scarce in the market but also incredibly expensive. To contradict this, a different solution revolves around the use of pyrometers.

4.5.2 Pyrometer

As previously explained, pyrometers work based on the same principal of thermographic cameras but are only capable of inspecting a really small surface area and extracting the average temperature value of it.

In spite of only being able to obtain the temperature value of what is basically a single surface point in time, this does not invalidate their use in film sealing inspection. As described in chapter 3, it is not necessary to obtain the entire surface temperature distribution to reach a conclusion regarding quality of seal, since due to the heating distribution in the sealing process, sealing problems always appear first in the critical area. As such, it can be assumed that inspecting the temperature in this area is enough to reach a conclusion.

Since a pyrometer is capable of measuring the temperature in a certain spot in a specific period of time, in theory, as the continuous of film and straws produced pass through the pyrometer inspection field of view, it is possible to obtain the temperature values of the critical area over time.

Looking at the types of possible defects and their critical areas, which englobe the film on top of the straw and between straw corrugations, to cover all possible defects two pyrometers should be implemented, one for each side of the film, as described in figure 4.7.

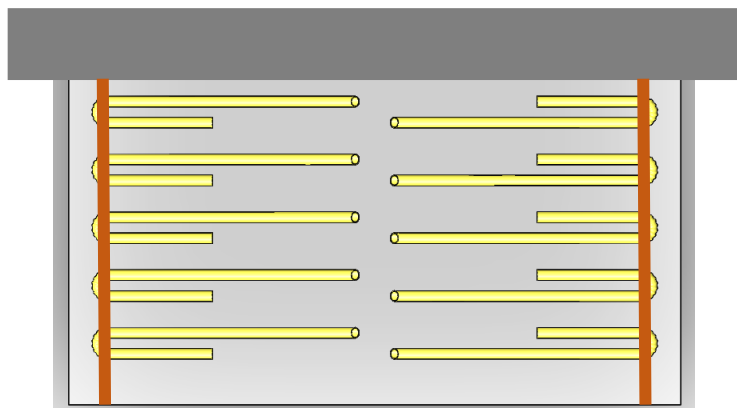


Figure 4.7. Diagram representing the film leaving the machine. At orange: inspected line by the pyrometers.

To test this assumption, a pyrometer Optris® CTP3 was used. This sensor was specially developed for precise temperature measurements of thin plastic films made of PE, PP or PS, detecting radiation only in the $3.43 \mu\text{m}$ wavelength. It is capable of measuring temperatures of 50°C to 400°C and enduring up to 75°C , being one of the best devices in the market for this application. It also comes with an alarm option, sending a signal whenever a condition is verified, according to its programming [46]. This alarm signal can be sent directly to the machine, stopping the production and reducing the product waste created.



Figure 4.8. Pyrometer Optris® CTP3.

However, it has a few characteristics that might invalidate its applicability in this process. The first one is based on its optical parameters. The distance between straw corrugations is 8 ± 1.5 mm, which corresponds to the critical area. Taking a look at the optical parameters of the pyrometer in figure 4.9, we can estimate that in order for the area of inspection to only include sealed film, the sensor as to be placed at 30 mm or less from it. Due to the small tolerance between these two dimensions, it is very likely that in some measurements, the field of view will include non-sealed area which will influence the measured temperature.

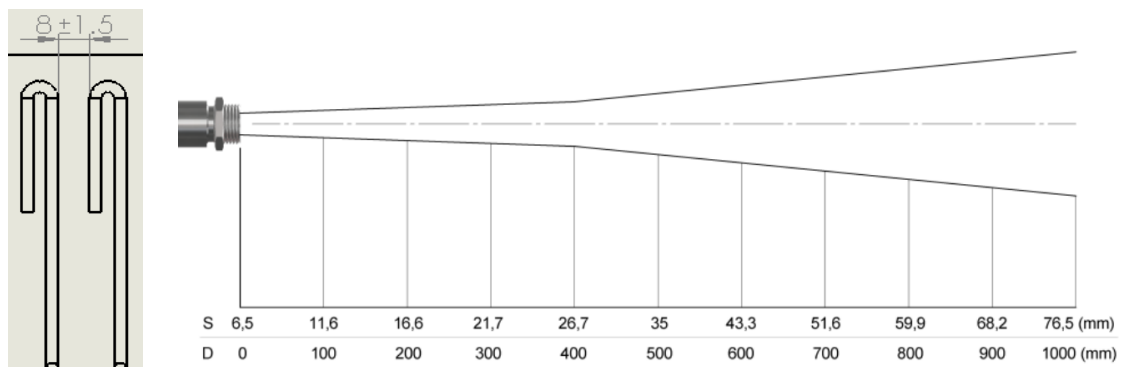


Figure 4.9. On the left: Straw drawing; on the right: relation between the diameter of the measuring spot in dependence on the distance.

Another important characteristic of the pyrometer is its accuracy of $\pm 3^\circ\text{C}$. As described previously in chapter 3, small variations in the sealing wheel temperature or pressure applied can be enough to originate weak sealing. However, the influence that these parameters have in the resulting temperature of the film after sealing might not be large enough to compensate the error resulting from the sensor accuracy, invalidating the results. The pyrometer repeatability of $\pm 1.5^\circ\text{C}$ can also induce errors in the measured temperature.

The distance at which the pyrometer is placed from the sealing process is also an important factor in this implementation. The higher the distance, the more time the film has to cool, which, depending on the ambient temperature, can highly diminish the variation between weak and good sealing temperatures, resulting in the sensor inability to distinguish them. The pyrometer should also be

placed in a direction normal to the film surface, since this direction corresponds to its highest emissivity point.

The characteristics described above can lead to measurements errors in some instances. However, since sealing problems are process dependent, they don't occur in only a small number of instances, but in a large sample of continuous product. As such, instances where false values are obtained can be ignored with signal processing.

If the sensor is placed over the straw's corrugation, as described in figure 4.7, in theory the measured temperature in relation to time should resemble a sinusoidal wave, where the peak values correspond to the film surface temperature between straws and the lower values correspond to the film over the straws. In this application, only the peak values are important and related to sealing quality.

An estimation of the pyrometer model, the evaluation of its behavior in sealed film temperature measurement and the results obtained will be analyzed in the following chapters.

Chapter 5

Pyrometer Model

In order to predict how the pyrometer will behave in measuring the film surface temperature after sealing, during normal production, its model and temperature response were studied.

A pyrometer, just like most temperature sensors, can be estimated as a first-order system, in whose input-output equation is a first order differential equation.

$$G(s) = \frac{1}{Ts+1} \quad (5.1)$$

To define the system model, time constant T must be estimated. This will be done in two different ways, a theoretical way where the constant used is the one present in the pyrometer datasheet, and an experimental way where the time constant is estimated.

5.1 Theoretical model

In the Optris® CTP3 sensor datasheet, the sensor settling time, T_s equals 100 ms. From this value it is possible to estimate the time constant T as a quarter of it, as seen in equation (5.2).

$$T = \frac{T_s}{4} \quad (5.2)$$

As such, we can assume $T=25$ ms. This defines the system theoretical model as:

$$G_{tc}(s) = \frac{1}{25s+1} \quad (5.3)$$

or in its discrete form, obtained using zero-order hold on the inputs with a sample time of 1ms:

$$G_{td}(z) = \frac{0.04144}{z-0.9586} \quad (5.4)$$

5.2 Experimental model

In temperature sensors, the settling time defined by the manufacturer not always corresponds exactly to the real response time of the sensor, being typically a value below the average obtained from tests on multiple sensors. To validate the model previously described, an experiment was conducted using the Optris® CTP3 sensor, to evaluate its response to temperature changes.

In this experiment, a sample of film with straws was placed in a hoven and heated at 68°C for 15 minutes, giving it enough time to reach this temperature uniformly. The sensor is placed normal to the film surface and covered by an object at room temperature. After the temperature of the film is stable, the hoven door is opened, and the object blocking the sensor is removed. The sensor is subjected to a temperature variation between room temperature and film temperature and its response over time is saved for processing. To assure the validity of the experiment, the procedure was conducted eight times, with intervals of 3 minutes in between to assure the film temperature was stable.

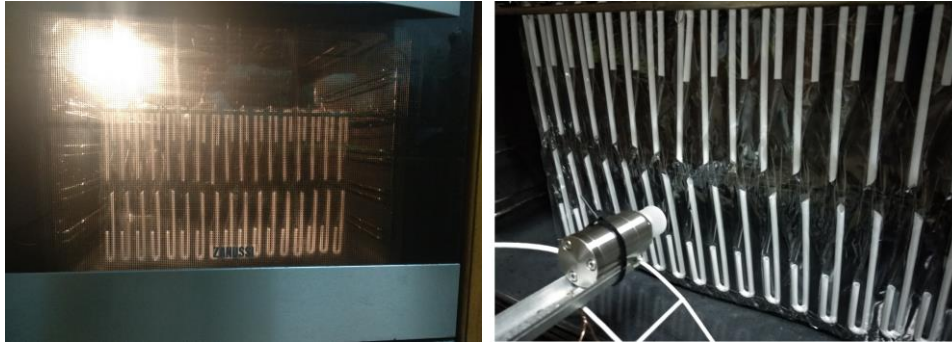


Figure 5.1. Experiment to estimate pyrometer response time. The film is heated up to 68°C. After stabilizing at that temperature, the door is opened and the sensor response to the temperature variation is collected.

The sensor response over time can be analyzed as a first-order system step response. From this, it is possible to estimate the system settling time T_s as the time required for the sensor to reach 98.2% of the temperature variation. An average of the different tests conducted was considered.

	mean	σ
Settling time T_s [ms]	91.75	15.84

Table 5.1. Experimental model mean settling time. σ represents the standard deviation.

From equation (5.2), we can estimate the time constant T required to define the system as $T = 22.94$ ms.

$$G_{ec}(s) = \frac{1}{22.94s+1} \quad (5.5)$$

or in its discrete form, obtained using zero-order hold on the inputs with a sample time of 1ms:

$$G_{ed}(z) = \frac{0.04266}{z-0.9573} \quad (5.6)$$

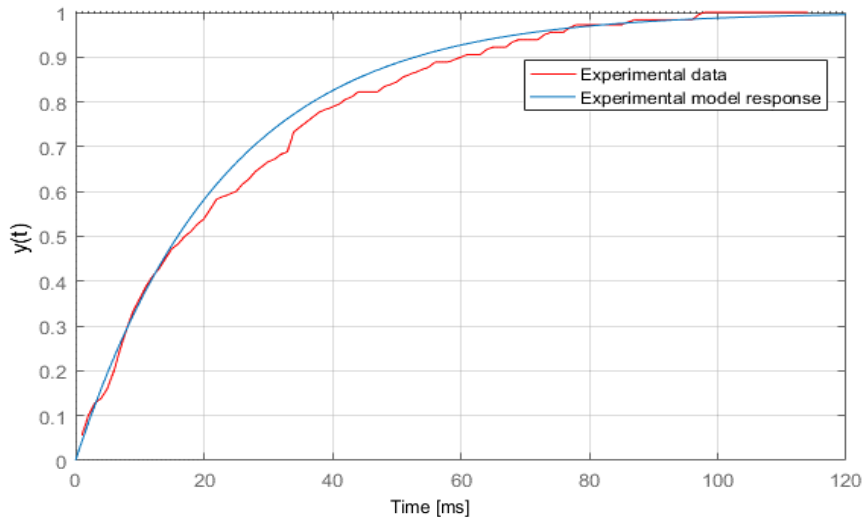


Figure 5.2. Comparison between the experimental measurement normalized and the model step response.

From this point forward, the experimental model G_e obtained will be used.

5.3 Production process implementation

As previously defined, the main objective for the pyrometer installation is to measure the temperature of the sealed area surface in the critical area. To do so, the sensor is pointed at the critical area, measuring continuously the film temperature through the sealed and non-sealed area. As previously mentioned, it is not possible to measure only sealed area at any time since the distance between straws is smaller than the minimum distance the sensor can measure.

5.3.1 Film surface temperature variation

To measure the film surface temperature, the pyrometer is fixed normal and as close as possible to the film surface and to the sealing process. The pyrometer, however, doesn't measure only a single spot but a small area. The temperature value measured results in an average of the area inspected.

With the sensor fixed, as the film passes through, the area measured includes sealed film and non-sealed film (pouch area). As such, the temperature values obtained will not be constant, but oscillate between a low and a high temperature value.

To estimate this oscillation, a few parameters must be defined. Straw and film specifications are defined as a standard by the factory.



Figure 5.3. Straw pacing specifications.

Distance between straws [mm]	d_s	8 ± 1.5
Distance between consecutive straws [mm]	d_t	$22^{+0.0}_{-0.5}$

Table 5.2. Straw specifications

Pyrometer distance to the film is also an important factor. In this work it is placed at 10 mm, as close as possible, to reduce the measurement area, without coming into contact with the film. The pyrometer measurement diameter can then be estimated according to the pyrometer specifications, as seen in figure 5.4.

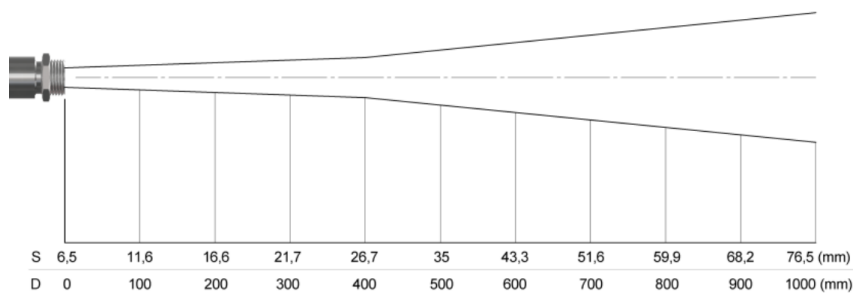


Figure 5.4. Relation between distance from surface and measured diameter (obtained from Optris® CTP3 datasheet)

Pyrometer distance to the film [mm]	h_p	10
Pyrometer measurement diameter [mm]	d_p	7
Pyrometer measurement area [mm²]	A_p	38.48

Table 5.3. Parameters related to pyrometer measurement.

It is also necessary to define the production velocity. This can be done accurately with an initial experiment with the pyrometer. As seen in figure 5.5, when a temperature valley is measured means that a straw passed through the sensor. Counting the number of valleys over a period of time allows us to estimate the production velocity.

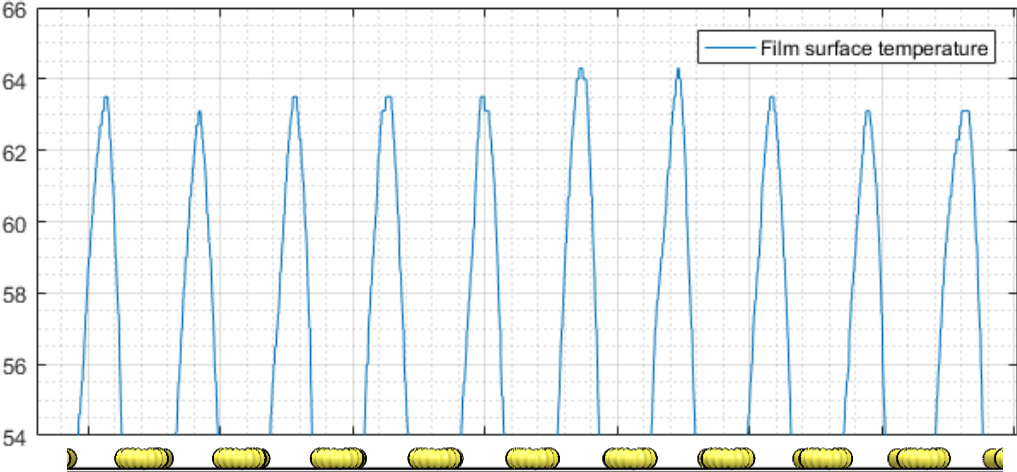


Figure 5.5. Comparison between the temperature measured and the area inspected. On the bottom, a top view of the straws can be seen as a comparison.

Production velocity [mm/s]	v_p	60.85
-----------------------------------	-------	--------------

Table 5.4. Production velocity estimated.

When estimating the temperature variation, it is assumed that each area, sealed and non-sealed, presents a uniform temperature throughout.

As the film passes through the pyrometer measurement area, part of this area belongs to sealed film, while the other belongs to non-sealed film. The ratio between these parts can be estimated based on the circular segment area mathematical formula, described in equation (5.7) and represented in figure 5.6.

$$A_s = R^2 \cos^{-1} \left(\frac{R-h}{R} \right) - (R-h)\sqrt{2Rh - h^2} \tag{5.7}$$

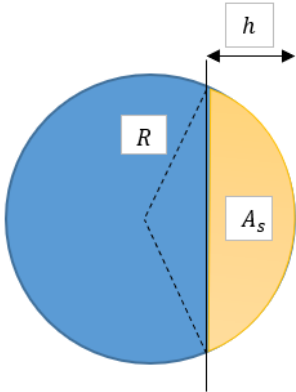


Figure 5.6. Circular segment representation. The orange area A_s represents the sealed film area exposed to the pyrometer and the blue area represents the non-sealed area.

With $R = \frac{d_p}{2} = 3.5 \text{ mm}$ and h defined as time dependent t .

$$h(t) = v_p \cdot t = 60.85 t \quad (5.8)$$

Knowing the circular segment area, we can relate it with the total measurement area to obtain the ratio $r(t)$ between temperatures over time.

$$r(t) = \frac{A_s(t)}{A_p} \quad (5.9)$$

When the area corresponds to entirely sealed film, $r = 1$, and when the area is entirely non-sealed, $r = 0$. The ratio variation over time for a straw cycle is described in figure 5.7.

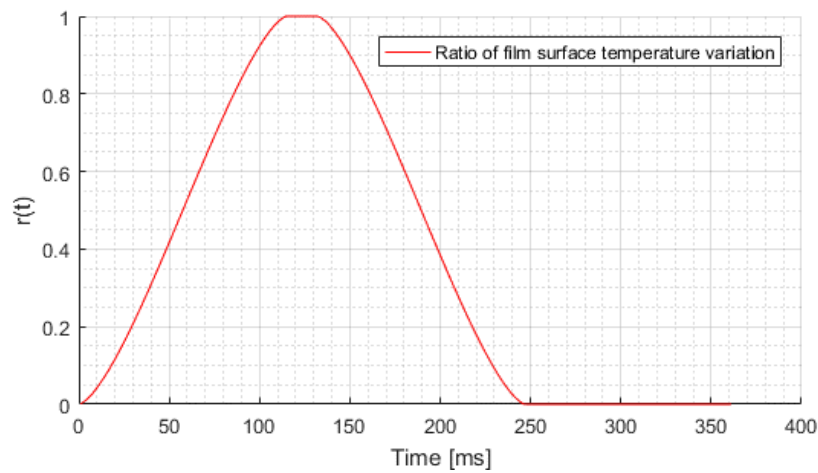


Figure 5.7. Film surface temperature variation with time, as the different film areas pass through the pyrometer measurement area. At $r = 1$, we have the sealed film temperature and at $r = 0$ we have the non-sealed film temperature.

5.4 Pyrometer model response to film temperature variation

Having estimated the pyrometer model and knowing the theoretical surface temperature variation of the film, it is possible to analyze the model dynamic response for this input. This response is described in figure 5.8.

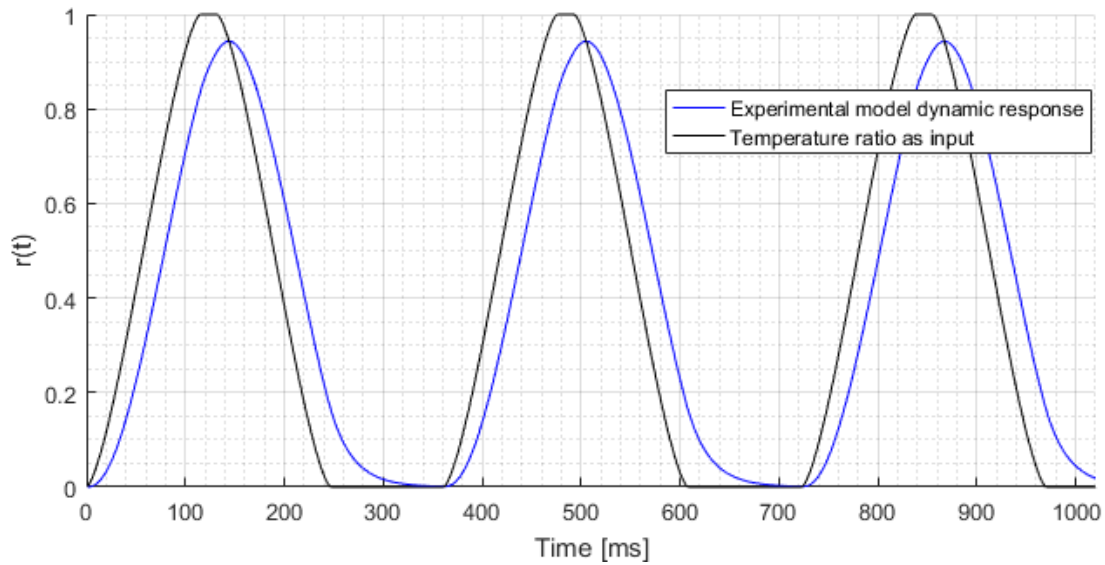


Figure 5.8. Simulation of the system model time response to the surface measured temperature variation.

It is possible to see that the system model cannot keep up with the surface temperature variation. Due to the production high velocity and the small distance between straws, the pyrometer is not exposed enough time to the sealed film between straws to reach the sealing maximum temperature. A constant error of 5.68% is always present.

To reduce this error, there are two theoretical solutions possible. The first one would be the reduction of the production velocity. For example, at half production speed, the constant error between the maximum temperature measured and the sealed film temperature would be reduced to 0.99%, as seen in figure 5.9.

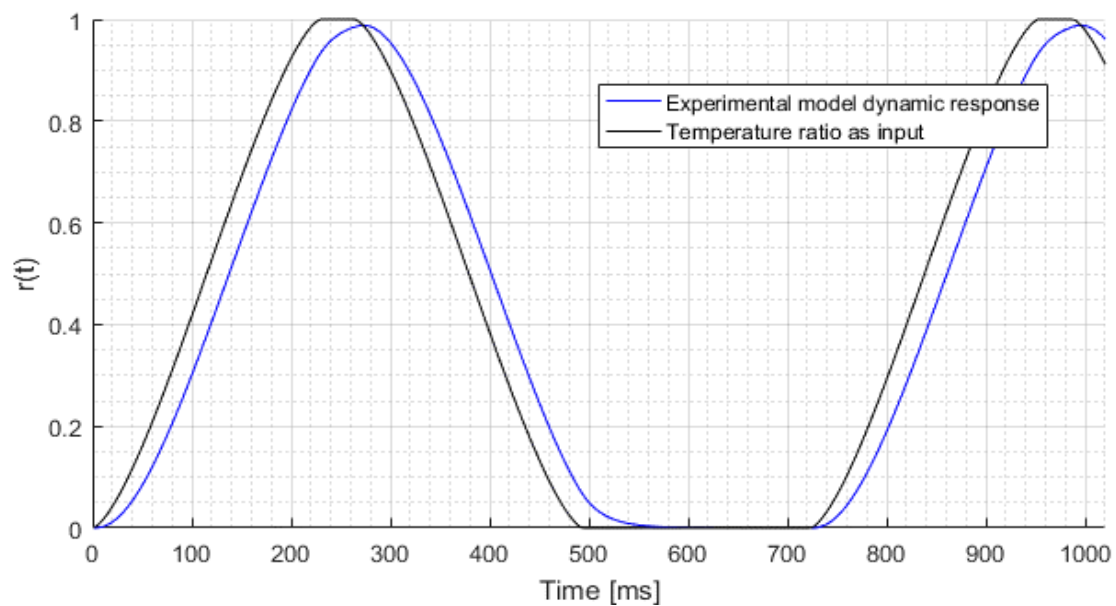


Figure 5.9. Simulation of the system model time response to the surface measured temperature variation for production at half speed.

In practice, however, a production speed reduction to half is not possible due to the major impact it would have on production efficiency.

The other solution would be to use a pyrometer with a faster response time. To guarantee a constant error smaller than 1.5%, the pyrometer would require a constant time $T < 12.5 \text{ ms}$, as seen in figure 5.10.

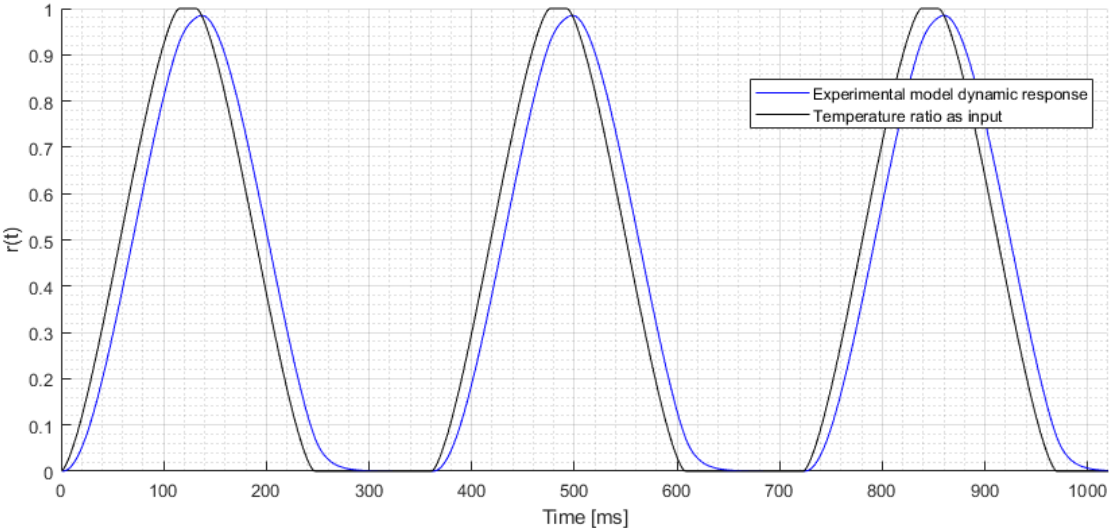


Figure 5.10. Simulation of the system model time response to the surface measured temperature variation for production at normal speed, with pyrometer constant time $T=12.5 \text{ ms}$.

While, in practice, there are some pyrometers in the market that match this response time, there is no option available for the specific wavelength required to measured thin film.

Taking these conclusions into account, a constant error of 5.68% will be considered for the pyrometer response in the experimental results to follow.

Chapter 6

Film Sealing Imaging

As previously mentioned, over the years, computational vision has been gaining more use when it comes to in-line product inspection. With the technological advances, new and improved solutions have appeared in the market for this type of necessity. In this chapter, two different systems for sealed film image collecting will be presented together with two different image classification methods based on texture analysis.

For image classification, four independent steps have to be conducted in the order described in figure 6.1.

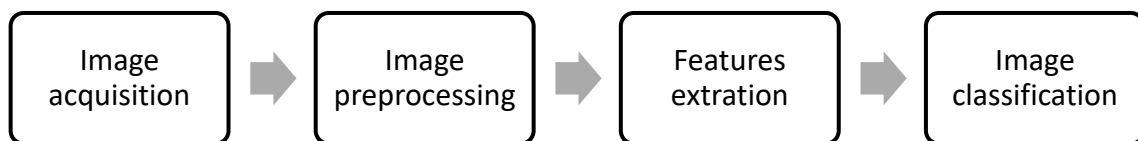


Figure 6.1. Model representing the machine vision steps for image classification.

6.1 Image acquisition

The first step in machine vision is image acquisition. This step is of major importance since it is responsible for the collection of the digital image to be analyzed. The wrong choice of image acquisition tools, such as not appropriate lighting conditions or a low-resolution camera, can make so that the digital image obtained might not contain the necessary object properties needed for its right classification.

The choices for image acquiring setup become even more important when the object to picture possesses properties difficult to record, as is the case BOPP film, which is not only transparent but also highly reflective, which makes the job of qualifying its sealing quality impossible using direct white light.

Taking this into account, in this dissertation, two different types of image acquisition setups will be tested, with tools designed to possibly collect the film characteristics necessary for its right classification.

6.1.1 Infrared imaging

In industrial machine vision, one of the most used types of lighting revolves around infrared radiation. This electromagnetic radiation has a wavelength ranging from approximately 700 nm to 1 mm and is located between the visible and the radio waves in the electromagnetic spectrum. While being generally invisible to the human eye, with particular equipment, IR can be used in innumerable machine vision applications where the specific properties of this lighting bring major advantages [51].

Since electromagnetic light is governed by the equation

$$\lambda = \frac{v}{f} \quad (6.1)$$

with λ being the wavelength, f the wave frequency and v the speed of light, being a longer-wave radiation means that infrared radiation oscillates less frequently than visible radiation, which makes it capable of transmitting further into the sample and, in some cases, transmitting through certain materials such as glass, paper, cloth or plastic. It also enables vision systems to recognize objects and their condition under difficult lighting conditions, where reflective surfaces produce high levels of visible-spectrum noise or the target areas have variable light intensities. Infrared light is also effective at neutralizing contrast differences based on color, primarily because reflection of this light is based more on the sample composition than color differences. Since it is not visible to the human eye, another great advantage is that it can be applied particularly well at workstations where normal light would be disturbing.

As a result of these properties, certain defects or flaws in the sample being inspected which cannot be seen with visible light, can be detected with IR lighting. In most of these applications, where this type of lighting is required, the radiation utilized is located in the near infrared range, which comprises the spectral range from 780 to 3000 nm.

6.1.1.1 Infrared imaging system

Multiple vision systems can be assembled using IR. The components used for the design of the system used for this paper are described in the following subchapters.

6.1.1.2 Lighting

One of the most important parts of an imaging system is the lighting used. For this system, a LED Backlight with 400 x 100 mm is used, covering the full length of the film. It emits near-infrared radiation in a single wavelength: 850nm, with a homogeneity along its length of over 80%. It has anti-reflection coating which reduces reflections of parasite lightning around the system.

This type of lighting is utilized as back lighting, meaning that it illuminates directly the side of the sample for inspection opposite to the camera. This type of configuration is used to greatly increase the contrast of the image obtained. The vision system is also protected by an aluminum cage, blocking outside light from interfering with the system

6.1.1.3 Filtering

To also increase contrast, a collimated filter is used on top of the backlight. Since usually the radiation emitted by backlights has wide and diffuse angles, these filters are used to conduct infrared rays in parallel direction, perpendicular to the object inspected, resulting in a better definition of the object's contours.

6.1.1.4 Image capture

For image capturing, two cameras are used, in parallel, to inspect both straws side by side. These are CMOS area scan monochromatic cameras which have a capability of 38.8 fps, enough to keep up with the production line, and originate high quality images. These cameras are coupled with 16 mm wide-angle lens which have a shorter focal length than standard lens, enabling them to capture a wider angle of view. The cameras are connected to a computer for image collection and processing.

While the cameras maximum capability is 38.8 fps, they do not work autonomously but only when they receive the order to. To know when to take the picture, the system has a photoelectric cell, which is calibrated to the film and straw characteristics. These devices are constituted by a beam of infrared light shining permanently on a light-dependent resistor and producing a steady electric current, which is interrupted every time a straw passes through, sending the signal for the cameras to take a picture.

6.1.1.5 Images collected

Examples of the images obtained can be seen in figure 6.2.

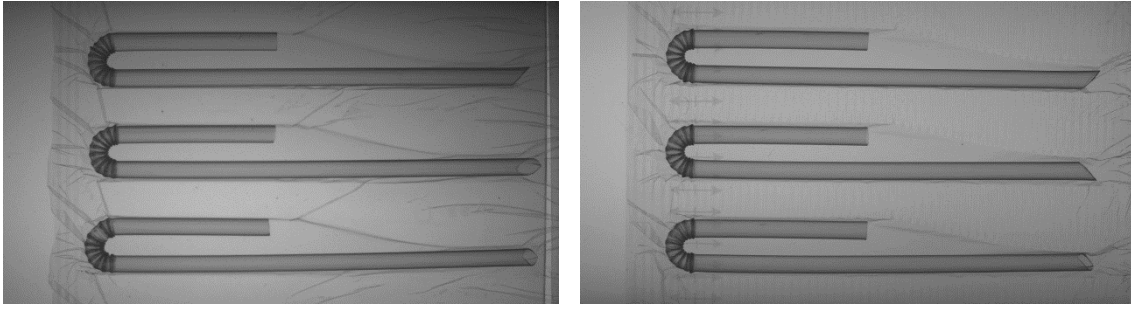


Figure 6.2. On the left: image of clear film sample; on the right: image of rugged film sample.

6.1.2 Polarized filtering imaging

A different vision system solution analyzed in this paper involves the use of polarized filtering. This imaging technique is based on the principle that light is an electromagnetic wave, whose electrical field, magnetic field and propagation direction are orthogonal to one another. Polarization direction is defined as the electrical field direction.

When a polarized filter is used, only the light with an electrical field oscillating perpendicularly to the filter can pass through, blocking light with other polarizations.

This capability of manipulating the polarization state of light that passes through the filter offers numerous benefits in a variety of optical applications, due to the fact that many phenomena in the visible spectrum are polarization sensitive, allowing the detection of physical properties that conventional imaging wouldn't be able to [52].

6.1.2.1 Polarized filtering imaging system

The imaging system used in this paper is composed by different components described in the following sub-chapters. Two configurations of this system were tested, using two different lighting techniques.

6.1.2.2 Lighting

For this system, a white LED monochromatic lighting was used. Two different lighting placements were tested. The first one involved using a backlight configuration, similar to the infrared system, where the sample is placed between the lighting source and the camera. The other configuration involved using diffuse dome light, where the sample is placed in a dome like structure, with the camera inserted in the top of the dome. Models representing these two configurations can be seen in figure 6.3.

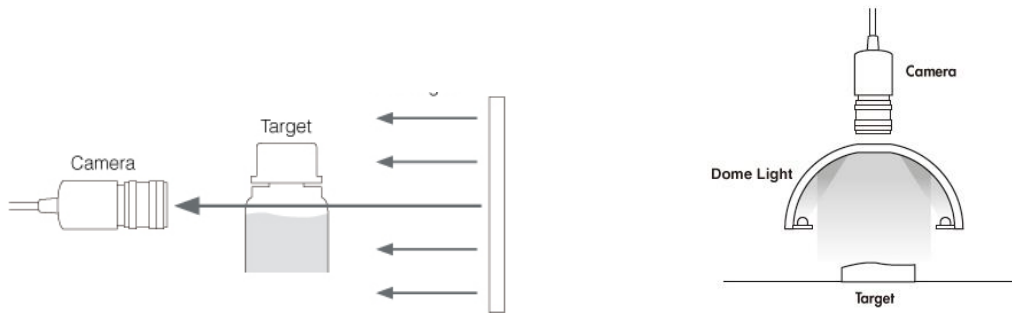


Figure 6.3. On the left: backlight lighting model; on the right: dome light lighting model [53].

6.1.2.3 Filtering

For filtering in this system, a very unique component is used: a quad-polarizer filter. This is a nanowire polarizer filter, incorporated in the camera monochromatic sensor, placed directly on the sensor's pixel array. This brings major advantages when compared to polarizer filters used over the camera, reducing the possibility of light at a polarized angle going into an adjacent pixel and causing wrong readings.

This filter presents a 2x2 pattern, where every pixel has a nanowire polarizer filter with a different angle between 90° , 45° , 135° or 0° , as seen in figure 6.4. This allows the detection of the amount of polarized light passing through each pixel.

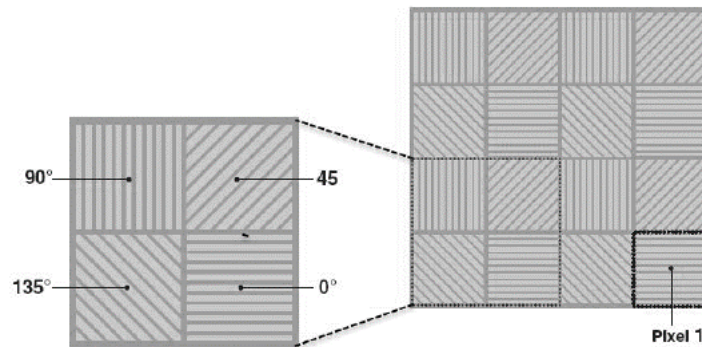


Figure 6.4. Model representing pixel distribution according to the filter polarization angle [54].

6.1.2.4 Image capture

For image capture, a single camera is used. This is a CMOS monochromatic camera with a standard capability of 52 fps, also enough to keep up with the production speed.

6.1.2.5 Images collected

Examples of the images collected can be seen in figures 6.5 and 6.6.

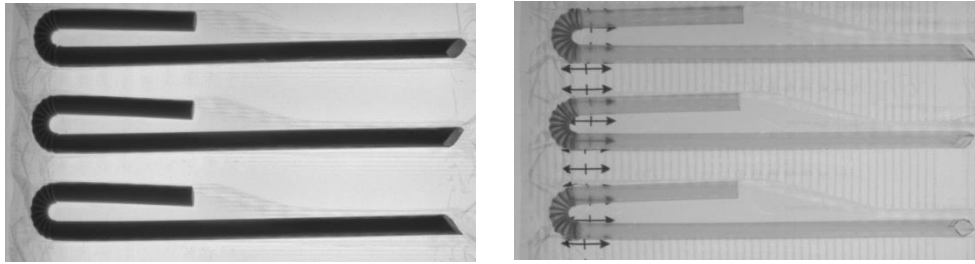


Figure 6.5. Examples of images captured with backlight lighting. On the left: clear film; on the right: rugged film.

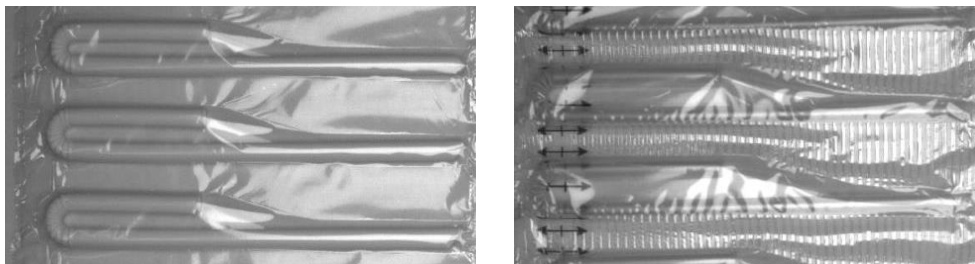


Figure 6.6. Examples of images captured with dome lighting. On the left: clear film; on the right: rugged film.

Taking a look at the images obtained from both types of lighting, it is easy to see that the samples with backlight lighting display a much clearer image. The samples with dome lighting, however, due to the reflective capacity of the film, display an image where light reflection overlaps any possible characteristics of the film. Since the reflected light doesn't actually go through the film, being only reflected by its surface, it is only dependent on the film orientation and not on its properties, making it impossible to extract any conclusion regarding the film sealing quality. Taking this into account, from this point forward only images with backlight lighting will be studied.

6.2 Image preprocessing

The role of the preprocessing step to segment the pattern of interest from the rest of the image acquired [55]. As seen in the figures below, the digital images acquired contain a large area of film with multiple straws. However, for image classification, only a small area of film between the straws, that contains the characteristics related to its sealing quality, is important and necessary.

To isolate these samples of film, an algorithm for image preparation was developed, whose steps can be seen in figure 6.7.

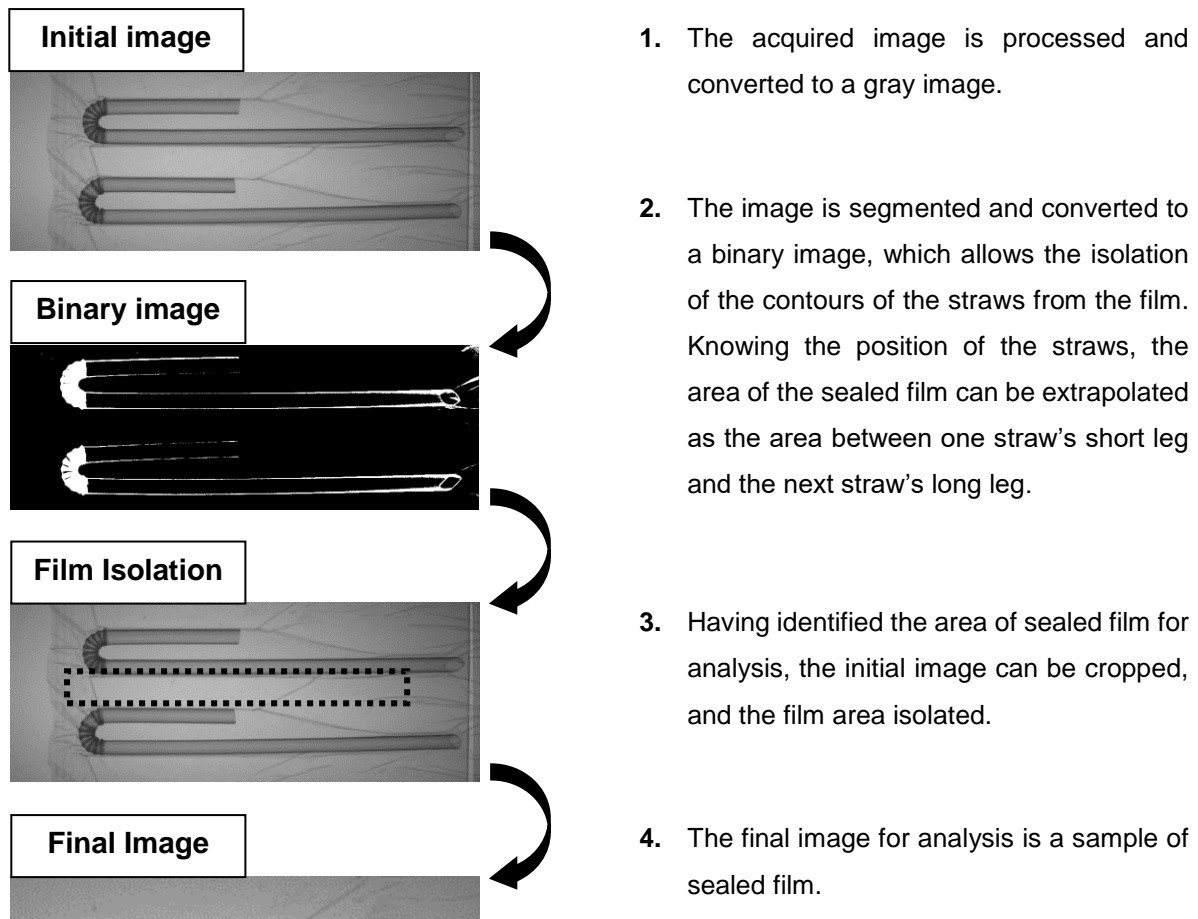


Figure 6.7. Model representing the steps of image preparation.

6.3 Features Extraction

For image classification, it is not necessary to analyze the entire image, but only a set of features that represent the required image characteristics. This compact set of features not only makes the image classification easier but also requires less computational power.

In this dissertation, a specific property of images will be analyzed for feature extraction: texture.

6.3.1 Texture Analysis

In digital images, texture is an important property utilized in many computer vision and image analysis applications. However, in spite of its frequent use and the many attempts to describe it, texture lacks a precise definition [56]. Pietikäinen et al. [57] provides a good description of texture, stating that “A textured area in an image can be characterized by a non-uniform or varying spatial distribution of intensity or color”. Texture can also be seen as a complex visual pattern composed by entities or sub-patterns, characterized by brightness, color, size, etc [58], [59]. The shape of the object and the way it is hit by light, reflections and shadows can change the perception of texture [60].

Texture classification is the process of distinguishing or classifying different images into separate classes, according to its texture properties, being an area of research widely investigated in several computer vision and pattern recognition problems [61].

Finding an efficient texture descriptor is an important step in texture classification. These descriptors extract the texture features of an image, representing them in a more simple and efficient way, allowing for high classification accuracies with low computational time. They can be based on orientations, spatial arrangements of pixels, uniformity, histograms and gradients.

In this dissertation, two different descriptors are described and their application to film sealing quality classification is studied.

6.3.2 Local binary pattern (LBP) descriptor

LBP first emerged in the mid-1990s [61]. It was introduced as a local contrast descriptor [62], and as a development of the texture spectra in [63]. Shortly after, LBP was discovered to be a good texture descriptor [59] and, since then, became one of the most used for this application [56], [64], [65]. Different variations to the classic LBP have since been proposed, with a comprehensive book about the LBP family of texture descriptors being published [57].

The local binary pattern operator is known by its efficiency, maintaining a great accuracy without requiring high computing power, reason why it is one of the most used texture descriptors.

As described by Ojala et al. [59], the LBP pattern allows the representation of a gray level image texture T_{LBP} information by defining the texture in a local neighborhood as the joint distribution of the gray levels of the image pixels. This is described in equations (6.2) e (6.3), where g_c corresponds to the gray value of the center pixel of a local neighborhood and g_p ($p = 0, \dots, P - 1$) correspond to the gray values of P equally spaced pixels on a circle of radius R_{LBP} ($R_{LBP} > 0$), forming a circularly symmetric neighbor set.

$$T_{LBP} = t_{LBP}(g_c, g_0, \dots, g_{P-1}) \approx t_{LBP}(s(g_0 - g_c), \dots, s(g_{P-1} - g_c)) \quad (6.2)$$

$$s(x) = \begin{cases} 0, & x \geq 0 \\ 1, & x < 0 \end{cases} \quad (6.3)$$

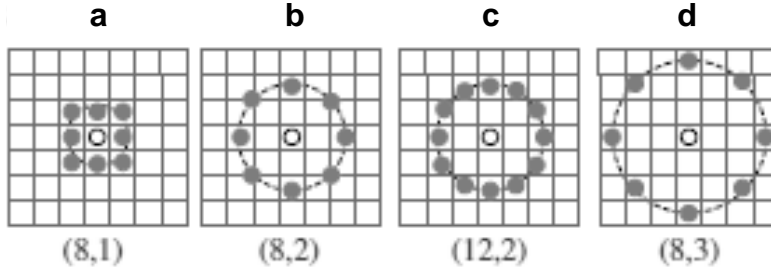


Figure 6.8. Four examples of the LBP described according to (P, R_{LBP}) . The pixel values are interpolated when the sampling point is not in the center of the pixel [64].

This means that, for each pixel in the gray-level image, the central pixel is compared to the neighborhood pixels. The difference between the central pixel and each neighbor is computed and a value of “0” or “1”, according to equation (6.2), is obtained, resulting in a binary number being attributed to each pixel.

As described in [59], a binary factor 2^p is assigned to each neighbor and the original LBP value of each pixel is represented according to equation (6.4), making the conversion from the binary value obtained from equation (6.2) to a integer number.

$$LBP = \sum_{p=0}^{P-1} s(g_p - g_c) \times 2^p \quad (6.4)$$

example	thresholded	weights
6 5 2	1 0 0	1 2 4
7 6 1	1 1 0	128 8
9 8 7	1 1 1	64 32 16

Pattern = **11110001**
LBP = 1 + 16 + 32 + 64 + 128 = 241

Figure 6.9. Example of the calculation of LBP [66].

This means that the LBP descriptor labels the pixels of an image by determining the gray levels of the P neighbors of the center pixel, according to a radius R_{LBP} . Finally, the histogram of the labels is calculated and can be utilized for texture classification.

6.3.2.1 Uniform LBP

A variation of the LBP, focused on the post-processing of the original LBP, is defined as uniform LBP. The difference in this descriptor is that only binary patterns that are considered as uniform are taken into account in the histogram, while all the other non-uniform account only for a single position.

A binary pattern is called uniform if it contains at most two bitwise transitions, with the binary string being considered circular. A formal definition of this classification can be seen in equation (6.5).

$$U_{LBP} = |s(g_{P-1} - g_c) - s(g_0 - g_c)| + \sum_{p=1}^{P-1} s(g_p - g_c) - s(g_{p-1} - g_c) \quad (6.5)$$

Patterns where U_{LBP} has a value of 2 or less are considered uniform. While using this strategy may appear a waste of information regarding the image texture, these uniform patterns contribute over 90% of the spatial patterns present in the images, while sustaining rotation quite well [66].

The resulting feature vector is obtained as a histogram of P+1 elements of uniform patterns and one element of all other patterns summed together. This results in a significant decrease of the feature vector size, while maintaining almost all the texture related information, increasing the image classification performance. The uniform LBP descriptor application to this work will be demonstrated in the following chapters.

6.3.2.2 Multiresolution LBP

Extending the LBP descriptor, it is possible to obtain a multi-resolution descriptor. As described by Ojala et al. [58], multiresolution analysis can be accomplished by combining the information provided by multiple operators of varying radius R_{LBP} and number P of equally spaced pixels in that circle.

Utilizing multiple LBP descriptor vectors for each image increases the amount of information obtained, which can be beneficial when it comes to its classification. Examples of this application can be seen in [67]–[70].

6.3.3 Gray level co-occurrence matrix

One of the most currently used approaches in image processing to describe texture is the statistical approach, widely used due to its good results with a low computational time [71]. This method takes into account the distribution and relationship of the gray levels of the image, using the pixel values and their relationship to the neighbors to create numerical structures that can be associated to the texture pattern present in the image. These numerical structures are defined as gray-level co-occurrence matrices.

Over the years, gray level co-occurrence matrices have been used as a method of texture classification for the most diverse applications, from classification of forest species [65], sea ice patterns mapping [72], rock texture classification [73] or even applied to tissue classification in medical images [71].

To create a GLCM, the initial gray image is first divided into a number of gray levels, where each one represents an equally sized interval of pixel intensity values, from 0 to 255. From this matrix of gray levels, a GLCM is created where the indexes of rows and columns represent the given range of the image gray levels, and the value $F(i, j)$ stored at the position (i, j) is the frequency that gray levels i and j are present, at a given distance and at a given direction. An example of this transformation can be

seen in figure 6.10. After this calculation, the matrix is normalized, dividing each value by the sum of all indexes.

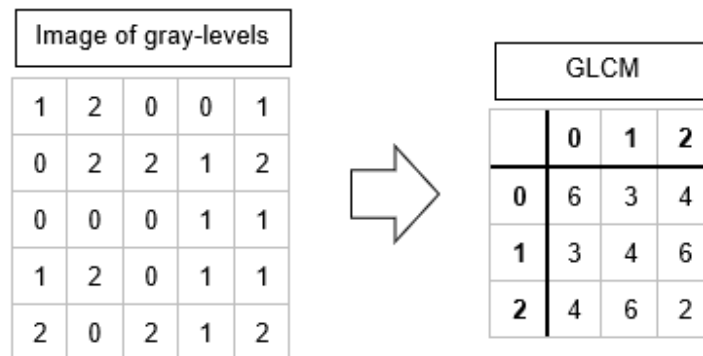


Figure 6.10. On the left: example of an image quantified in 3 gray-levels, sampled in 5x5 pixels; on the right: the correspondent GLCM, for a direction of 0° and a distance of 1. For instance, the value of the GLCM $F(0,1) = 3$ was calculated by scanning the image of gray levels and finding the frequency where, for each pixel with a value of 0, its left or right neighbor pixel value was 1.

Multiple GLCM can be created from a single image by changing the direction and distance parameters. One different GLCM is created for each pair of these parameters, which can relate to different texture properties. The benefits of using multiple GLCM for texture classification will be studied in this paper.

From the GLCM, it is possible to apply different statistical mathematical operations to the matrix values, obtaining different properties of the pixel distribution. These operations can be defined as descriptors, where each one relates to a particular visual feature of the image texture.

From the application of these descriptors, an image signature is obtained, constituted by a set of numerical values, that represents one or more characteristics of it.

In this dissertation, five of the descriptors initially described by Haralick et al. [74] were used to create the image signature.

In the following equations, $F(i, j)$ corresponds to the elements in the normalized GLCM, with i, j being the indexes of the matrix rows and columns. μ_i and μ_j correspond to the mean deviations while σ_i and σ_j are the standards deviations for the rows and columns respectively.

6.3.3.1 Contrast descriptor

Contrast, also known as variance or inertia, returns a measurement of the intensity contrast between the pixels and their neighbors across the entire image.

$$CON = \sum_i \sum_j |i - j|^2 F_{i,j} \quad (6.6)$$

6.3.3.2 Correlation descriptor

The correlation descriptor returns the measurement of the level of correlation between the pixels and their neighbors across the image.

$$COR = \sum_i \sum_j \frac{(i - \mu_i)(j - \mu_j)F_{i,j}}{\sigma_i \sigma_j} \quad (6.7)$$

6.3.3.3 Energy descriptor

Energy, also known as uniformity or angular second momentum, returns the sum of the squared values in the normalized GLCM.

$$ENE = \sum_i \sum_j F_{i,j}^2 \quad (6.8)$$

6.3.3.4 Homogeneity descriptor

Homogeneity returns a value that measures how close the distribution of elements in the normalized GLCM is to its diagonal.

$$HOM = \sum_i \sum_j \frac{F_{i,j}}{1 + |i - j|} \quad (6.9)$$

6.3.3.5 Entropy descriptor

Entropy represents a statistical measurement of randomness of the pixels' intensity across the image.

$$ENT = \sum_i \sum_j F_{i,j} (-\ln F_{i,j}) \quad (6.10)$$

From the descriptor values obtained it is possible to form a vector representing the image signature. This signature can then be used as a parameter for texture classification.

6.3.3.6 Multiple GLCM

When computing the GLCM from an image, multiple parameters are defined that change the matrix obtained. In this dissertation, the variation of the number of gray level intervals, the direction and distance between pixels are analyzed.

A possible solution to increase the amount of textural information obtained from an image revolves around the extraction of multiple GLCM. This can be done by using multiple different direction and distance values, obtaining a different matrix for each pair of values. The descriptors chosen can then be applied to each individual GLCM, obtaining an image signature whose vector size equals to the number of descriptors used multiplied by the number of GLCM extracted. [75], [76].

6.4 Image Classification

In this work, for image classification, a multi-layer perceptron (MLP) neural network is used. This is a class of feed-forward layered networks of artificial neurons, where each neuron computes an activation function on the weighted sum of all its inputs [77].

An MLP consists of one input layer, with as many neurons as the size of the descriptor vector, one output layer, with a number of neurons equal to the number of classes, and a number of hidden intermediate layers. Each node in one layer connects with a certain weight to every node in the following layer.

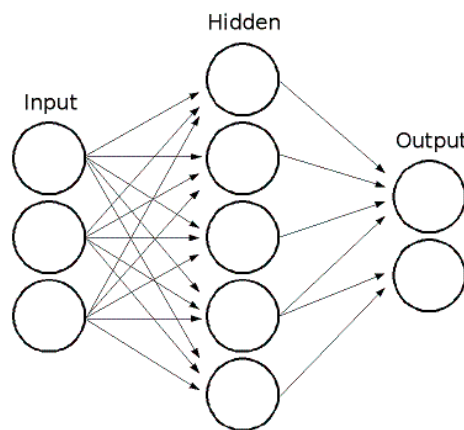


Figure 6.11. MLP diagram [78].

For this thesis, a single hidden layer network was chosen, trained with a scaled conjugate gradient (SCG) backpropagation algorithm [79], known for good performances over a wide variety of problems, while maintaining a fast training time. A percentage of the images collected are used for training, another for validation and a final one for tests.

The network receives a descriptor vector, corresponding to each image, as input and classifies it as good or weak sealing.

6.4.1 Method performance evaluation

In order to evaluate the quality of the method used in image classification, it is necessary to evaluate its performance.

After the image classification algorithm is applied, the images are divided into four groups, according to their predicted classification and their real classification. From this division in four groups, which represent the false positives FP, false negatives FN, true positives TP and true negatives TN, it is possible to create a confusion matrix, also known as an error matrix.

		Actual Class	
		Weak Sealing	Good Sealing
Predicted Class	Weak Sealing	TP	FP
	Good Sealing	FN	TN

Figure 6.12. Model of a confusion matrix, where the classified images are divided into four groups: TP, FP, FN, TN.

From this matrix it is possible to have a clear look at the algorithm performance, as well as calculate diverse performance indicators. One of the most intuitive indicators of a test result is accuracy, which is the percentage of samples predicted right, as seen in equation (6.11).

$$Accuracy = \frac{TP + TN}{TP + TN + FP + FN} \quad (6.11)$$

In this dissertation, a different indicator will also be used to evaluate the network performance: F_1 score. This indicator is equal to the harmonic mean of precision and recall, where precision is the ratio of correctly predicted positive images to the total predicted positive images while recall is the ratio of correctly predicted positive images to all images in the actual class. Due to this, F_1 score takes both false positives and false negatives into account, reaching its maximum value at 1.

$$Precision = \frac{TP}{TP + FP} \quad (6.12)$$

$$Recall = \frac{TP}{TP + FN} \quad (6.13)$$

$$F_1 \text{ score} = 2 \times \frac{\text{Recall} \times \text{Precision}}{\text{Recall} + \text{Precision}} \quad (6.14)$$

Chapter 7

Imaging Experimental Results

In this chapter the results for the application of machine vision image classification will be analyzed.

The images were collected from good sealing samples, classified as good, and weak sealing and really weak sealing samples, classified as bad. These images can be divided into four groups, according to table 7.1.

		Nº of samples	Number of Good sealing to Weak sealing images ratio
Clear film	Infrared imaging	710	4:1
	Polarized filtering imaging	272	1:1
Rugged film	Infrared imaging	1300	4:1
	Polarized filtering imaging	248	1:1

Table 7.1. Table representing the division of images collected for each category.

For image classification, as previously described, an MLP neural network is used. As initial parameters, it has a hidden layer size of 10 neurons and the samples, after being randomly organized, are divided into train, validation and test groups according to the ratios, respectively, of 70%, 15% and 15%. These conditions are maintained across all tests to establish a line of comparison between the different algorithms.

In order to guarantee the best results, for each test, 200 neural networks were trained, and the best performing one, with the highest F_1 score, was picked. To also guarantee that the best results obtained weren't a consequence of overfitting, neural networks where the difference between the test accuracy and the train accuracy was higher than 3% were excluded.

7.1 Local binary pattern descriptor results

In order to estimate the best result for LBP, two parameters were varied according to the best performances obtained. These are the number of equally spaced neighborhood pixels and the radius, which is the distance in pixels between the central and the neighborhood pixels.

For each group of images, the radius was varied from 1 to 20 pixels, while the number of neighborhood pixels changed from 4 to 32, in multiples of 4. In figures 7.1 and 7.2 it is possible to analyze the average F_1 score for each radius value and number of pixels respectively. Table 7.2 presents the best performances obtained for each group.

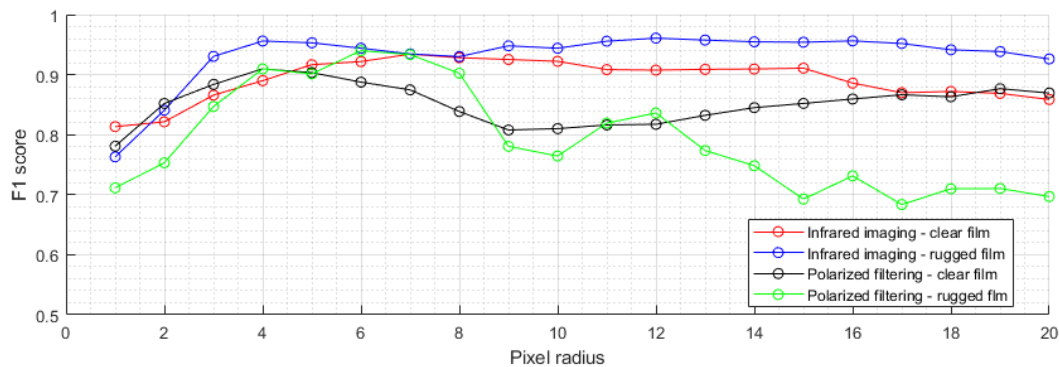


Figure 7.1. Average F1 score for different levels of pixel radius.

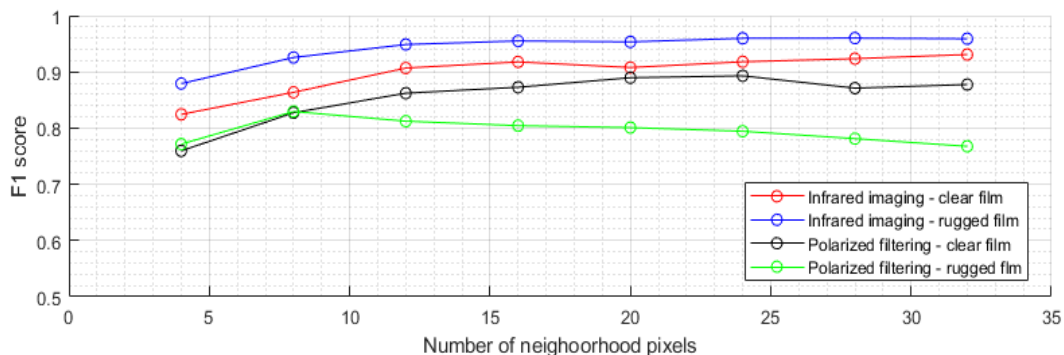


Figure 7.2. Average F1 score for different number of neighborhood pixels.

		Radius	Number of pixels	F_1 score
Clear film	Infrared imaging	9 pixels	28 pixels	0.978
	Polarized filtering imaging	4 pixels	24 pixels	0.951
Rugged film	Infrared imaging	12 pixels	24 pixels	0.990
	Polarized filtering imaging	6 pixels	16 pixels	0.984

Table 7.2. Best F_1 scores for variation of radius and number of pixels.

The best performances for a single LBP were obtained. However, it is still possible to combine this LBP with another with a different radius and number of pixels. Tests were conducted where these two parameters were changed, and the best results obtained can be seen in table 7.3.

		LBP 1		LBP 2		F ₁ score
		Radius	Number of pixels	Radius	Number of pixels	
Clear film	Infrared imaging	9 pixels	28 pixels	13 pixels	4 pixels	0.996
	Polarized filtering imaging	4 pixels	24 pixels	5 pixels	24 pixels	0.967
Rugged film	Infrared imaging	12 pixels	24 pixels	19 pixels	28 pixels	0.994
	Polarized filtering imaging	6 pixels	16 pixels	8 pixels	4 pixels	0.996

Table 7.3. Performance results for multiple LBP.

While the performances obtained from a single LBP were already high, it is still possible to verify a small increase in the F₁ score obtained with the use of multiple LBP.

To evaluate if the choice for the number of neurons in the hidden layer of the neural network was correct, a test was conducted to analyze its impact in the performance obtained, whose results can be seen in figure 7.3. Overall, the increase of the number of artificial neurons leads to a small decrease in performance.

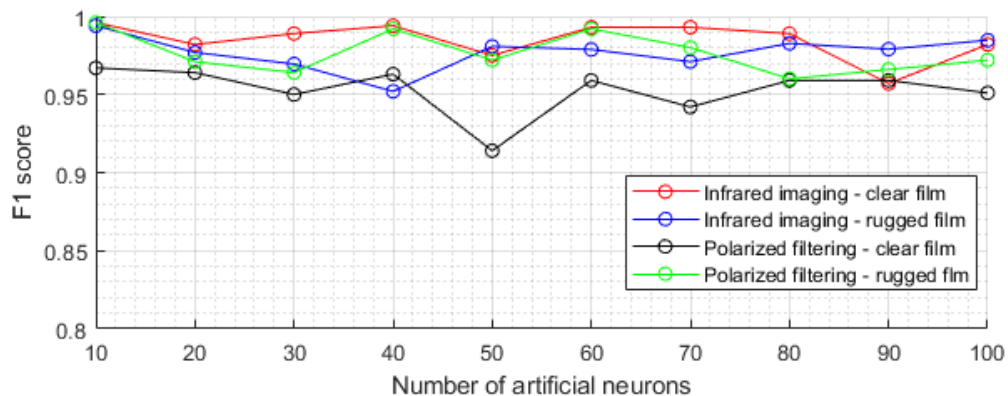


Figure 7.3. LBP performance variation related with the number of artificial neurons.

7.2 Gray level co-occurrence matrix results

In order to estimate the best result for GLCM, four different parameters were varied according to the best performances. These parameters are the number of gray levels the image is divided, the direction angle and distance between pixels when computing the GLCM and the descriptors, from contrast, correlation, energy, homogeneity and entropy, used for feature extraction.

The first parameter to analyze is the number of gray levels, where it is possible to observe from figure 7.3 that the ideal value is 32 levels, for both types of film and acquisition system. For the next tests, a number of 32 gray-levels will be considered.

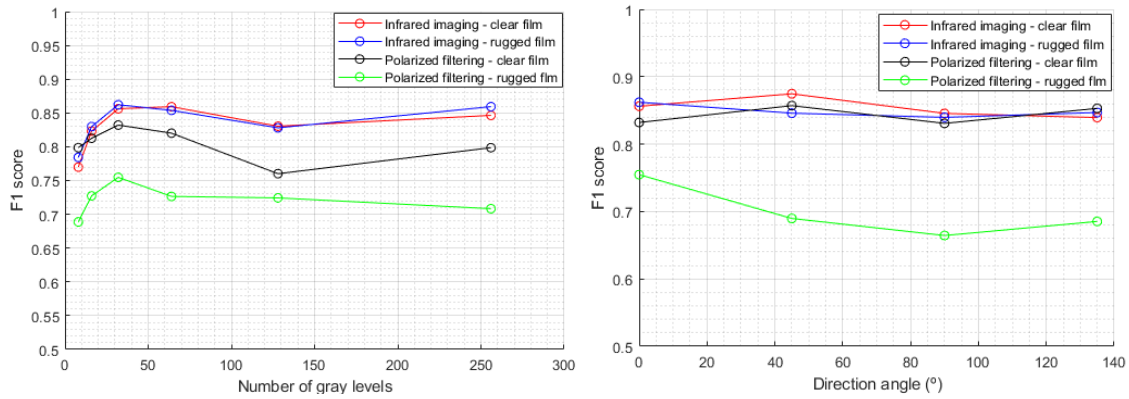


Figure 7.4. On the left: variation of the number of gray-levels; on the right: variation of the direction angle.

It is also possible to observe from the same figure, on the right, the performance variation according to the direction angle, where, for the rugged film, a horizontal direction of 0° is more beneficial, while the clear film benefits from a direction angle of 45°.

Fixing this direction angles, it is possible to estimate the distance between pixels that results in the best performance. The results can be seen in table 7.4. It is possible to see that the distance between pixels has a major impact in the performance of the algorithm applied to the rugged film images.

		Direction Angle	Distance	F ₁ score
Clear film	Infrared imaging	45°	15 pixels	0.913
	Polarized filtering imaging	45°	12 pixels	0.864
Rugged film	Infrared imaging	0°	14 pixels	0.906
	Polarized filtering imaging	0°	8 pixels	0.947

Table 7.4. Distance in pixels that results in the best performance.

In figure 7.5 it is possible to compare the F₁ scores obtained when removing one descriptor. For polarized filtering, there is a substantial performance drop when the entropy and homogeneity descriptors are removed for the clear and rugged film respectively. For infrared imaging, the clear film performance is more dependent on the contrast, while the rugged film splits its dependency with the homogeneity and energy descriptors. Overall, all groups benefit from the use of all five descriptors, achieving the highest classification performance with all five.

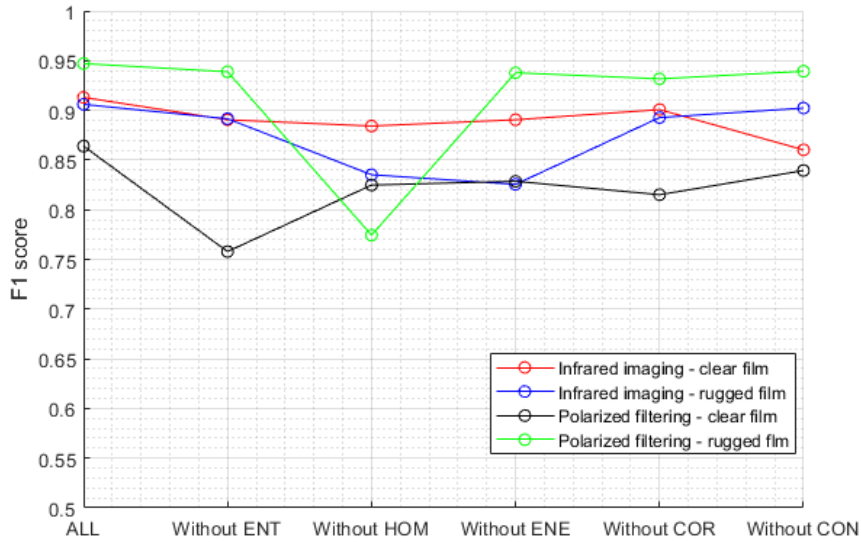


Figure 7.5. Performance variation related with descriptors variation.

Having obtained the highest performance values for a single GLCM, tests were conducted to evaluate the benefits of combining this GLCM with another with different distance and direction angle as parameters. The best results obtained can be seen in table 7.5. It is possible to see a significant increase in performance for all categories with the use of the more robust multiple GLCM.

		GLCM 1		GLCM 2		F ₁ score
		Direction angle	Distance	Direction angle	Distance	
Clear film	Infrared imaging	45°	15 pixels	0°	6 pixels	0.943
	Polarized filtering imaging	45°	12 pixels	0°	17 pixels	0.916
Rugged film	Infrared imaging	0°	14 pixels	90°	17 pixels	0.990
	Polarized filtering imaging	0°	8 pixels	45°	4 pixels	0.984

Table 7.5. Performance results for multiple GLCM.

Similar to before, to evaluate the impact of the number of neurons in the hidden layer of the neural network in the model performance, a test was conducted, whose results can be seen in figure 7.6. It can be easily seen that the increase of the number of artificial neurons leads to a decrease in performance, which is a result of the network overfitting.

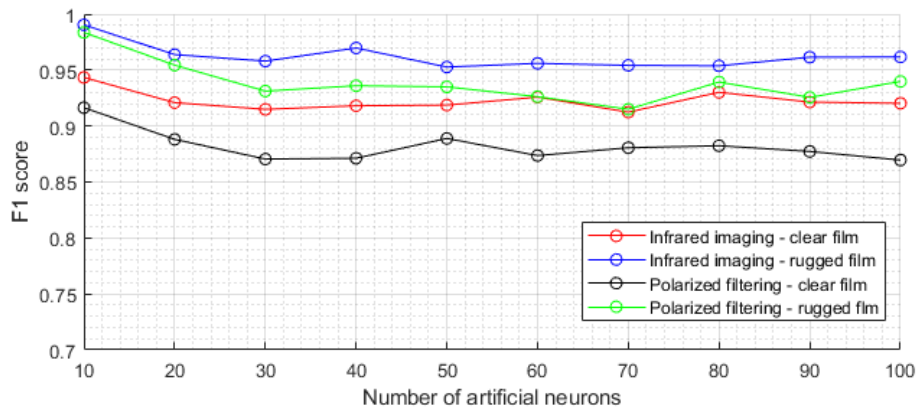


Figure 7.6. GLCM performance variation related with the number of artificial neurons.

For a more detailed view, all the tests performance values can be seen in appendix C.

7.3 Results comparison

In table 7.6 it is possible to see the best F1 scores obtained with each texture descriptor for all four groups of images.

F ₁ score		LBP	GLCM
Clear film	Infrared imaging	0.996	0.943
	Polarized filtering imaging	0.967	0.916
Rugged film	Infrared imaging	0.994	0.990
	Polarized filtering imaging	0.996	0.984

Table 7.6. Comparison between the best F1 score obtained from both texture descriptors.

Despite the great performances achieved with the GLCM, the local binary pattern takes the win for all four groups of images.

Comparing both image acquisition systems, when it comes to the clear film, the infrared imaging is clearly the best option. For the rugged film, however, the polarized filtering imaging presents a small edge. It is important to mention, however, that for the rugged film the number of images from polarized filtering used was much lower.

Having achieved an F₁ score of 0.996 for both types of films means, in practical terms, that the algorithm predicts the image classification with an accuracy of 99.5%, or that 1 in 200 images will be predicted wrong. While this seems like an optimal result, in a practical application in an industrial setting at high production speeds, 1 in 200 wrong predictions has a major impact.

For an application in industrial environment, there is another parameter that needs to be taken into account, which is the algorithm's computational time. In table 7.7 it is possible to see the computational times for the different algorithms, which include all the steps from image preparation, features extraction and classification.

		Computational time [s]	
		mean	σ
LBP	Single	0.616	0.094
	Multiple	0.939	0.152
GLCM	Single	0.289	0.024
	Multiple	0.343	0.018

Table 7.7. Computational times for the different algorithms.

Overall, it is possible to see that the GLCM descriptor is significantly faster than the LBP, with a computational time 53% lower if we compare the single algorithms, or an even higher 63% time reduction for the multiple descriptors. Despite having a worse performance, in cases where low computational speed is essential, the GLCM presents a great advantage.

Chapter 8

Pyrometer Experimental Results

To analyze the real response of the pyrometer in the industrial environment, the sensor was installed in two different machines, for each type of film, in the straw factory.

8.1 Installation

The sensor was placed right after the sealing process, normal to the film, at 10mm, and directed to the left side which, as previously defined, corresponds to the critical area with the lowest temperature. To keep the sensor in the right position throughout the tests, a metal support was designed and installed, whose technical drawing, together with the installation specifications, can be seen in appendix B.

The sensor was connected to a laptop through USB and experimental data was collected continuously. This data included the time, temperature value measured by the sensor and the room temperatures at the sensor and at the sensor's box placed outside the machine. New values were obtained every millisecond.

8.2 Experiment in normal production conditions

With the machine working with normal production conditions, with a sealing temperature of 130 °C and pressure of 0,45 MPa, the sensor response data was collected.

As previously deduced, the temperature values measured change as the sealed and unsealed areas pass through the sensor, obtaining an oscillatory response as seen in figure 8.1.

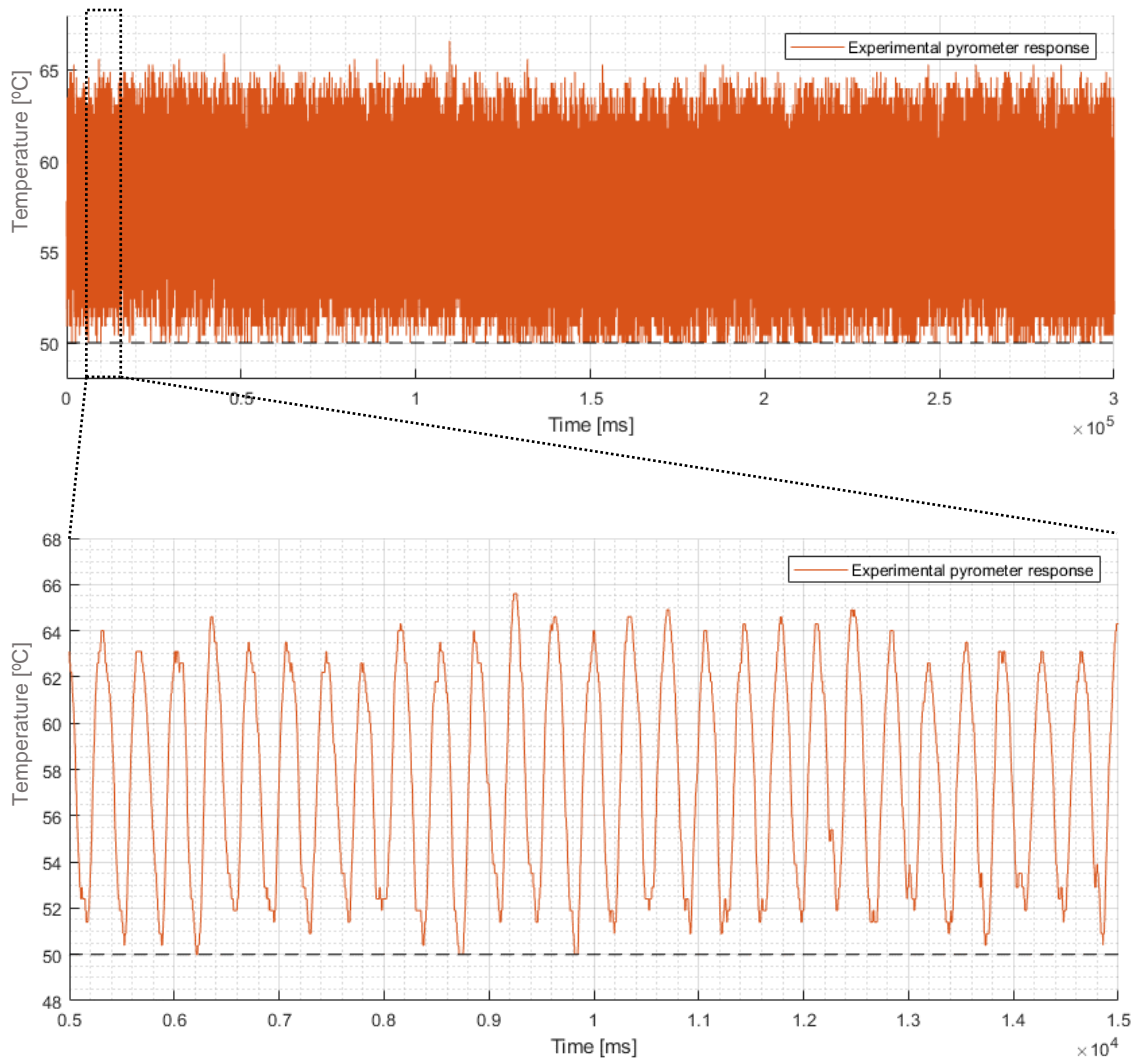


Figure 8.1. Sample of 5 minutes of experimental pyrometer response in normal production conditions, with a zoom of 10 seconds.

Analyzing the multiple sets of data collected from the sensor response to the machine working in normal conditions, the following temperature values were obtained, which can be seen in table 8.1 and figure 8.2. The peak film temperature T_p corresponds to the highest temperature value measured for each straw iteration, which relates to the sealed film temperature. On the other hand, the valley film temperature T_v corresponds to the lowest temperature value measured for each straw iteration, which relates to the non-sealed film temperature. To obtain the vector of values that correspond to the peaks, the Matlab function *findpeaks*, present in the Signal processing Toolbox, was used [83]. To obtain the vector of values that correspond to the bottom temperature, the same function was applied, but to the inverse of the data values.

	mean	σ	σ^2
Peak film temperature T_p [$^{\circ}\text{C}$]	63.44	0.90	0.81
Valley film temperature T_v [$^{\circ}\text{C}$]	50.43	0.63	0.40

Table 8.1. Average values and standard deviation of the peak and valley film temperature

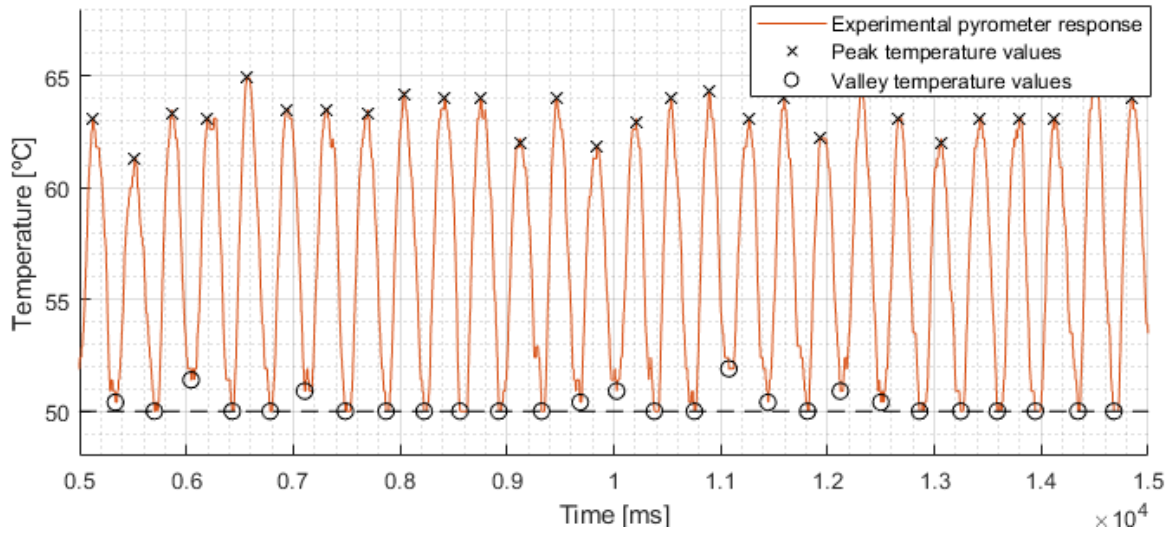


Figure 8.2. Representation of the peak and valley temperature values in each iteration.

8.2.1 Theoretical model validation

Assuming the peak and valley film average temperatures, described in table 8.1, it is possible to estimate the model, described in chapter 5, and compare it to the experimental data obtained. Figure 8.3 shows a sample of 10 seconds of this comparison, while in table 8.2 we can see the statistical results of the error for both cases.

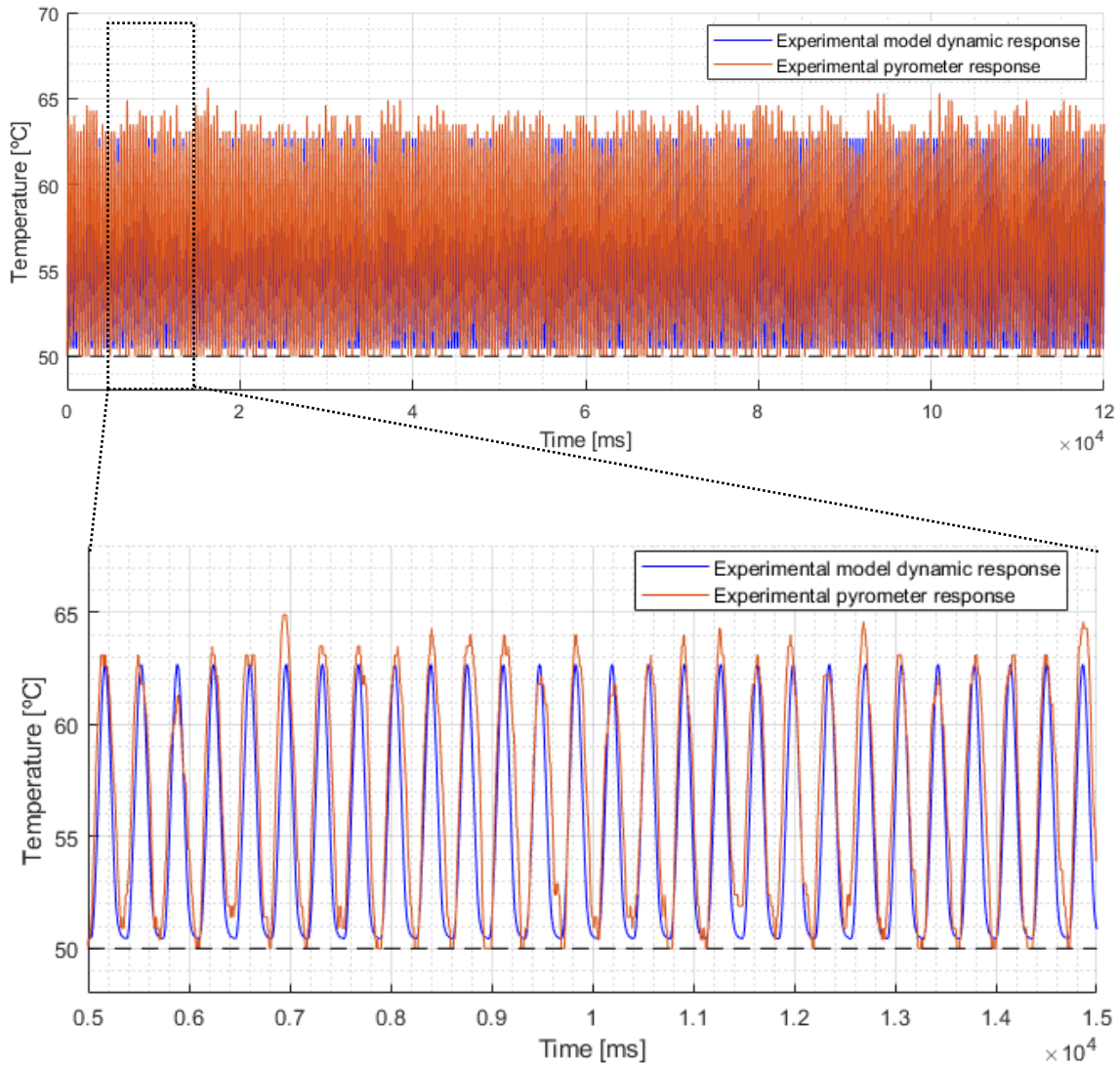


Figure 8.3. Sample of 2 minutes of experimental pyrometer response, in normal production conditions, in comparison to the model response, with a zoom of 10 seconds.

	Max Error	mean	σ	σ^2
Clear film [°C]	2.66	1.66	2.64	6.97
Rugged film [°C]	3.02	1.89	2.95	8.70

Table 8.2. Statistical results of the error between the theoretical model and the experimental pyrometer response

Despite the theoretical model proposed being a simplified representation of the film temperature variation, it is possible to observe that the experimental data obtained shows a very similar behavior to the model. The error obtained is mostly related to the pyrometer measurement accuracy, described by the manufacturer as $\pm 3^\circ\text{C}$ [84]. It is also a result of the film oscillation as it leaves the machine.

8.2.2 Peak temperature analysis – Moving average filter

In order to correlate the pyrometer temperature measured with the seal quality of the film, the only temperature values necessary to analyze are the ones related to the film sealed surface, which correspond to the peak temperature values in each iteration. However, these peak temperature values can fluctuate, as previously mentioned.

To contradict this fluctuation, a moving average filter can be applied to the data values related to temperature peaks. This is one of the most common filters used in digital signal processing, being optimal for reducing random data fluctuations while retaining a sharp step response [85]. This filter operates by averaging a number of points, from the input signal, to estimate each point in the output signal. Its written form can be seen in equation (8.1), where $x_{MA}[i]$ represents the input signal, $y_{MA}[i]$ is the output signal, and M is the number of points averaged.

$$y_{MA}[i] = \frac{1}{M} \sum_{j=0}^{M-1} x_{MA}[i + j] \quad (8.1)$$

For this application, however, it is required to consider only past values from the input signal, assuming the filter a different form, seen in equation (8.2).

$$y_{MA}[i] = \frac{1}{M} \sum_{j=-M+1}^0 x_{MA}[i + j] \quad (8.2)$$

The parameter to take into account when applying this filter is the number of points to average M . If used just a small number of points, the temperature fluctuations might not be smoothed. However, a high number of values averaged might result in a loss of information, eliminating the detection of temperature fluctuations related to sealing conditions, or increasing the time for their detection.

In table 8.3, it is possible to see the results of using a moving average filter to reduce the max temperature error. These results were obtained from data collected over 2 hours of production in normal working conditions.

	Max Error	Max Error with MA filter $M=3$	Max Error with MA filter $M=6$	Max Error with MA filter $M=9$
Clear film [°C]	2.66	1.96	1.73	1.51
Rugged film [°C]	3.02	2.15	1.94	1.67

Table 8.3. Comparison of the maximum temperature errors obtained with and without the moving average filter as a comparison with the theoretical model. M corresponds to the number of points averaged.

By using a filter averaging the last 9 points, which corresponds to a sample time of only 3.25 seconds, it is possible to reduce the maximum error in 43.2% and 44.7%, for clear and rugged film respectively. As such, using this filter allows the elimination of noisy temperature fluctuations while maintaining a quick detection of variations in the sealing process.

8.3 Experiment with abnormal production conditions

As previously mentioned, and confirmed, weak sealing can be related to lack of temperature or pressure in the sealing creation process. To observe the pyrometer response to failures in the sealing process and correlate the sensor measurements to the film sealing conditions, two sets of tests were conducted, related to variations in the sealing temperature and pressure.

8.3.1 Experimental results with sealing temperature variation

In order to observe the pyrometer response to sealing temperature variation, two types of tests were conducted. In the first type, with the machine always working, the temperature controller value was slowly dropped allowing the observation of the pyrometer response in real time. In figure 8.4, it is possible to see the comparison between the sealing temperature values, shown in the controller, and the film sealed surface temperature values, obtained from the pyrometer response peak values passed through a moving average filter with $M=9$ past input values.

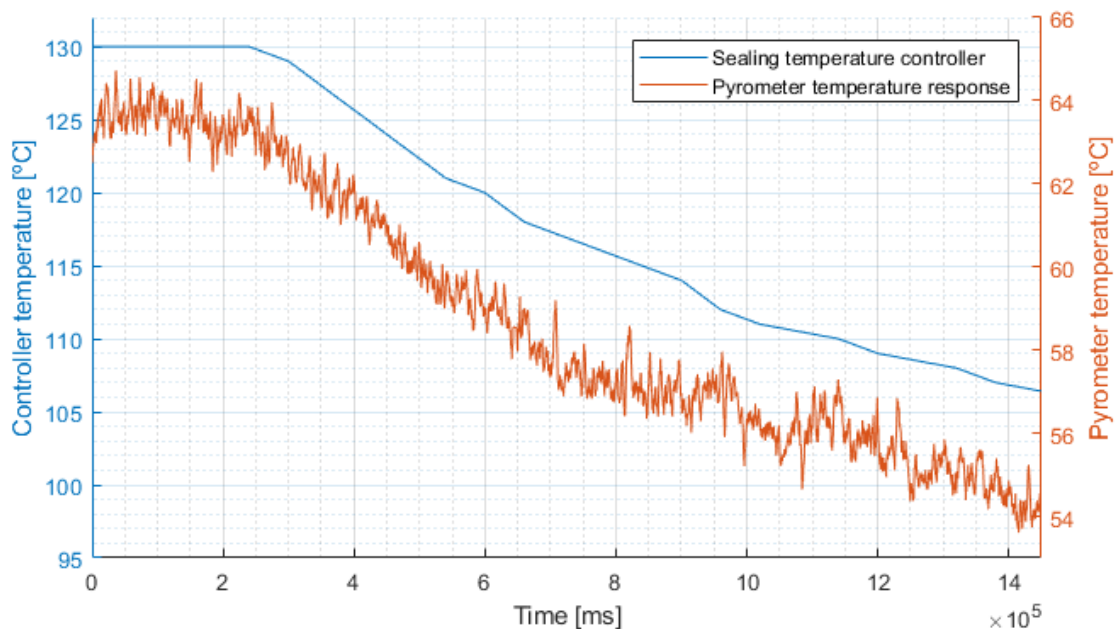


Figure 8.4. Comparison between the controller temperature and pyrometer temperature variation, for rugged film.

From figure 8.4, it is possible to conclude that, as expected, there is a clear relation between the temperature inside the sealing cylinder, shown in the controller, and the film temperature after

sealing, measured by the pyrometer. Approximately, for every degree Celsius the temperature controller drops, the pyrometer measurement drops 0.41°C.

It is also possible to observe that the pyrometer temperature starts to drop approximately 90 seconds before the controller. This happens due to the fact that the temperature displayed in the controller is measured by a thermocouple inside the sealing cylinder, but, after the signal to drop the temperature is sent, the first area to lose temperature is the cylinder surface, due to heat transfer to the environment, which has a direct impact on the sealing conditions before it is even measured by the thermocouple.

Another point to mention is that, as the temperature drops, the pyrometer measurements become more erratic. What happens is that the two layers of film in the sealing area start to separate, creating an uneven surface, which directly impact the pyrometer measurements.

The second type of tests were conducted with a fixed controller temperature value, to study the pyrometer response in these conditions. The temperature values chosen are some of the values used to obtain the sealing samples for the tests described in chapter 3, each one representing each different quality of sealing. The machine was started with the controller at the defined temperature, after a period of approximately 10 minutes for temperature stabilization in the sealing cylinder. A summary of the data collected can be seen in table 8.4.

Type of film	Controller temperature [°C]	Quality of sealing	Pyrometer temperature (with MA filter $M=9$) [°C]		
			mean	σ	max deviation
Clear film (at 0.5 MPa)	115	Good sealing	67.21	0.41	1.46
	105	Weak sealing	63.82	0.43	1.71
	100	Really Weak Sealing	59.76	0.76	2.11
Rugged film (at 0.5 MPa)	130	Good sealing	63.44	0.53	1.94
	120	Weak sealing	58.74	0.62	1.79
	115	Really Weak Sealing	56.32	0.98	2.43

Table 8.4. Pyrometer response at different sealing temperatures for both types of film.

Analyzing the results, it can be identified that the measured temperature for the rugged film is lower, as expected. This happens due to the fact that, not only is the rugged film thinner, not requiring as much heat to reach the sealing temperature, but also presents stripes of film that are not directly sealed, due to the morphology of the sealing cylinder used, as previously described in chapter 2.

It is also possible to confirm a clear difference between acceptable and not acceptable sealing temperature measurements in both films, which confirms the pyrometer capability to make the distinction required.

8.3.2 Experimental results with sealing pressure variation

The same tests just described in the previous subchapter were also conducted with sealing pressure variation. In the first set of tests, the production started with good sealing conditions, and the sealing pressure was dropped in intervals of 0.05 MPa to a low value. This variation and the pyrometer response to it can be seen in figure 8.5.

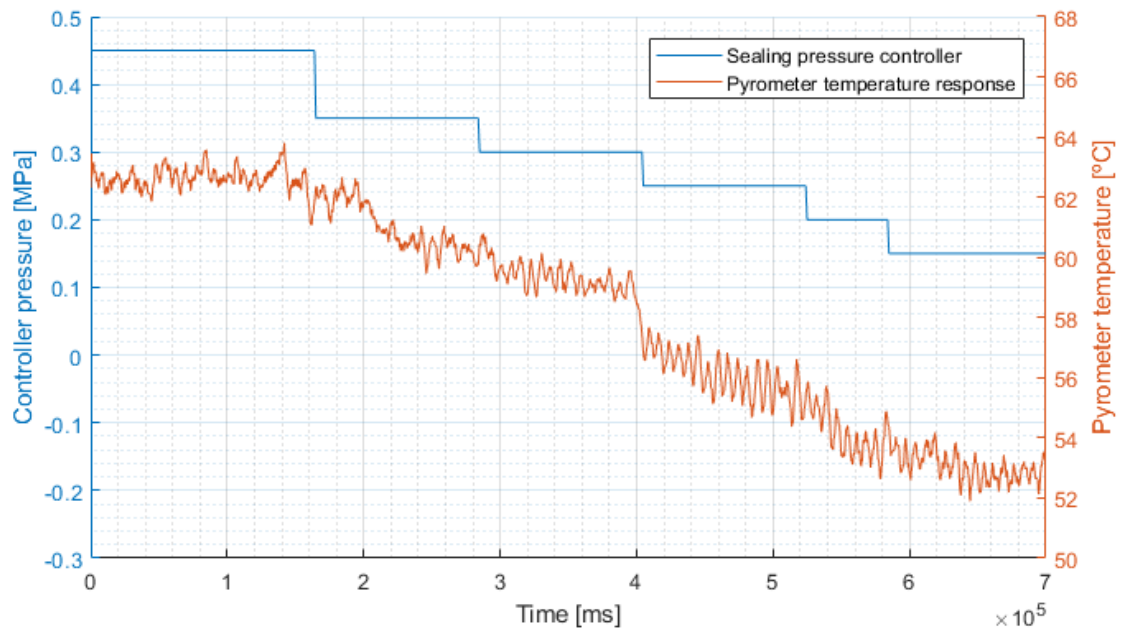


Figure 8.5. Comparison between the controller pressure and pyrometer temperature variation, for rugged film.

Observing figure 8.5, it is possible to establish a clear relation between the sealing pressure and the film surface temperature measured by the pyrometer. It is also possible to confirm that at 0,3 MPa there is a clear drop in the measured temperature, which corresponds to a drastic reduction of seal strength, like it was shown in chapter 3, leading also to a more erratic pyrometer measurement.

The second set of tests were conducted with a fixed sealing pressure, to study the pyrometer response in these conditions. The pressure values chosen are also the same used to obtain the sealing samples for the peel tests, each one representing a different seal quality. Since the pressure variation is almost immediate, there was no need for a set-up period for the machine in these conditions. A summary of the data collected can be seen in table 8.5.

Type of film	Controller pressure [MPa]	Quality of sealing	Pyrometer temperature (with MA filter $M=9$) [°C]		
			mean	σ	max deviation
Clear film (at 115 °C)	0.50	Good sealing	67.21	0.41	1.68
	0.30	Weak sealing	63.50	0.53	1.74
	0.25	Really Weak Sealing	58.85	1.22	2.89
Rugged film (at 130 °C)	0.50	Good sealing	63.44	0.53	1.96
	0.30	Weak sealing	59.03	0.74	2.07
	0.25	Really Weak Sealing	55.81	1.16	2.71

Table 8.5. Pyrometer response at different sealing pressure for both types of film.

Just like the temperature variation, it is also possible to confirm a clear difference between acceptable and not acceptable sealing temperature measurements in both films.

With these tests it is proven the capability of using the measurement of the sealed film surface temperature, for both types of films, with a pyrometer sensor, as a way of evaluating the film sealing strength.

Chapter 9

Conclusions

9.1 Achievements

This work proposes two distinct systems for inspection of BOPP film sealing quality in straw packaging. The main goal is to have an in-line system capable of inspecting all the products produced and detecting possible sealing defects produced, for two different types of film, while being viable to be implemented in an industrial environment.

First, an analysis of the heat-sealing process and parameters was presented. Sealed film samples for different production parameter values were produced and subjected to a peel test for measurement of their seal strength. The critical area of the film was identified, and the samples were classified according to their sealing quality.

A hypothesis was presented relating the seal quality with the temperature of the film after sealing. Different temperature measurement methods were presented, concluding that a non-contact method specific for the characteristics of the film was required. A pyrometer device specific for thin plastic film was analyzed.

Theoretical and experimental models for the pyrometer were presented, together with the estimation of the model for film temperature variation. The pyrometer model response to the film temperature variation was analyzed and it was concluded that the pyrometer response time was not fast enough to follow the temperature variations, assuming a small constant error.

The pyrometer was then tested in a real application, validating the theoretical film temperature variation model presented. A moving average filter was introduced for data processing. The experimental results obtained with the pyrometer in abnormal production showed that the film temperature measured is directly related with the change in the production parameters that govern the sealing process, proving the hypothesis that it can be related with sealing quality. It is also clearly possible to make a distinction between the different sealing quality classifications according to the temperature measured, for both types of film, proving the capability of this system in inspecting BOPP film sealing quality.

A solution for sealing quality inspection based on machine vision was also presented. Two different imaging systems, one based on infrared lighting and the other on polarized filtering, were used

to collect images from the samples obtained for different production conditions. Two textural descriptors were proposed for image features extraction, based on the local binary pattern and the gray level co-occurrence matrix and for classification, a multi-layer perceptron neural network was used.

Good results were obtained, with F_1 scores very close to one for both types of film. showing the good capability of the textural descriptors in extracting from the images the necessary information related to its sealing properties. Comparing the two descriptors performances, the local binary pattern achieves a higher performance for all the systems. Comparing both image acquisition systems, when it comes to the clear film, the infrared imaging is clearly the best option. For the rugged film, however, the polarized filtering imaging presents a small edge. Comparing, however, the computational times, the GLCM descriptor is much faster than the LBP.

Overall, with this work it was possible to achieve the main objective of identifying a system for in-line inspection of BOPP film sealing quality in straw packaging.

9.2 Future Work

Despite the developed work achieving the primary objective defined, some work could still be done to improve the systems. The implementation and validation of the systems in the factory environment over a significant period of time would be important to truly evaluate their performance.

With the fast advances in technology and the growing need for industry automation in quality control, new and improved solutions can be developed over the following years.

A route to explore would be the application of a thermographic camera specific for thin PP film, since an area analysis of the sealed film surface in real time would bring major advantages when compared to the point temperature measurement of pyrometers, allowing us to pinpoint the defect area and more easily identify the root cause of the problem.

Another area to explore would be to test different image acquisition systems, with new and improved cameras being constantly developed. Different classification algorithms could also prove to be more effective, especially with the constant new developments in artificial intelligence capabilities for image recognition and classification.

References

- [1] B. Morris, *The science and technology of flexible packaging: multilayer films from resin and process to end use*. Boston, MA: Elsevier, 2016.
- [2] S. Ebnesajjad, *Plastic films in food packaging materials, technology and applications*. Amsterdam: Elsevier, William Andrew, 2013.
- [3] S. E. M. Selke and J. D. Culter, *Plastics packaging: properties, processing, applications, and regulations*, 3rd edition. Munich : Hanser Publishers ; Cincinnati: Hanser Publications, 2016.
- [4] G. L. Robertson, *Food packaging: principles and practice*, 3rd ed. Boca Raton, FL: CRC Press, 2013.
- [5] K. Yamada, K. Miyata, R. Konishi, K. Okada, and T. Tsujii, "Molecular Orientation Effect of Heat-Sealed PP Film on Peel Strength and Structure," *Adv. Mater. Phys. Chem.*, vol. 05, no. 11, pp. 439–446, 2015.
- [6] J. F. Hanlon, R. J. Kelsey, and H. E. Forcinio, *Handbook of package engineering*, 3rd ed. Lancaster, Pa: Technomic Pub. Co, 1998.
- [7] K. L. Yam, Ed., *The Wiley encyclopedia of packaging technology*, 3rd ed. Hoboken, N.J: John Wiley & Sons, 2009.
- [8] N. Theobald and B. Winder, *Packaging closures and sealing systems*. Oxford; Boca Raton, FL: Blackwell Pub. ; CRC Press, 2006.
- [9] "ASTM F2054 / F2054M-13, Standard Test Method for Burst Testing of Flexible Package Seals Using Internal Air Pressurization Within Restraining Plates, ASTM International, West Conshohocken, PA, 2013, www.astm.org."
- [10] C. L. Harper, B. A. Blakistone, J. Bruce Litchfield, and S. A. Morris, "Developments in food packaging integrity testing," *Trends Food Sci. Technol.*, vol. 6, no. 10, pp. 336–340, Oct. 1995.
- [11] "ASTM F88 / F88M-15, Standard Test Method for Seal Strength of Flexible Barrier Materials, ASTM International, West Conshohocken, PA, 2015, www.astm.org."
- [12] M. Dudbridge, *Handbook of seal integrity in the food industry*. Oxford, UK ; Hoboken, NJ: Wiley Blackwell, 2016.
- [13] "ASTM F2338-09(2013), Standard Test Method for Nondestructive Detection of Leaks in Packages by Vacuum Decay Method, ASTM International, West Conshohocken, PA, 2013, www.astm.org."
- [14] "ASTM F2391-05(2016), Standard Test Method for Measuring Package and Seal Integrity Using Helium as the Tracer Gas, ASTM International, West Conshohocken, PA, 2016, www.astm.org."

- [15] M. A. Pascall, J. Richtsmeier, J. Riemer, and B. Farahbakhsh, "Non-destructive packaging seal strength analysis and leak detection using ultrasonic imaging," *Packag. Technol. Sci.*, vol. 15, no. 6, pp. 275–285, Nov. 2002.
- [16] B. Ostyn, P. Darius, J. De Baerdemaeker, and B. De Ketelaere, "Statistical Monitoring of a Sealing Process by Means of Multivariate Accelerometer Data," *Qual. Eng.*, vol. 19, no. 4, pp. 299–310, Oct. 2007.
- [17] Y. S. Song, M. Gera, B. Jain, and J. L. Koontz, "Evaluation of a Non-destructive High-voltage Technique for the Detection of Pinhole Leaks in Flexible and Semi-rigid Packages for Foods: High-voltage leak detection for food packages," *Packag. Technol. Sci.*, vol. 27, no. 6, pp. 423–436, Jun. 2014.
- [18] Z. Shuangyang, "Fast Inspection of Food Packing Seals Using Machine Vision," in *2010 International Conference on Digital Manufacturing & Automation*, Changcha, TBD, China, 2010, pp. 724–726.
- [19] M. Barnes, M. Dudbridge, and T. Duckett, "Polarised light stress analysis and laser scatter imaging for non-contact inspection of heat seals in food trays," *J. Food Eng.*, vol. 112, no. 3, pp. 183–190, Oct. 2012.
- [20] M. Vollmer and K.-P. Möllmann, *Infrared thermal imaging: fundamentals, research and applications*, Second edition. Weinheim, Germany: Wiley-VCH Verlag GmbH & Co. KGaA, 2018.
- [21] K. D'huys, W. Saeys, and B. De Ketelaere, "Active Infrared Thermography for Seal Contamination Detection in Heat-Sealed Food Packaging," *J. Imaging*, vol. 2, no. 4, p. 33, Nov. 2016.
- [22] T. L. Bergman, A. Lavine, and F. P. Incropera, *Fundamentals of heat and mass transfer*. 2017.
- [23] B. Davidson, C. Gonyea, J. Cardwell, and M. Cantwell, "Heat Sealing Fundamentals, Testing, and Numerical Modeling." Worcester Polytechnic Institute, Apr-2015.
- [24] C. S. Yuan and A. Hassan, "Effect of bar sealing parameters on OPP/MCPP heat seal strength," *Express Polym. Lett.*, vol. 1, no. 11, pp. 773–779, 2007.
- [25] P. Meka and F. C. Stehling, "Heat sealing of semicrystalline polymer films. I. Calculation and measurement of interfacial temperatures: Effect of process variables on seal properties," *J. Appl. Polym. Sci.*, vol. 51, no. 1, pp. 89–103, Jan. 1994.
- [26] F. C. Stehling and P. Meka, "Heat sealing of semicrystalline polymer films. II. Effect of melting distribution on heat-sealing behavior of polyolefins," *J. Appl. Polym. Sci.*, vol. 51, no. 1, pp. 105–119, Jan. 1994.
- [27] H. W. Theller, "Heat sealability of Flexible Web Materials in Hot-Bar Sealing Applications," *J. Plast. Film Sheeting*, vol. 5, no. 1, pp. 66–93, Jan. 1989.
- [28] B. A. Morris, "Predicting the Heat Seal Performance of Ionomer Films," *J. Plast. Film Sheeting*, vol. 18, no. 3, pp. 157–167, Jul. 2002.
- [29] Y. Hashimoto, U. S. Ishiaku, Y. W. Leong, H. Hamada, and T. Tsujii, "Effect of heat-sealing temperature on the failure criteria of oriented polypropylene/cast polypropylene heat seal," *Polym. Eng. Sci.*, vol. 46, no. 2, pp. 205–214, Feb. 2006.

- [30] T. Tetsuya, Y. Hashimoto, U. S. Ishiaku, M. Mizoguchi, Y. W. Leong, and H. Hamada, "Effect of heat-sealing temperature on the properties of OPP/OPP heat seals. Part II. Crystallinity and thermomechanical properties," *J. Appl. Polym. Sci.*, vol. 99, no. 2, pp. 513–519, Jan. 2006.
- [31] B. A. Blakistone, Ed., *Principles and applications of modified atmosphere packaging of foods*, 2nd ed. London: Blackie Academic & Professional, 1998.
- [32] T. Tetsuya, U. S. Ishiaku, M. Mizoguchi, and H. Hamada, "The effect of heat sealing temperature on the properties of OPP/OPP heat seal. I. Mechanical properties," *J. Appl. Polym. Sci.*, vol. 97, no. 3, pp. 753–760, Aug. 2005.
- [33] K. Hishinuma and H. Miyagawa, *Heat sealing technology and engineering for packaging: principles and applications*. Lancaster, Pa: DEStech Publ, 2009.
- [34] S. Farris, C. A. Cozzolino, L. Introzzi, and L. Piergiovanni, "Effects of different sealing conditions on the seal strength of polypropylene films coated with a bio-based thin layer," *Packag. Technol. Sci.*, vol. 22, no. 6, pp. 359–369, Oct. 2009.
- [35] D. Aithani, H. Lockhart, R. Auras, and K. Tanprasert, "Heat Sealing measurement by an innovative technique," *Packag. Technol. Sci.*, vol. 19, no. 5, pp. 245–257, Sep. 2006.
- [36] "DIN, ENISO. '11607-1. Packaging for terminally sterilized medical devices–Part 1: Requirements for materials, sterile barrier systems and packaging systems, DIN EN ISO 11607-2.' Packaging for terminally sterilized medical devices–Part 2: 16-23." .
- [37] C. S. Yuan, A. Hassan, M. I. Ghazali, and A. F. Ismail, "Heat-seal strength analysis of laminated films with LLDPE and LDPE sealant materials in bar sealing application," *FEIIC Semin. Eng. Technol.*, p. 8, 2006.
- [38] B. A. Morris, "Predicting the heat seal performance of ionomer films.," *J. Plast. Film Sheeting* 183, pp. 157–167, 2002.
- [39] V. M. Hernandez-Izquierdo and J. M. Krochta, "Thermal transitions and heat-sealing of glycerol-plasticized whey protein films," *Packag. Technol. Sci.*, vol. 22, no. 5, pp. 255–260, Aug. 2009.
- [40] W. Bernal, "Relating Burst Pressure to Seal Peel Strength In Pouches," *Clemson Univ.*, p. 142, 2012.
- [41] "Datasheets Maxim Integrated 2019, accessed 1 May 2019, <www.datasheets.maximintegrated.com/en/ds/DS18B20.pdf>." .
- [42] D. P. DeWitt and G. D. Nutter, Eds., *Theory and practice of radiation thermometry*. New York: Wiley, 1988.
- [43] X. P. V. Maldague, *Nondestructive Evaluation of Materials by Infrared Thermography*. London: Springer London, 1993.
- [44] C. Maier and T. Calafut, *Polypropylene: the definitive user's guide and databook*. Norwich, NY: Plastics Design Library, 1998.
- [45] "Optris Global 2019, accessed 1 May 2019, <www.optris.global/optris-xi-400>." .
- [46] "Optris Global 2019, accessed 1 May 2019, <www.optris.global/optris-ct-p3>." .

- [47] A. Bendada and M. Lamontagne, "A new infrared pyrometer for polymer temperature measurement during extrusion moulding," *Infrared Phys. Technol.*, vol. 46, no. 1–2, pp. 11–15, Dec. 2004.
- [48] N. P. Cheremisinoff, Ed., *Handbook of engineering polymeric materials*. New York: Marcel Dekker, 1997.
- [49] I. I. Taubkin, M. A. Trishenkov, and N. V. Vasilchenko, "Minimum temperature difference detected by the thermal radiation of objects," *Infrared Phys. Technol.*, vol. 35, no. 5, pp. 715–732, Aug. 1994.
- [50] T. Fu, J. Liu, J. Tang, M. Duan, H. Zhao, and C. Shi, "Temperature measurements of high-temperature semi-transparent infrared material using multi-wavelength pyrometry," *Infrared Phys. Technol.*, vol. 66, pp. 49–55, Sep. 2014.
- [51] D.-W. Sun, *Computer vision technology in the food and beverage industries*. Woodhead Publishing Limited, 2012.
- [52] Y. Zhao and A. Alù, "Manipulating light polarization with ultrathin plasmonic metasurfaces," *Phys. Rev. B*, vol. 84, no. 20, Nov. 2011.
- [53] "Keyence 2019, accessed 1 May 2019, <www.keyence.com>." .
- [54] "Teledyne 2019, accessed 1 May 2019, <www.teledynedalsa.com>." .
- [55] A. K. Jain, P. W. Duin, and Jianchang Mao, "Statistical pattern recognition: a review," *IEEE Trans. Pattern Anal. Mach. Intell.*, vol. 22, no. 1, pp. 4–37, Jan. 2000.
- [56] G. Kylberg and I.-M. Sintorn, "Evaluation of noise robustness for local binary pattern descriptors in texture classification," *EURASIP J. Image Video Process.*, vol. 2013, no. 1, Dec. 2013.
- [57] M. Pietikäinen, A. Hadid, G. Zhao, T. Ahonen, *Computer Vision Using Local Binary Patterns, vol. 40 of Computational Imaging and Vision*. London: Springer, 2011.
- [58] T. Ojala, M. Pietikainen, and T. Maenpaa, "Multiresolution gray-scale and rotation invariant texture classification with local binary patterns," *IEEE Trans. Pattern Anal. Mach. Intell.*, vol. 24, no. 7, pp. 971–987, Jul. 2002.
- [59] T. Ojala and M. Pietikainen, "A comparative study of texture measures with classification based on feature distributions," *Pattern Recognit.* 291, pp. 51–59, 1996.
- [60] U. R. Babu, V. V. Kumar, and B. Sujatha, "Texture Classification Based on Texton Features," *Int. J. Image Graph. Signal Process.*, vol. 4, no. 8, pp. 36–42, Aug. 2012.
- [61] P. Cavalin and L. S. Oliveira, "A Review of Texture Classification Methods and Databases," in *2017 30th SIBGRAPI Conference on Graphics, Patterns and Images Tutorials (SIBGRAPI-T)*, Niterói, 2017, pp. 1–8.
- [62] D. Harwood, T. Ojala, M. Pietikäinen, S. Kelman, and L. Davis, "Texture classification by center-symmetric auto-correlation, using Kullback discrimination of distributions," *Pattern Recognit. Lett.*, vol. 16, no. 1, pp. 1–10, Jan. 1995.
- [63] L. Wang and D.-C. He, "Texture classification using texture spectrum," *Pattern Recognit.*, vol. 23, no. 8, pp. 905–910, Jan. 1990.

- [64] X. Qian, X.-S. Hua, P. Chen, and L. Ke, "PLBP: An effective local binary patterns texture descriptor with pyramid representation," *Pattern Recognit.*, vol. 44, no. 10–11, pp. 2502–2515, Oct. 2011.
- [65] J. Martins, L. S. Oliveira, S. Nisgoski, and R. Sabourin, "A database for automatic classification of forest species," *Mach. Vis. Appl.*, vol. 24, no. 3, pp. 567–578, Apr. 2013.
- [66] M. Topi, O. Timo, P. Matti, and S. Maricor, "Robust texture classification by subsets of local binary patterns," in *Proceedings 15th International Conference on Pattern Recognition. ICPR-2000*, Barcelona, Spain, 2000, vol. 3, pp. 935–938.
- [67] R. Davarzani, K. Yaghmaie, S. Mozaffari, and M. Tapak, "Copy-move forgery detection using multiresolution local binary patterns," *Forensic Sci. Int.*, vol. 231, no. 1–3, pp. 61–72, Sep. 2013.
- [68] H.-C. Lian and B.-L. Lu, "Multi-view gender classification using multi-resolution local binary patterns and support vector machines," *Int. J. Neural Syst.*, vol. 17, no. 06, pp. 479–487, Dec. 2007.
- [69] T. Mäenpää and M. Pietikäinen, "Multi-scale Binary Patterns for Texture Analysis," in *Image Analysis*, vol. 2749, J. Bigun and T. Gustavsson, Eds. Berlin, Heidelberg: Springer Berlin Heidelberg, 2003, pp. 885–892.
- [70] S. Kundu, N. Das, and M. Nasipuri, "Automatic Detection of Ringworm using Local Binary Pattern (LBP)," *ArXiv Prepr. ArXiv11030120*, p. 6, 2011.
- [71] J. C. Felipe, A. J. M. Traina, and C. Traina, "Retrieval by content of medical images using texture for tissue identification," in *16th IEEE Symposium Computer-Based Medical Systems, 2003. Proceedings.*, New York, NY, USA, 2003, pp. 175–180.
- [72] L.-K. Soh and C. Tsatsoulis, "Texture analysis of SAR sea ice imagery using gray level co-occurrence matrices," *IEEE Trans. Geosci. Remote Sens.*, vol. 37, no. 2, pp. 780–795, Mar. 1999.
- [73] M. Partio, B. Cramariuc, M. Gabbouj, and A. Visa, "Rock Texture Retrieval Using Gray Level Co-Occurrence Matrix," *Proc 5th Nord. Signal Process. Symp.*, vol. 75, 2002.
- [74] R. M. Haralick, K. Shanmugam, and I. Dinstein, "Textural Features for Image Classification," *IEEE Trans. Syst. Man Cybern.*, vol. SMC-3, no. 6, pp. 610–621, Nov. 1973.
- [75] P. Cavalin, L. S. Oliveira, A. L. Koerich, and A. S. Britto, "Wood Defect Detection using Grayscale Images and an Optimized Feature Set," in *IECON 2006 - 32nd Annual Conference on IEEE Industrial Electronics*, Paris, France, 2006, pp. 3408–3412.
- [76] P. R. Cavalin, M. N. Kapp, J. Martins, and L. E. S. Oliveira, "A multiple feature vector framework for forest species recognition," in *Proceedings of the 28th Annual ACM Symposium on Applied Computing - SAC '13*, Coimbra, Portugal, 2013, p. 16.
- [77] M. Sonka, V. Hlavac, and R. Boyle, *Image processing, analysis, and machine vision*, 3. ed. Stamford, Conn.: Cengage Learning, 2008.
- [78] E. R. Davies, *Computer and machine vision: theory, algorithms, practicalities*, 4th ed. Amsterdam ; Boston: Elsevier, 2012.
- [79] M. F. Møller, "A scaled conjugate gradient algorithm for fast supervised learning," *Neural Netw.*, vol. 6, no. 4, pp. 525–533, Jan. 1993.

- [80] J. F. Peters, *Foundations of Computer Vision*, vol. 124. Cham: Springer International Publishing, 2017.
- [81] *Geometric algebra applications*. New York, NY: Springer Berlin Heidelberg, 2018.
- [82] A. Majumder and M. Gopi, *Introduction to Visual Computing: Core Concepts in Computer Vision, Graphics, and Image Processing*. CRC Press, 2018.
- [83] "Signal Processing Toolbox™ Reference." The MathWorks, Inc., 2018-1988.
- [84] Optris, "Optris CTP3 Technical Data, accessed in 1 May 2019, <www.optris.com/optris-ctp3?file=tl_files/pdf/Downloads/Compact%20series%20US/datasheet-optris-ct-p3.pdf>." .
- [85] S. W. Smith, *The scientist and engineer's guide to digital signal processing*. San Diego, Calif.: California Technical Pub., 1999.

Appendix A

Peel Test Method

In this appendix it will be described the peel test, mentioned in chapter 3, used to analyze the seal strength of the film.

The peel test used follows the ISO 11607-1:2019 norm [36], which includes the ASTM F88 procedure [11], which is the standard test method for analysis of the seal strength of flexible barrier materials. This test method covers the measurement of the strength of seals in flexible barrier materials, measuring the force required to separate a test strip of material containing the seal while also identifying the mode of specimen failure. This standard does not purport to address all of the safety concerns, if any, associated with its use. It is the responsibility of the user of this standard to consult and establish appropriate safety and health practices and determine the applicability of regulatory imitations prior to use [11].

A.1 Sample preparation

The material being tested corresponds to the seal of two oriented polypropylene layers of film. The test specimens were prepared by cutting the film according the dimensions shown in figure A.1, perpendicular to the direction of seal. They were subjected to a minimum conditioning time of 40 h, in order to guarantee seal stability was reached.

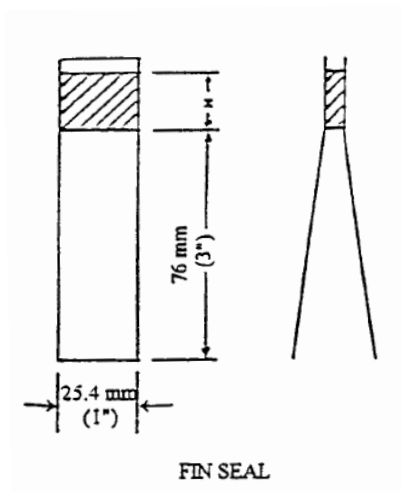


Figure A.1. On the left: diagram representing the sample dimensions; on the right: sample of film collected.

A.2 Test Procedure

The peel tests were conducted in an *Instron* tensile testing machine, connected to *Instron Bluehill* software, in a laboratory.

For the test, each leg of the specimen was clamped in the testing machine, in an unsupported hold, as described in figure A.2, with enough slack so the seal is not stressed prior to the initiation of the test. The sealed area was placed approximately equidistant between the grips and was aligned perpendicular to the direction of pull. The tests were made with a rate of grip separation of 8mm/min.

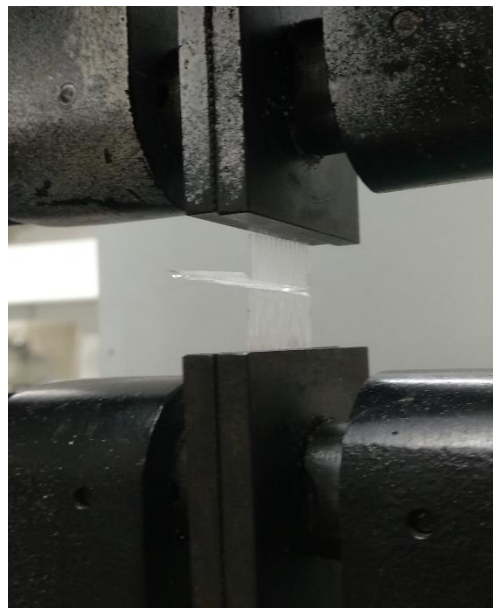
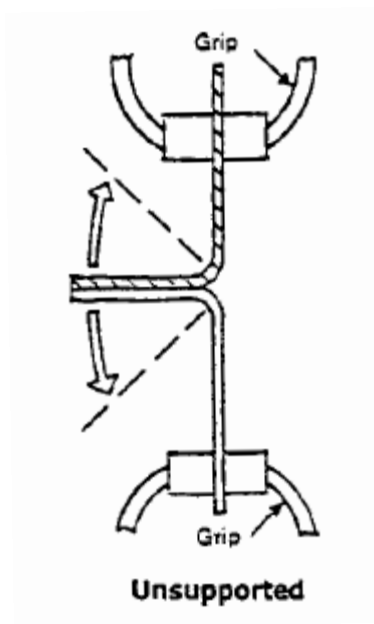


Figure A.2. On the left: a diagram representing the unsupported hold; on the right: a picture showing the specimen hold.

A.3 Results Analysis

For each test conducted, data from the load applied in comparison to the extension of the specimen would be collected. From this data it was possible to evaluate the seal strength profile, as seen in figure A.3.

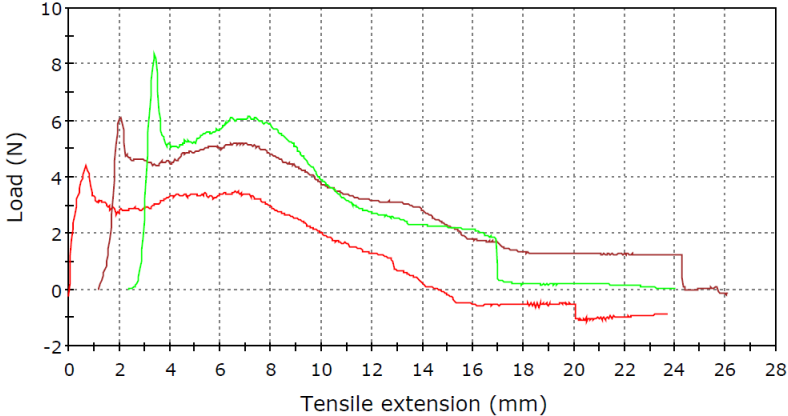


Figure A.3. Example of 3 different seal strength profiles.

It was also possible to evaluate the test samples failure modes. Three different failure modes were identified, as seen in figure A.4.

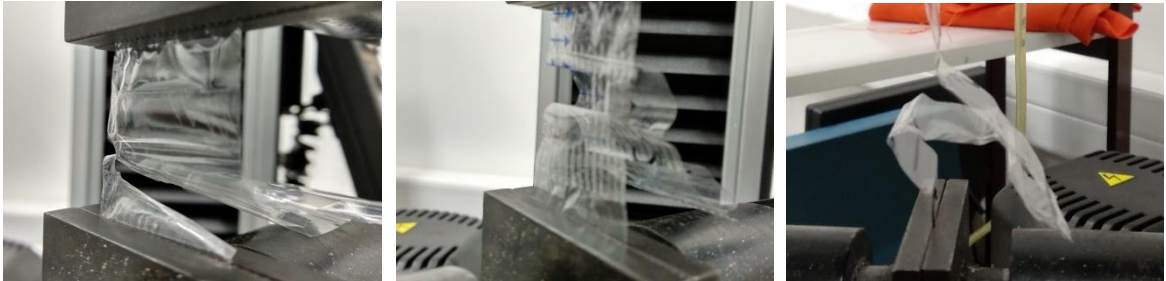


Figure A.4. On the left: seal break; on the middle: seal tear; on the right: seal peel.

Due to the poor resolution of the tensile test machine used, which was not specific for this type of problem, the values might not be as exact as expected. Despite this, it was possible to obtain a rough estimate of the force required to separate the test specimens.

Appendix B

Pyrometer Installation

As previously mentioned, the pyrometer sensor was placed right after the sealing process, normal to the film, at 10mm, and directed to the left side. To not only attach the sensor to the machine structure, but also tightly secure it in place, maintaining the pretended conditions through all the tests, a metal support was designed and developed. The 3D model, designed in Solidworks, and the final product can be seen, respectively, in figures B.1 and B.2.

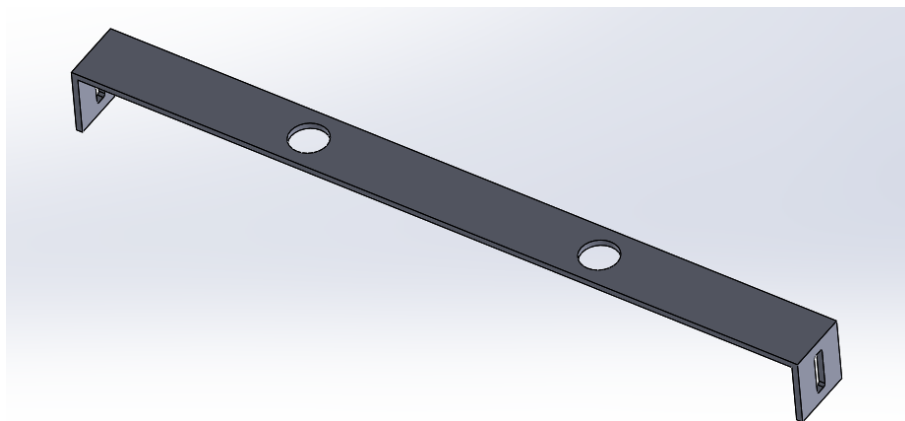


Figure B.1. Pyrometer support 3D model.



Figure B.2. Picture of pyrometer support.



Figure B.3. Pyrometer installation in the machine.

Appendix C

Imaging Result Values

C.1 Local binary pattern results

Initial Parameters:

Radius in pixels = 1

Number of neighborhood pixels = 8

Number of neurons in hidden layer = 10

C.1.1 Clear film

Infrared imaging

		Radius									
		1	2	3	4	5	6	7	8	9	10
Number of neighborhood pixels	4	0.787	0.816	0.806	0.844	0.836	0.817	0.803	0.786	0.776	0.812
	8	0.840	0.804	0.849	0.870	0.828	0.871	0.897	0.859	0.873	0.875
	12	-	0.822	0.875	0.890	0.914	0.925	0.948	0.936	0.929	0.895
	16	-	0.843	0.880	0.912	0.939	0.964	0.953	0.971	0.942	0.925
	20	-	-	0.893	0.911	0.953	0.953	0.978	0.968	0.968	0.975
	24	-	-	0.892	0.883	0.950	0.950	0.968	0.956	0.964	0.968
	28	-	-	-	0.897	0.950	0.961	0.964	0.975	0.978	0.964
	32	-	-	-	0.913	0.964	0.935	0.962	0.975	0.971	0.964
		Radius									
		11	12	13	14	15	16	17	18	19	20
Number of neighborhood pixels	4	0.835	0.815	0.844	0.839	0.877	0.863	0.835	0.852	0.832	0.813
	8	0.853	0.864	0.855	0.873	0.917	0.904	0.823	0.905	0.904	0.810
	12	0.916	0.893	0.899	0.930	0.930	0.892	0.897	0.891	0.937	0.912
	16	0.879	0.935	0.910	0.906	0.886	0.890	0.909	0.885	0.953	0.954
	20	0.929	0.975	0.920	0.872	0.901	0.842	0.809	0.909	0.764	0.822
	24	0.956	0.918	0.923	0.968	0.945	0.879	0.891	0.831	0.838	0.845
	28	0.949	0.952	0.967	0.946	0.904	0.889	0.919	0.819	0.817	0.849
	32	0.950	0.908	0.954	0.942	0.926	0.929	0.876	0.885	0.906	0.865

Table C.1. F₁ score obtained from clear film classification with infrared imaging with variation of the radius together with the number of neighborhood pixels.

Polarized filtering imaging

		Radius									
		1	2	3	4	5	6	7	8	9	10
Number of neighborhood pixels	4	0.709	0.764	0.795	0.788	0.806	0.832	0.806	0.818	0.725	0.738
	8	0.853	0.871	0.872	0.885	0.867	0.848	0.842	0.815	0.762	0.672
	12	-	0.882	0.886	0.899	0.928	0.888	0.874	0.819	0.798	0.839
	16	-	0.892	0.918	0.947	0.927	0.895	0.888	0.833	0.842	0.862
	20	-	-	0.913	0.944	0.920	0.881	0.908	0.859	0.852	0.852
	24	-	-	0.918	0.951	0.933	0.909	0.901	0.874	0.868	0.864
	28	-	-	-	0.927	0.917	0.928	0.879	0.847	0.819	0.775
	32	-	-	-	0.936	0.928	0.920	0.900	0.843	0.797	0.879
		Radius									
		11	12	13	14	15	16	17	18	19	20
Number of neighborhood pixels	4	0.717	0.719	0.713	0.706	0.710	0.787	0.704	0.788	0.769	0.797
	8	0.757	0.737	0.769	0.822	0.857	0.850	0.854	0.861	0.877	0.876
	12	0.785	0.780	0.835	0.870	0.862	0.895	0.869	0.878	0.906	0.888
	16	0.839	0.856	0.852	0.853	0.851	0.870	0.869	0.863	0.868	0.858
	20	0.863	0.886	0.866	0.892	0.881	0.907	0.917	0.865	0.910	0.898
	24	0.864	0.871	0.887	0.886	0.900	0.879	0.909	0.875	0.901	0.883
	28	0.860	0.886	0.888	0.884	0.880	0.817	0.890	0.896	0.869	0.845
	32	0.845	0.803	0.849	0.847	0.876	0.872	0.920	0.881	0.913	0.909

Table C.2. F₁ score obtained from clear film classification with polarized filtering imaging with variation of the radius together with the number of neighborhood pixels.

Infrared imaging – multiple LBP (LBP 1: radius = 9, number pixels = 28)

		Radius									
		1	2	3	4	5	6	7	8	9	10
Number of neighborhood pixels	4	0.953	0.971	0.968	0.986	0.985	0.978	0.975	0.986	0.989	0.989
	8	0.986	0.986	0.971	0.985	0.964	0.971	0.946	0.979	0.957	0.952
	12	-	0.989	0.946	0.961	0.982	0.993	0.960	0.993	0.978	0.982
	16	-	0.996	0.996	0.993	0.993	0.993	0.989	0.978	0.978	0.967
	20	-	-	0.982	0.989	0.978	0.975	0.993	0.978	0.993	0.996
	24	-	-	0.989	0.960	0.989	0.978	0.989	0.982	0.993	0.975
	28	-	-	-	0.979	0.989	0.993	0.978	0.968	0.948	0.993
	32	-	-	-	0.964	0.989	0.971	0.989	0.993	0.961	0.993
		Radius									
		11	12	13	14	15	16	17	18	19	20
Number of neighborhood pixels	4	0.989	0.989	0.996	0.993	0.979	0.968	0.979	0.974	0.964	0.971
	8	0.986	0.996	0.949	0.989	0.993	0.996	0.982	0.993	0.993	0.978
	12	0.989	0.989	0.993	0.989	0.982	0.993	0.993	0.993	0.996	0.989
	16	0.989	0.982	0.975	0.975	0.979	0.982	0.964	0.989	0.989	0.971
	20	0.978	0.978	0.971	0.968	0.968	0.993	0.993	0.993	0.960	0.978
	24	0.975	0.964	0.993	0.971	0.960	0.971	0.996	0.996	0.989	0.989
	28	0.953	0.978	0.982	0.968	0.978	0.989	0.982	0.989	0.974	0.989
	32	0.971	0.978	0.993	0.989	0.982	0.982	0.975	0.957	0.989	0.982

Table C.3. F_1 score obtained from clear film classification with infrared imaging with multiple LBP, where the LBP 2 parameters result from the variation of the radius together with the number of neighborhood pixels.

Polarized filtering imaging – multiple LBP (LBP 1: radius = 4, number pixels = 24)

		Radius									
		1	2	3	4	5	6	7	8	9	10
Number of neighborhood pixels	4	0.940	0.923	0.930	0.924	0.935	0.935	0.935	0.943	0.927	0.933
	8	0.952	0.932	0.947	0.947	0.940	0.924	0.948	0.924	0.935	0.000
	12	-	0.945	0.899	0.956	0.963	0.947	0.925	0.927	0.932	0.940
	16	-	0.923	0.924	0.939	0.923	0.962	0.940	0.963	0.904	0.943
	20	-	-	0.931	0.966	0.937	0.936	0.955	0.944	0.931	0.914
	24	-	-	0.959	0.944	0.967	0.963	0.940	0.967	0.932	0.937
	28	-	-	-	0.962	0.939	0.956	0.943	0.861	0.933	0.881
	32	-	-	-	0.951	0.955	0.925	0.909	0.911	0.927	0.940
		Radius									
		11	12	13	14	15	16	17	18	19	20
Number of neighborhood pixels	4	0.943	0.927	0.925	0.918	0.963	0.932	0.940	0.947	0.920	0.944
	8	0.934	0.940	0.947	0.944	0.943	0.954	0.944	0.928	0.924	0.927
	12	0.904	0.915	0.925	0.931	0.959	0.909	0.935	0.951	0.923	0.940
	16	0.941	0.921	0.948	0.939	0.939	0.944	0.951	0.944	0.927	0.939
	20	0.936	0.937	0.931	0.940	0.000	0.926	0.959	0.917	0.955	0.935
	24	0.925	0.959	0.917	0.927	0.936	0.923	0.951	0.950	0.955	0.943
	28	0.924	0.944	0.939	0.967	0.920	0.942	0.946	0.931	0.939	0.928
	32	0.916	0.959	0.865	0.916	0.940	0.936	0.946	0.947	0.951	0.922

Table C.4. F₁ score obtained from clear film classification with polarized filtering imaging with multiple LBP, where the LBP 2 parameters result from the variation of the radius together with the number of neighborhood pixels.

C.1.2 Rugged film

Infrared imaging

		Radius									
		1	2	3	4	5	6	7	8	9	10
Number of neighborhood pixels	4	0.787	0.893	0.828	0.877	0.889	0.838	0.816	0.864	0.885	0.897
	8	0.740	0.813	0.936	0.973	0.960	0.960	0.954	0.958	0.941	0.906
	12	-	0.807	0.958	0.969	0.965	0.958	0.958	0.925	0.967	0.949
	16	-	0.850	0.954	0.983	0.967	0.960	0.958	0.936	0.969	0.966
	20	-	-	0.946	0.960	0.958	0.973	0.946	0.945	0.954	0.969
	24	-	-	0.961	0.967	0.961	0.958	0.944	0.943	0.968	0.969
	28	-	-	-	0.961	0.959	0.952	0.954	0.936	0.956	0.955
	32	-	-	-	0.959	0.964	0.954	0.948	0.934	0.945	0.941
		Radius									
		11	12	13	14	15	16	17	18	19	20
Number of neighborhood pixels	4	0.895	0.910	0.900	0.921	0.918	0.915	0.906	0.893	0.864	0.888
	8	0.914	0.926	0.947	0.921	0.930	0.962	0.951	0.939	0.948	0.935
	12	0.962	0.950	0.968	0.962	0.965	0.948	0.962	0.941	0.971	0.941
	16	0.979	0.973	0.968	0.958	0.967	0.964	0.958	0.954	0.952	0.930
	20	0.975	0.979	0.973	0.969	0.960	0.956	0.950	0.942	0.912	0.896
	24	0.977	0.990	0.951	0.973	0.954	0.958	0.955	0.937	0.966	0.941
	28	0.977	0.985	0.974	0.967	0.969	0.969	0.965	0.960	0.945	0.939
	32	0.968	0.973	0.981	0.966	0.969	0.977	0.968	0.966	0.951	0.940

Table C.5. F_1 score obtained from rugged film classification with infrared imaging with variation of the radius together with the number of neighborhood pixels.

Polarized filtering imaging

		Radius									
		1	2	3	4	5	6	7	8	9	10
Number of neighborhood pixels	4	0.723	0.653	0.783	0.826	0.802	0.924	0.825	0.855	0.783	0.757
	8	0.700	0.787	0.794	0.915	0.881	0.914	0.940	0.881	0.782	0.826
	12	-	0.773	0.884	0.875	0.912	0.933	0.951	0.897	0.807	0.759
	16	-	0.798	0.898	0.918	0.920	0.984	0.959	0.937	0.763	0.819
	20	-	-	0.832	0.943	0.930	0.934	0.976	0.951	0.849	0.771
	24	-	-	0.891	0.926	0.900	0.939	0.906	0.840	0.770	0.723
	28	-	-	-	0.936	0.921	0.943	0.964	0.926	0.742	0.742
	32	-	-	-	0.938	0.945	0.947	0.947	0.932	0.749	0.719

		Radius									
		11	12	13	14	15	16	17	18	19	20
Number of neighborhood pixels	4	0.792	0.878	0.788	0.760	0.724	0.730	0.653	0.677	0.754	0.744
	8	0.849	0.816	0.777	0.882	0.895	0.888	0.641	0.827	0.798	0.798
	12	0.767	0.882	0.803	0.753	0.696	0.778	0.701	0.752	0.748	0.762
	16	0.839	0.819	0.554	0.672	0.774	0.789	0.778	0.683	0.677	0.700
	20	0.901	0.855	0.846	0.724	0.459	0.794	0.729	0.691	0.677	0.554
	24	0.831	0.845	0.865	0.767	0.648	0.705	0.708	0.673	0.701	0.662
	28	0.785	0.851	0.843	0.746	0.641	0.554	0.598	0.735	0.681	0.674
	32	0.789	0.744	0.713	0.683	0.704	0.613	0.660	0.642	0.647	0.680

Table C.6. F_1 score obtained from rugged film classification with polarized filtering imaging with variation of the radius together with the number of neighborhood pixels.

Infrared imaging – multiple LBP (LBP 1: radius = 12, number pixels = 24)

		Radius									
		1	2	3	4	5	6	7	8	9	10
Number of neighborhood pixels	4	0.960	0.949	0.938	0.941	0.954	0.946	0.967	0.931	0.960	0.965
	8	0.958	0.939	0.961	0.936	0.956	0.991	0.965	0.960	0.946	0.963
	12	-	0.960	0.967	0.965	0.973	0.962	0.964	0.960	0.966	0.971
	16	-	0.934	0.958	0.969	0.962	0.964	0.970	0.967	0.958	0.956
	20	-	-	0.957	0.950	0.954	0.966	0.953	0.959	0.964	0.955
	24	-	-	0.972	0.965	0.959	0.968	0.987	0.952	0.962	0.943
	28	-	-	-	0.960	0.956	0.965	0.975	0.943	0.941	0.958
	32	-	-	-	0.973	0.967	0.963	0.945	0.938	0.954	0.957
		Radius									
		11	12	13	14	15	16	17	18	19	20
Number of neighborhood pixels	4	0.939	0.985	0.973	0.962	0.977	0.958	0.983	0.960	0.948	0.968
	8	0.958	0.987	0.969	0.977	0.981	0.963	0.965	0.979	0.989	0.983
	12	0.975	0.989	0.981	0.985	0.990	0.968	0.985	0.956	0.990	0.981
	16	0.989	0.992	0.983	0.992	0.960	0.983	0.971	0.975	0.983	0.971
	20	0.981	0.981	0.977	0.987	0.992	0.992	0.992	0.979	0.953	0.983
	24	0.983	0.987	0.979	0.987	0.994	0.975	0.990	0.981	0.979	0.956
	28	0.981	0.990	0.971	0.983	0.987	0.985	0.989	0.983	0.994	0.968
	32	0.987	0.981	0.983	0.994	0.985	0.985	0.994	0.979	0.991	0.941

Table C.7. F₁ score obtained from rugged film classification with infrared imaging with multiple LBP, where the LBP 2 parameters result from the variation of the radius together with the number of neighborhood pixels.

Polarized filtering imaging – multiple LBP (LBP 1: radius = 6, number pixels = 16)

		Radius									
		1	2	3	4	5	6	7	8	9	10
Number of neighborhood pixels	4	0.968	0.972	0.943	0.972	0.964	0.964	0.992	0.996	0.968	0.992
	8	0.988	0.988	0.964	0.972	0.960	0.952	0.984	0.976	0.996	0.980
	12	-	0.984	0.984	0.984	0.955	0.968	0.964	0.955	0.943	0.937
	16	-	0.964	0.964	0.972	0.984	0.971	0.976	0.943	0.947	0.967
	20	-	-	0.996	0.988	0.980	0.956	0.968	0.948	0.972	0.959
	24	-	-	0.992	0.992	0.980	0.971	0.000	0.902	0.960	0.976
	28	-	-	-	0.988	0.968	0.984	0.976	0.988	0.951	0.946
	32	-	-	-	0.000	0.976	0.000	0.000	0.988	0.968	0.959

		Radius									
		11	12	13	14	15	16	17	18	19	20
Number of neighborhood pixels	4	0.996	0.950	0.964	0.984	0.992	0.996	0.980	0.992	0.992	0.980
	8	0.935	0.980	0.980	0.976	0.992	0.968	0.936	0.959	0.992	0.984
	12	0.960	0.972	0.948	0.992	0.947	0.996	0.976	0.968	0.980	0.967
	16	0.000	0.980	0.992	0.968	0.980	0.996	0.948	0.984	0.939	0.967
	20	0.988	0.984	0.996	0.988	0.996	0.956	0.996	0.947	0.000	0.960
	24	0.996	0.000	0.992	0.984	0.976	0.000	0.984	0.956	0.984	0.968
	28	0.996	0.996	0.960	0.976	0.793	0.928	0.956	0.959	0.925	0.972
	32	0.992	0.000	0.964	0.926	0.963	0.940	0.000	0.952	0.976	0.984

Table C.8. F_1 score obtained from rugged film classification with polarized filtering imaging with multiple LBP, where the LBP 2 parameters result from the variation of the radius together with the number of neighborhood pixels.

C.2 Gray level co-occurrence matrix results

Initial Parameters:

Number of gray levels NL = 8

Distance DI = 1

Direction angle DA= 0°

Descriptors: CON, COR, ENE, ENT, HOM

Number of neurons in hidden layer = 10

C.2.1 Clear film

Number gray levels NL	8	16	32	64	28	56
Infrared imaging	0.7698	0.8231	0.8562	0.8532	0.8304	0.8464
Polarized filtering imaging	0.7986	0.8125	0.8321	0.8201	0.7601	0.7986

Table C.9. F₁ score obtained from clear film classification with variation of the number of gray levels.

Direction angle DA (°)	0°	45°	90°	135°
Infrared imaging	0.8562	0.8746	0.8456	0.8394
Polarized filtering imaging	0.8321	0.8571	0.8308	0.853

Table C.10. F₁ score obtained from clear film classification with variation of the angle direction (NL=32).

Distance DI	1	2	3	4	5	6	7	8	9	10
Infrared imaging	0.875	0.874	0.886	0.887	0.903	0.874	0.895	0.894	0.879	0.893
Polarized filtering imaging	0.857	0.848	0.841	0.836	0.817	0.824	0.803	0.813	0.810	0.818

Distance	11	12	13	14	15	16	17	18	19	20
Infrared imaging	0.897	0.887	0.897	0.902	0.913	0.898	0.906	0.898	0.901	0.903
Polarized filtering imaging	0.825	0.864	0.838	0.845	0.823	0.834	0.817	0.830	0.819	0.857

Table C.11. F₁ score obtained from clear film classification with variation of the pixels distance (NL=32; DA=45°).

Descriptors	ALL	Without ENT	Without HOM	Without ENE	Without COR	Without CON
Infrared imaging	0.913	0.8905	0.8842	0.8905	0.9007	0.8602
Polarized filtering imaging	0.8635	0.7579	0.8248	0.8286	0.8151	0.8394

Table C.12. F₁ score obtained from clear film classification with variation of the descriptors used (NL=32; DA=45°; DI=15 and DI=12 for infrared and polarized filtering imaging respectively).

Multiple direction angles DA (°)	45°	45°; 0°	45°; 90°	45°; 135°
Infrared imaging	0.913	0.9181	0.911	0.9111
Polarized filtering imaging	0.8635	0.8864	0.8519	0.8397

Table C.13. F₁ score obtained from clear film classification with multiple angle directions (NL=32; DI=15 and DI=12 for infrared and polarized filtering imaging respectively).

Distance DI_2	1	2	3	4	5	6	7	8	9	10
Infrared imaging	0.935	0.921	0.917	0.930	0.920	0.943	0.909	0.924	0.925	0.923
Polarized filtering imaging	0.882	0.886	0.892	0.891	0.882	0.908	0.891	0.891	0.902	0.886
Distance DI_2	11	12	13	14	15	16	17	18	19	20
Infrared imaging	0.913	0.919	0.931	0.914	0.931	0.925	0.918	0.920	0.928	0.928
Polarized filtering imaging	0.905	0.886	0.891	0.896	0.873	0.900	0.916	0.892	0.899	0.878

Table C.14. F_1 score obtained from clear film classification with variation of the pixels distance of the second angle direction (NL=32, $DI_1=15$, $DA_1=45^\circ$, $DA_2=0^\circ$ for infrared imaging; NL=32, $DI_1=12$, $DA_1=45^\circ$, $DA_2=0^\circ$ for polarized filtering imaging)

Number of Neurons	10	20	30	40	50	60	70	80	90	100
Infrared imaging	0.943	0.921	0.915	0.918	0.919	0.926	0.912	0.930	0.921	0.920
Polarized filtering imaging	0.916	0.888	0.871	0.871	0.889	0.874	0.881	0.882	0.877	0.870

Table C.15. F_1 score obtained from clear film classification with variation of the pixels distance of the second angle direction (NL=32, $DI_1=15$, $DA_1=45^\circ$, $DI_2=6$, $DA_2=0^\circ$ for infrared imaging; NL=32, $DI_1=12$, $DA_1=45^\circ$, $DI_2=17$; $DA_2=0^\circ$ for polarized filtering imaging)

C.2.2 Rugged film

Number gray levels NL	8	16	32	64	28	56
Infrared imaging	0.7842	0.8298	0.8621	0.8538	0.828	0.8593
Polarized filtering imaging	0.6887	0.7273	0.7547	0.7265	0.7243	0.7083

Table C.16. F_1 score obtained from rugged film classification with variation of the number of gray levels.

Direction angle DA (°)	0°	45°	90°	135°
Infrared imaging	0.8621	0.8459	0.8397	0.8469
Polarized filtering imaging	0.7547	0.6897	0.6644	0.6853

Table C.17. F_1 score obtained from rugged film classification with variation of the angle direction (NL=32).

Distance	1	2	3	4	5	6	7	8	9	10
Infrared imaging	0.862	0.839	0.833	0.850	0.874	0.896	0.895	0.889	0.899	0.889
Polarized filtering imaging	0.755	0.786	0.739	0.879	0.862	0.939	0.926	0.947	0.939	0.939
Distance	11	12	13	14	15	16	17	18	19	20
Infrared imaging	0.885	0.889	0.886	0.906	0.889	0.883	0.893	0.872	0.857	0.833
Polarized filtering imaging	0.891	0.890	0.772	0.815	0.737	0.736	0.724	0.763	0.740	0.759

Table C.18. F_1 score obtained from rugged film classification with variation of the pixels distance (NL=32; DA=0°).

Descriptors	ALL	Without ENT	Without HOM	Without ENE	Without COR	Without CON
Infrared imaging	0.9063	0.8915	0.8352	0.8255	0.8927	0.9023
Polarized filtering imaging	0.9469	0.9388	0.7744	0.9428	0.9317	0.9393

Table C.19. F_1 score obtained from rugged film classification with variation of the descriptors used (NL=32; DA=0°; DI=14 and DI=8 for infrared and polarized filtering imaging respectively).

Multiple direction angles DA (°)	0°	0°; 45°	0°; 90°	0°; 135°
Infrared imaging	0.9063	0.9482	0.9692	0.8969
Polarized filtering imaging	0.9469	0.9677	0.9516	0.9474

Table C.20. F_1 score obtained from rugged film classification with multiple angle directions (NL=32; DI=15 and DI=12 for infrared and polarized filtering imaging respectively).

Distance DI_2	1	2	3	4	5	6	7	8	9	10
Infrared imaging	0.975	0.970	0.975	0.979	0.973	0.977	0.971	0.977	0.973	0.977
Polarized filtering imaging	0.963	0.968	0.952	0.984	0.959	0.963	0.960	0.971	0.964	0.964
Distance DI_2	11	12	13	14	15	16	17	18	19	20
Infrared imaging	0.971	0.989	0.977	0.969	0.981	0.975	0.990	0.987	0.968	0.981
Polarized filtering imaging	0.968	0.964	0.955	0.964	0.963	0.963	0.959	0.959	0.980	0.971

Table C.21. F_1 score obtained from rugged film classification with variation of the pixels distance of the second angle direction (NL=32, $DI_1=14$, $DA_1=0^\circ$, $DA_2=90^\circ$ for infrared imaging; NL=32, $DI_1=8$, $DA_1=0^\circ$, $DA_2=45^\circ$ for polarized filtering imaging)

Number of Neurons	10	20	30	40	50	60	70	80	90	100
Infrared imaging	0.990	0.964	0.958	0.970	0.953	0.956	0.954	0.954	0.962	0.962
Polarized filtering imaging	0.984	0.954	0.931	0.936	0.935	0.926	0.915	0.939	0.926	0.940

Table C.22. F_1 score obtained from rugged film classification with variation of the pixels distance of the second angle direction (NL=32, $DI_1=14$, $DA_1=0^\circ$, $DI_2=17$, $DA_2=90^\circ$ for infrared imaging; NL=32, $DI_1=8$, $DA_1=0^\circ$, $DI_2=4$; $DA_2=45^\circ$ for polarized filtering imaging)